UNIVERSIDAD TÉCNICA FEDERICO SANTA MARÍA
DEPARTAMENTO DE INGENIERÍA MECÁNICA
VALPARAÍSO - CHILE

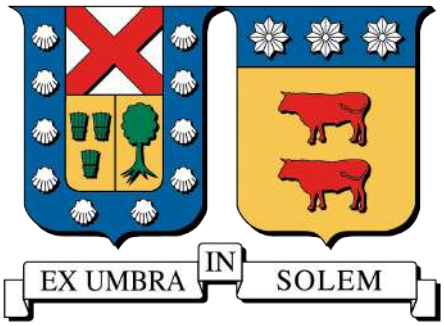

DEVELOPMENT OF A DIGITAL TWIN FOR SMART MANAGEMENT OF THERMAL LOADS IN RESIDENTIAL MICROGRIDS WITH PEER-TO-PEER TRANSACTIONS

JAVIER IGNACIO SALLES MARDONES

THESIS WORK TO OBTAIN THE DEGREE OF
MAGÍSTER EN CIENCIAS DE LA INGENIERÍA MECÁNICA

THESIS ADVISOR	:	Ph.D. RODRIGO BARRAZA V.
INTERNAL EXAMINER	:	Ph.D. MOHAMED ABDELHAMID A.
EXTERNAL EXAMINER	:	Ph.D. LUIS GUTIERREZ L.

JUNE 2024

Thesis:

DEVELOPMENT OF A DIGITAL TWIN FOR SMART MANAGEMENT OF THERMAL LOADS IN RESIDENTIAL MICROGRIDS WITH PEER-TO-PEER TRANSACTIONS

Author:

JAVIER IGNACIO SALLES MARDONES

This thesis is presented in partial fulfillment of the requirements for the degree of MAGÍSTER EN CIENCIAS DE LA INGENIERÍA MECÁNICA at Universidad Técnica Federico Santa María, Valparaíso, Chile.

Thesis advisor,
Ph.D. RODRIGO BARRAZA V. ———————————————-

Internal examiner,
Ph.D. MOHAMED ABDELHAMID A. ———————————————-

External examiner,
Ph.D. LUIS GUTIERREZ L. ———————————————-

JUNE 2024

Agradecimientos

Pensaba que nunca iba a llegar este momento. Siento que fue un largo y difícil camino, con altos y bajos, pero se salió adelante con voluntad, disciplina y esfuerzo.

Es por esto que agradezco a todas las personas que me ayudaron y fueron parte de este proceso, en especial a mis padres por confiar en mí y darme siempre todo lo que tuvieron a su alcance.

También agradezco a mis profesores guías, partiendo por el Sr. Mohamed, por su gran dedicación por su trabajo y profesionalismo, trabajando junto a él arduamente para poder enviar los papers. También, al Sr. Rodrigo, no sólo por guiarme con su increíble expertiz y conocimientos, sino también por su apoyo como persona, mostrándome empatía en momentos difíciles. También, al Sr. Alex, que me guió durante la primera etapa de la carrera y siempre tuvo disposición para colaborar en la investigación. Ha sido un gusto haberlos conocido y haber trabajado con ustedes.

Finalmente, agradezco a la Universidad Técnica Federico Santa María por haberme otorgado las facilidades y la oportunidad de potenciar mi carrera profesional dentro del ámbito de la investigación. Espero haberles retribuido.

Abstract

Public policies in Chile aim to improve energy efficiency and promote distributed energy resources (DERs) in residential communities. However, challenges persist with respect to solar power curtailment due to supply-demand mismatch and the need to inform the community about the energy performance of their buildings to incentivize residential energy efficiency projects. This work develops a digital twin (DT) in its design phase to evaluate the potential benefits of smart thermal load management in residential microgrids implementing peer-to-peer (P2P) markets. The developed DT considers smart management of air conditioning (AC) systems using overcooling and overheating techniques, and domestic hot water (DHW) tanks to promote self-consumption in the microgrid.

Different scenarios are modeled, analyzed, and compared, applying the formulated smart thermal load management techniques in prosumers homes, both with and without a battery energy storage system (BESS), and consumers. The results show a synergistic effect between the implementation of P2P markets and the smart management of DHW tanks and AC systems operation, allowing for a reduction of up to 56.4% and 2.6% in the annual electricity bills of prosumers and consumers, respectively. Furthermore, at the residential microgrid level, community energy costs would be reduced by up to 11.5%, self-consumption ratio (SCR) and self-sufficiency ratio (SSR) would increase by up to 33.5% and 17.8%, respectively, and there would be a reduction in energy import from the utility grid (UG) during periods of high demand by up to 17.1%. This would result in better local utilization of surplus photovoltaic (PV), increased energy independence from the UG, load shifting from periods of high consumption to periods of high solar irradiation, and an improvement in the profitability of prosumers' distributed generation projects.

The results of the sensitivity analysis based on the sizing of the BESS, AC systems, and DHW tanks indicate that small sizing of the latter two has a positive impact on the bills of the RCs, while increasing the BESS capacity offers greater benefits than increasing the capacity of DHW tanks, under a fixed pricing scheme. Additionally, a geographical analysis was carried out to extend the evaluation to different geographical zones of the country. The general trend indicates that the most influential variable in the benefits is the level of solar radiation, followed by the stringency of thermal insulation regulations, which allows for better performance in terms of energy efficiency of the AC system. The developed DT contributes to local public policies providing an evaluation tool for informed decision-making by the community.

Keywords. Peer-to-Peer Markets, Photovoltaic systems, Battery Energy Storage Systems, Domestic Hot Water, Air Conditioning Systems

Contents

List of Tables

List of Figures

1 | Glosary

Table 1.1: List of Acronyms.

Abb.	Significance	Abb.	Significance
DER	Distributed Energy Resources	DT	Digital Twin
P2P	Peer-to-Peer	AC	Air Conditioning
DHW	Domestic Hot Water	BESS	Battery Energy Storage System
SCR	Self-consumption ratio	SSR	Self-sufficiency ratio
UG	Utility Grid	PV	Photovoltaic
DG	Distributed Generation	RC	Residential Customer
ROI	Return of Investment	AG	Aggregator
DR	Demand Response	P2H	Power-to-Heat
TES	Thermal Energy Storage	EWH	Electric Water Heater
HVAC	Heating, Ventilation, and Air Conditioning	TCL	Thermostatically Controlled Loads
HP	Heat Pump	TOU	Time-Of-Use
LEM	Local Energy Market	HEMS	Home Energy Management System
FiT	Feed-in-tariff	SoC	State of Charge
IoT	Internet of Things	MVES	Multi-vector energy system
LOIN	Level of Information Needs	BIM	Building Information Modelling
KPI	Key Performance Indicator	MMR	Mid-market rate
FR	Frequency Response	COP	Coefficient Of Performance
EER	Energy Efficiency Ratio	SHR	Sensible Heating Ratio
PMV	Predicted Mean Vote	TMY	Typical Meteorological Year
IRR	Internal Rate of Return	EWMA	Exponential Weighted Moving Average

Table 1.2: Parameters definition.

Indices and sets			
$t \in T$	Time periods set	$i,j \in U$	Users set
Simulation parameters			
Δt	Duration of one time period	P_{ava}	Available power
Meteorological variables			
T_a	Dry bulb ambient temperature	RH_a	Ambient relative humidity
T_{wb}	Wet bulb ambient temperature	S_i	Solar irradiation
W_v	Wind velocity	k_a	Air thermal conductivity

ν_a	Air kinematic viscosity	μ_a	Air dynamic viscosity
c_a	Air specific heat	ρ_a	Air density

PV model parameters

N	N° installed PV panels	L_f	System power loss factor
Y	PV panels guaranteed yield	TP_{PV}	Power without factoring losses
PL_t	Thermal power losses	G_t	Incident global irradiance
U	Thermal losses factor	n_{PV}	PV panel efficiency
RP_{PV}	PV panel rated power	EA_{PV}	Effective PV area of the panel
α	Absorption coefficient	PTC	Temp. variation loss coefficient
$NOCT$	Rated PV cell temperature	Y_L	Yield loss due to panel degradation
P_{PV}	Effective PV power	CT	Cell temperature

BESS model parameters

B_c	Battery bank capacity	S_l	Stand-by losses
Ma_s	Maximum SoC	Mi_s	Minimum SoC
C_e	Charging efficiency	D_e	Discharging efficiency

P2P market parameters

C_T^R	RC total cost	C_{EC}^{AR}	RC energy consumption cost
C_{EI}^{RA}	RC energy injection cost	P_{PC}^{AR}	Power consumed from P2P market
r_C	Fraction of energy imported from P2P market	W_{EC}^{PR}	Price of energy imported from the P2P market
W_{EC}^{UR}	Price of energy imported from the UG	P_{PI}^{RA}	Power injected into P2P market
W_{EI}^{PR}	Price of energy sold in the P2P market	W_{EI}^{RU}	Price of energy injected in the P2P market
S_c	Self-consumption	TC_{EC}^{AC}	Total cost of energy consumed from P2P market
TC_{EI}^{AC}	Total income from energy injections into P2P market	W_{FRR}^{UA}	Incentive cost by receiving
W_{FRR}^{AU}	Incentive cost by injecting	W_{SP}^{PR}	P2P market special price
C_{FR}^{UA}	Reward for receiving during FR	C_{FR}^{AU}	Reward for injecting during FR
TI_{AG}	Total income for the AG	TI_{UG}	Total income for the UG

DHW model parameters

ρ_w	Water density	c_w	Water specific heat
T_{w0}	Water initial temperature	$\dot{m}_{dhw}$	Tank inlet/outlet mass flux
L_{wsup}	Litres of DHW supplied	T_{wsup}	DHW supply temperature
V_{dhw}	Tank internal volume	A_{dhw}	Tank average surface
P_{dhw}	Tank electric coil rated power	MP_{dhw}	Tank electric coil maximum power
D_{dhw}	Tank external diameter	H_{dhw}	Tank external height
x_f	Insulating foam layer thickness	I_f	Insulating foam heat loss factor
x_s	Stainless steel layer thickness	k_{ss}	Stainless steel thermal conductivity

T_{wmin}	Minimum operating temperature	T_{wmax}	Maximum operating temperature
IT_{dhw}	Tank inlet temperature	h_{Wi}	Internal heat convection coefficient
Pr	Prandtl number	h_{We}	External heat convection coefficient
Re_D	Reynolds number	$\overline{Nu}_D$	Average Nusselt number
U_{dhw}	Tank thermal transmittance	T_{dhw}	Internal water average temperature

AC model parameters

$n_a, n_{ws}, n_W, n_R, n_H$		Nodes for windows, wall, roof and internal air	
T_n	Temperature of node n	A_n	Surface area for node n
C_n	Heat capacity for node n	ϵ_n	Materials emissivity for node n
e_{ni}	Thickness of material i of node n	V_{ni}	Volume of material i of node n
k_{ni}	Thermal conductivity of material i of node n	ρ_{ni}	Density of material i of node n
c_{ni}	Specific heat of material i of node n	U_n	U-value of node n
h_s	Surface convective-radiative coefficient	Q_L	Heat input from occupants and applinces
Q_R	Heat input from solar radiation through windows	Q_u	Heat input from the AC system
Q_{inf}	Heat input due to outside air infiltration	σ	Stefan-Boltzmann constant
T_{mn}	Mean thermodynamic temperature	I_{tm}	Thermal mass index
H_s	Heat capacity per unit area	E_c	Base electrical consumption
met	Metabolism unit	B_s	Body surface area
M	Metabolic rate	Q_{occ}	Heat gain per occupant
ACH	Air changes per hour	α_R	Fraction of filtered solar radiation

Thermal comfort model parameters

W	Mechanical work done	p_{ia}	Indoor water vapor pressure
f_{cl}	Ratio of clothed body surface	T_{cl}	Clothing surface temperature
T_{MR}	Mean radiant temperature	h_c	Convective heat transfer coefficient
P_{ews}	External saturated water vapor pressure	H_{se}	External specific humidity
R_{da}	Dry air specific gas constant	R_w	Water vapor specific gas constant
P_T	Atmospheric absolute pressure	RH_a	Ambient relative humidity
H_{si}	Indoor specific humidity	v_{ar}	Relative air velocity

2 | Introduction

2.1 Motivation

Currently, Chile is undergoing an energy transition process aimed at promoting projects for generation from non-conventional renewable sources, with the goal of decarbonizing the energy matrix and incentivizing energy efficiency improvements in both residential and industrial sectors. To achieve this, the Chilean government has proposed an Energy Agenda 2022-2026, highlighting eight main areas to promote in the short term [1]. Among the new policies to be implemented, the following points are noteworthy and aligned with our work:

- The Social Solar House Program which promotes the installation of distributed generation (DG) systems, along with the creation of new reforms to legal regulations aimed at facilitating such programs. By 2040, the optimal installation of DG systems in Chile is projected to reach around 6.22 GW, constituting 40% of the newly installed generation capacity in the electrical system [2]. However, the current level of DG implementation is far from this value, which is attributed to the lack of information available to residential customers (RCs) regarding its benefits. Additionally, this approach not only reduces the investment required to improve the transmission system, which cost about 279 million USD in 2023 [3], but also avoids the installation of large-scale renewable generation plants.
- The National Energy Efficiency Plan aimed to reducing total energy consumption by 4.5% between 2022 and 2026. One of its policies is the promotion of energy efficiency by ensuring appliances meet standards, and incentivizing the use of solar thermal systems for DHW.
- Thermal Insulation Programs, aimed at improving housing conditioning and thermal comfort, reducing heating costs, and decreasing energy consumption by 30% compared to current standards.
- Strategic energy planning with local communities, public and private entities, through programs such as the Regional Energy Strategic Plan and the Community Energy Program. Additionally, providing technical assistance and co-financing to promote the installation of local DERs, energy efficiency, and support for local energy ventures.
- Development of new electrical infrastructure in terms of capacity and technology, as well as establishing more equitable electricity tariffs, where higher consumers will pay more to stabilize prices.

With respect to the last point, in the local energy sector during 2023, the total installed capacity in the national electrical system reached 32.8 GW, of which 40.8% corresponds to non-conventional renewable

energies, including solar energy, which accounts for 25.6% of the total and represented 19.7% of the total annual generation [4]. However, renewable energies exhibit a high curtailment rate, a longstanding issue in the Chilean electrical system. In 2023, the annual curtailment from wind and solar plants was 812 and 1803 GWh [5], respectively, corresponding to 8.2% and 11% of their total annual generation, respectively [4]. Causes include the advancement of generation projects outpacing transmission capacity, and supply-demand mismatch, especially during periods of high solar irradiation and critical consumption periods. Additionally, the inflexibility of base load thermal generation plants, which cannot be paused due to safety conditions and technical restrictions, results in variable generation plants, such as solar and wind, curtailing their generation to avoid transmission line problems when demand is significantly lower than generation [6]. In addition, fossil fuel-based generation plants have been affected by the increase in supply costs, where between 2019 and 2022, coal prices have increased by 242%, oil by 53%, and liquefied gas by 600% [7]. Furthermore, Chile has experienced a severe local drought over the past decade that has affected base generation, resulting in a 26% reduction in hydroelectric generation between 2019 and 2021, which typically accounts for approximately 20% of the total system's generation [8].

Solutions under consideration include large-scale energy storage projects, which would provide flexibility in transmission systems. Currently, there are 486 MW of installed power in large-scale BESS projects under construction [4]. Other solutions include accelerating the development of the transmission system, exporting energy to neighboring countries, and reviewing technical minimum generation requirements in base load thermal generation plants [6]. However, these proposed solutions are very costly, large-scale, and long-term. Therefore, there is a necessity to investigate complementary short-term, low-cost, and smaller-scale solutions that produce a positive impact on communities, the environment, and the economy, while promoting the aforementioned public policies, and increasing community self-consumption rates and grid independence. Therefore, the construction of a tool to assess these key indicators would be of great value, considering P2P systems, DERs such as PV and BESS, the level of energy efficiency in homes based on thermal insulation, smart management of AC systems and DHW storage tanks, and the thermal comfort of occupants.

2.2 Main Objective

This work aims to develop a digital twin of the energy requirements of households to model and analyze the potential benefits of smart thermal load management when integrated into a residential microgrid that implements a Peer-to-Peer energy transaction market.

2.3 Specific Objectives

- Conduct a comprehensive review of the state of the art in Peer-to-Peer energy markets, smart thermal load management and digital twins in residential microgrid systems.
- Design simulation models to accurately represent the energy requirements of households, including air conditioning systems and domestic hot water supply, and integrate them into the model of a residential microgrid system that incorporates Peer-to-Peer transactions, distributed photovoltaic generation, and battery energy storage systems.
- Develop smart thermal load management algorithms that are grounded in comfort ranges and energy

demand, while considering diverse meteorological profiles, household occupancy, and building thermal insulation rates specific to thermal zones.

- Assess the impact of smart thermal load management on energy efficiency at the household level and within the microgrid, including the quantification of economic savings, energy key performance indicators, and the identification of the most influential parameters through sensitivity analysis.
- Extend the study to different geographical zones in Chile to assess how the impact varies based on different thermal insulation regulations and meteorological conditions.

3 | Related Work

3.1 Study Cases of P2P Markets

The global trends in microgrids and local P2P markets could be locally implemented, allowing RCs to exchange PV surplus output among themselves [9]. This arrangement has the potential to offer more substantial compensation for surplus generation, thereby significantly enhancing the profitability of DERs projects. Moreover, P2P markets offer several benefits, such as enhancing distribution grid operational efficiencies, increasing resilience and flexibility of the electrical system to avoid failures, reducing dependence on high-voltage transmission, improving supply quality indices, minimizing losses caused by inversions of power flow direction in the distribution grid, and contributes to stabilizing the UG frequency [10].

Various studies have been conducted on the implementation of P2P markets outside of Chile. In [11], the advantages of P2P trading for RCs in a community microgrid of 100 to 300 households were explored. Figure 3.1 shows the distribution of households within the community microgrid, where there are prosumers with local PV systems and net consumers. The local private microgrid allows for local energy transfers between RCs, without the need to use the main UG. Figure 3.2 compares the schematic diagrams of a (a) conventional case and (b) a case with P2P energy trading. In case (a), households exchange energy with the public UG, while payments are managed by the retail market supplier, which defines energy prices based on the wholesale market. In case (b), there is a community energy system that manages power flows and payments with the public UG, while households have access to power trading among themselves. Market price paradigms such as bill sharing, mid-market rate, and auction-based pricing were introduced. The results showed that a moderate PV penetration in P2P energy trading, coupled with diverse demand profiles, led to a significant 30% reduction in electricity bills.

In [12], a P2P energy transaction model was proposed, which uses a virtual consumer management system within the UG, which operates in real time. Simulations were conducted in a microgrid featuring four RCs with small PV systems. The model aimed to maximize profits for participants and to enhance the return on investment (ROI). Figure 3.3 shows the schematic diagram of the proposed energy trading system, where prosumers have the option to inject their local surpluses into the UG to save on their electricity bills through net metering, or sell the surpluses to consumers at a price higher than the injection price into the UG. P2P transactions are managed by a power trading broker, which is responsible for both energy and data transfers, such as the amount of energy to be transferred and the corresponding payments.

In [13], a cost-effective energy trading system was suggested for an off-grid community with DERs. Each house consists of a PV system, BESS, and an IoT server for real-time energy data management. In

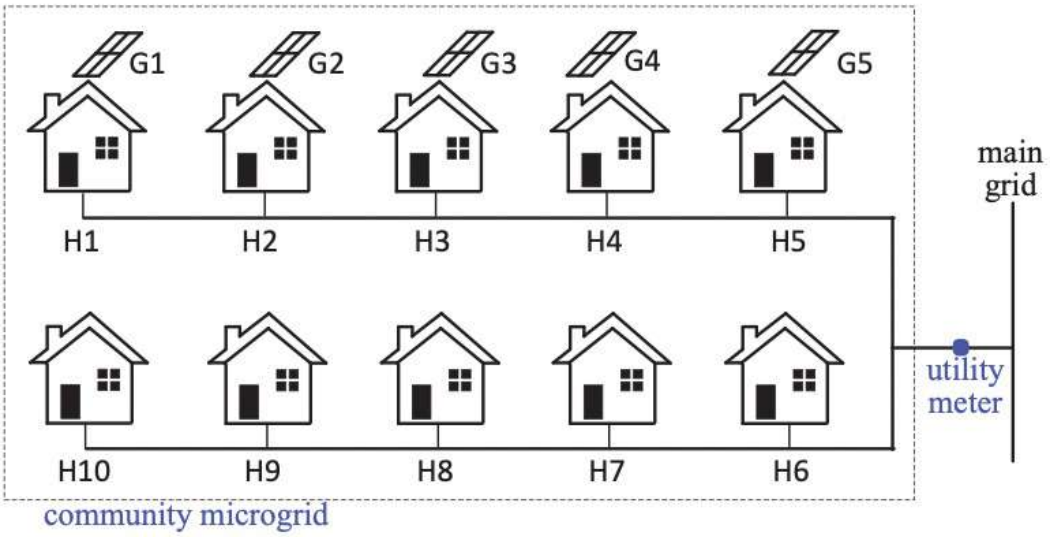

Figure 3.1: Schematic diagram of a community microgrid and its connection to the main grid [11].

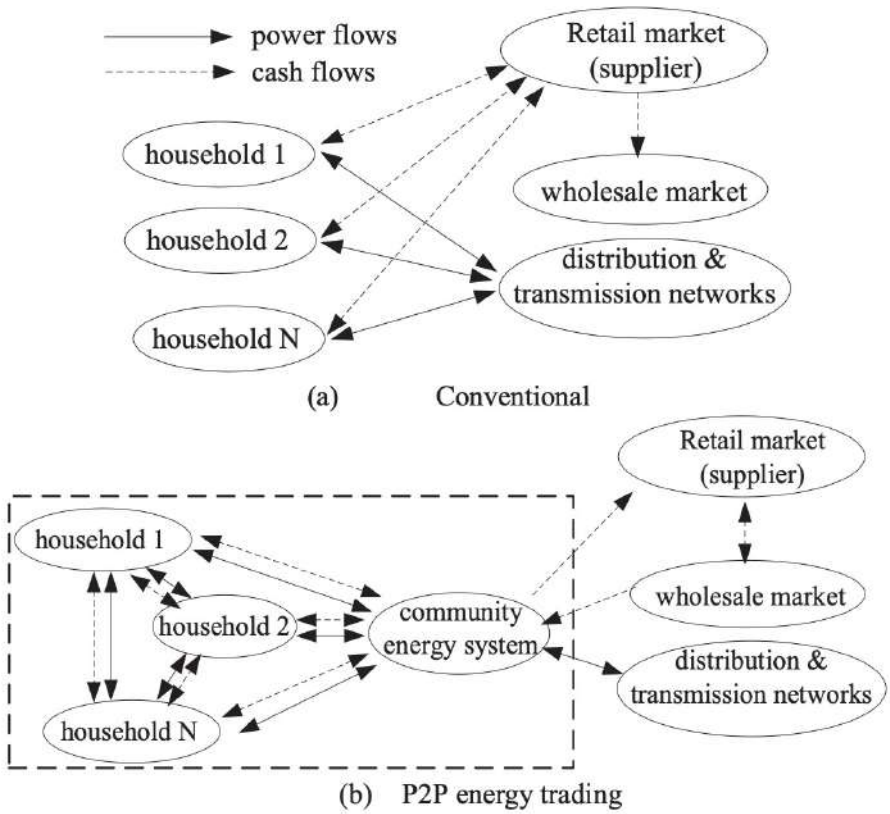

Figure 3.2: Schematic scheme of trading architecture of a community microgrid [11].

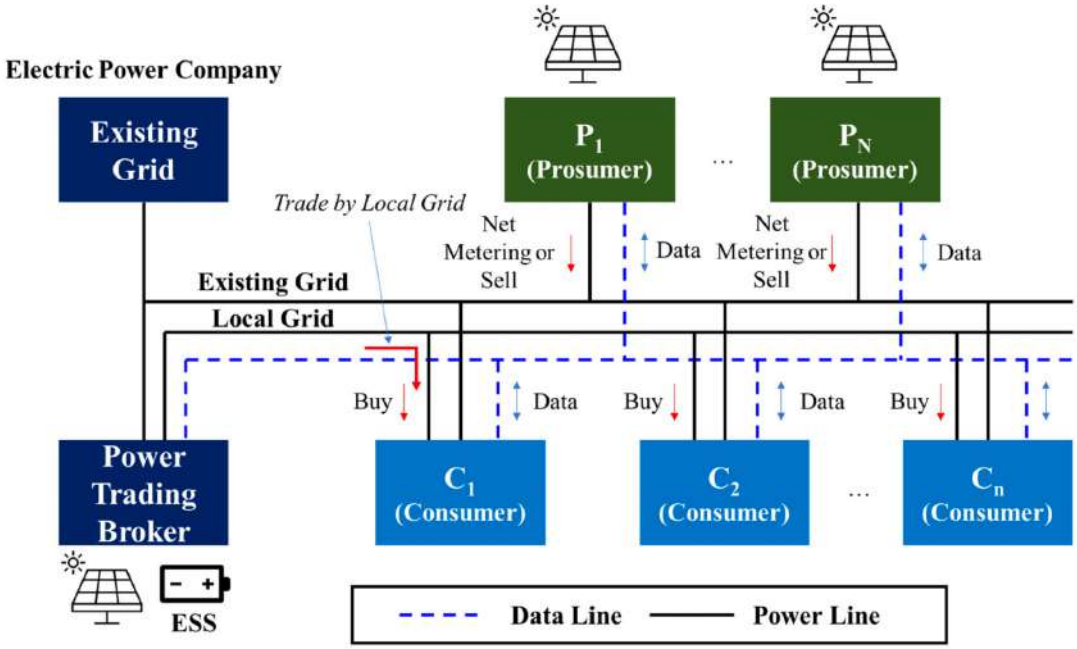

Figure 3.3: Schematic diagram of a typical energy trading system [12].

[14], a cooperative mechanism centered on the user was developed to encourage user involvement in P2P energy trading. An experiment was conducted within a residential community with 19 households, involving real-time measurements of demand, PV generation, and BESS status. The results showed an average P2P market price approximately 27% lower than the UG price. In [15], potential benefits of P2P markets were studied for 75 households integrating with DERs. Data on load, PV generation and BESS status were collected. Real-time pricing for the UG was assumed. The results indicated that consumers can reduce their electricity bills by up to 27.3%, decrease reliance on the UG, enhance self-sufficiency, and optimize BESS usage during more profitable time periods.

In [16], a P2P energy trading system was proposed, which virtually matches energy supply and demand, while in the physical layer, energy flows are traded using the existing UG. The results demonstrated that the P2P system could effectively and reliably transmit energy in a residential microgrid with 20 households and 1 office. In [17], P2P energy transactions among 3 households with PV systems were compared to conventional methods. Weather and load data were collected, and the actual electricity transactions were facilitated by the UG as an intermediary, which charged a fee. The results favored P2P trading as the most cost-effective approach, as it enables RCs to remain within lower consumption tariff ranges. In [18], a P2P energy trading model was introduced, considering PV generation and BESS. 30 different buildings were divided into groups with PV plus BESS, only PV, only BESS, and none of the above. Participants placed buy or sell orders in the P2P market, with a microgrid operator overseeing transactions, managing microgrid consumption, and setting market prices. The results showed that P2P market empowers households to invest in local PV systems.

In [19], the study assessed the impact of local regulatory frameworks on P2P markets. The initial designs were economically unattractive to RCs due to high public taxes on the use of the UG infrastructure. A novel market design was proposed incorporating a few legal adjustments. Simulations included 14 households,

a large PV plant, and a microgrid operator. Data on electricity prices, PV generation, and load were collected. The results indicated that the proposed model enables the community to benefit from the P2P market. In [20], various strategies to incentive microgrid development were examined within smart energy communities, considering architectural layers, DERs, UG integration, and local electricity markets. In [21], a hierarchical blockchain architecture is developed for an electric vehicle-to-grid trading system. It facilitates smart EV charging and discharging schedules to contribute to the UG load regulation and ensure fair benefit distribution among EV owners, aggregators (AGs), and the UG. Table 3.1 summarizes and compares previous research work on P2P energy trading studies.

The research on P2P energy trading is an emerging topic attracting a lot of attention with many research studies and trial projects across the world [22, 23, 24]. To implement such solutions, it is essential to define the responsibilities and roles of consumers in the P2P market, as well as to develop the P2P market policies and economic incentives for energy trading [22]. Also, there is a need for policies and regulations to incentive the participation of DERs in the local energy market [23]. Furthermore, there is a need to analyze how BESS would impact the outcomes of prosumers with PV systems [24]. In the context of Chile, current local regulations do not permit the implementation of P2P markets. This restriction is primarily attributed to the absence of studies advocating for the adoption of P2P energy trading and the lack of assessments regarding its potential benefits. An assessment of this nature has the potential not only to strengthen existing public energy policies, such as Casa Solar program, but also to stimulate the formulation of new policies geared towards enhancing the profitability of DG projects. This, in turn, could result in benefits not only for prosumers but also for consumers, potentially leading to reductions in their electricity bills.

Table 3.1: Summary of related work on P2P energy trading.

Ref.	Location	Main Contributions or Results	Participants	Specifications (A: Data collection, B: DERs)	Year
[12]	South Korea	Maximized profits and improved ROIs for prosumers and consumers	4 households	(A) Load: Real-time dataset; PV Generation: Theoretical estimation; Electricity prices: Local bills, (B) PV: 0.4-7.5 kWp installed power	2021
[11]	UK	Community electricity bills reduction by 30%	10-300 households	(A) Load: Real-time dataset; PV Generation: Real-time dataset, (B) PV: 2-3.5 kWp peak power generation	2017
[13]	Pakistan	P2P market implementation in an off-grid community	10 households		2022
[14]	Japan	P2P market price 27% lower than UG price is achieved	19 households	(A) Load: Real-time dataset; PV Generation: Real-time dataset; Electricity prices: According to power market price, (B) PV: 4.2-7.2 kWp installed power; BESS: 9.8 kWh capacity	2021
[15]	USA	Prosumers bill reduction up to 27.3% and increase in self-consumption is achieved	75 households	(A) Load: Real-time dataset; PV Generation: Real-time dataset; Electricity prices: Real-time power markets prices	2022
[16]	Japan	P2P system could secure and stably transmit energy	20 households and 1 office	(B) BESS: 9.8 kWh capacity	2021
[17]	South Korea	P2P system maintains lower electricity prices than grid prices and avoids energy injection into grid	3 households	(A) Load: Theoretical estimation; PV Generation: Theoretical estimation; Electricity prices: Progressive rate system; Weather data: Meteonorm software, (B) PV: 3 kWp installed power	2020
[18]	China	P2P system encourage users to invest in PV systems and increase self-consumption	30 households	(A) Load: Real-time database; PV Generation: Theoretical estimation, (B) PV: 595 kWp installed power	2020
[19]	Germany	P2P market model adapts to regulatory frameworks and allows communities to obtain benefits	14 households and 1 PV plant	(A) Load: Real-time database; PV Generation: Open-source database; Electricity prices: Local bills, (B) PV: 1.2-4.1 kWp (households) and 100 kWp (plant) installed power; BESS: 4-6 kWh capacity	2020
[20]	Ireland	Different approaches to incentive microgrid development in smart communities			2022
[21]	China	Blockchain architecture for an EV-to-grid system which generates benefits for participants	360,000 EVs and 240 AGs	(A) Load: Randomly generated SoC for EVs, Electricity prices: different price periods during the day and incentives for frequency response, (B) EV battery: 40 KWh, EV charger: 7 kW	2022
This work	Chile	Sensitivity analysis of local P2P PV energy trading in a residential microgrid, allowing for an economic estimate within the current context (fixed pricing system, net metering, and solar resource)	4 households	(A) Load: Consumption profiles of 3.7 and 3 MWh/year from theoretical estimation, Electricity prices: Local bills, Weather data: Open-source database, (B) PV: 4.92 and 4.1 kWp installed power, BESS: 10.56 kWh capacity	2023

3.2 Study Cases of Smart Management of Thermal Loads in Microgrids

Historically, the electrical infrastructure has faced challenges associated with increasing energy demand. One solution has been the implementation of demand response (DR) plans, which involve converting electricity into thermal energy using Power-to-Heat (P2H) technologies. Currently, DR plans are primarily focused on small communities, leveraging real-time communication technologies, DERs, and ancillary services. These initiatives aim to enhance operational control of systems such as Thermal Energy Storages (TESs), Electric Water Heaters (EWHs), Heating, Ventilation, and Air Conditioning systems (HVACs), Thermostatically Controlled Loads (TCLs), and Heat Pumps (HPs). They address issues such as infrastructure capacity limits, real-time balancing, frequency response, load curtailment, and facilitate load shifting, peak load reduction, increased self-consumption, and demand flexibility. Additionally, these plans complement price-based programs and Time-of-Use (TOU) tariffs [25].

In [26], a flexibility model was proposed that aggregates demands from residential and non-residential buildings. A local retailer controls HVAC systems and smart appliances, optimizing load scheduling based on day-ahead market price predictions. Figure 3.4 shows the effect on the AC system consumption of changing the reference temperatures inside an office. In the upper graph, a low temperature set point results in higher cooling thermal load during the day but lower heating thermal load during the night. However, raising the set point temperature reduces cooling consumption and increases heating consumption during the cooling and heating cycles, respectively. Thus, regulating the set point temperature can be crucial for energy savings during certain periods of the day, depending on the objectives. Similarly, Figure 3.5 shows on the left an overheating cycle during winter inside an office, while on the right, an overcooling cycle for a summer day is depicted. These techniques can be applied as needed based on electricity prices under a variable pricing scheme, which generally have lower costs during non-critical or high solar irradiation periods and higher costs during critical or nighttime periods. Through proper demand aggregation, a demand flexibility ratio of up to 40% can be achieved. The optimal scheduling strategy shifts a portion of the demand from peak to off-peak periods while ensuring occupant's thermal comfort.

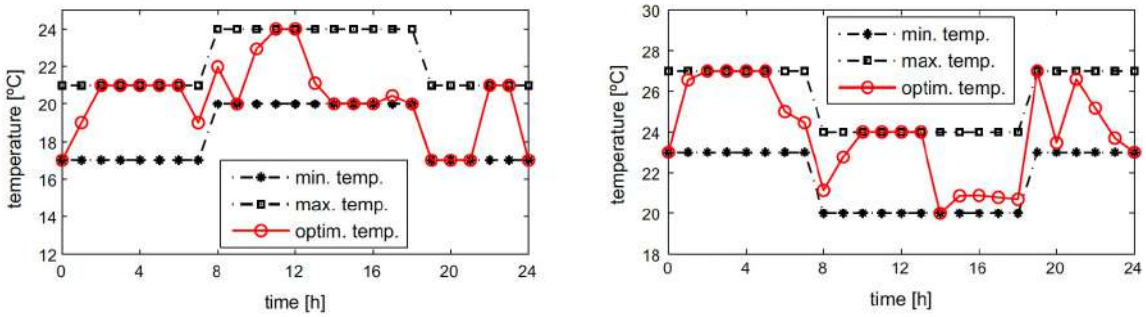

Figure 3.5: To the left, indoor temperature of an office building for a workday in winter. To the right, indoor temperature of an office building for a workday in summer [26].

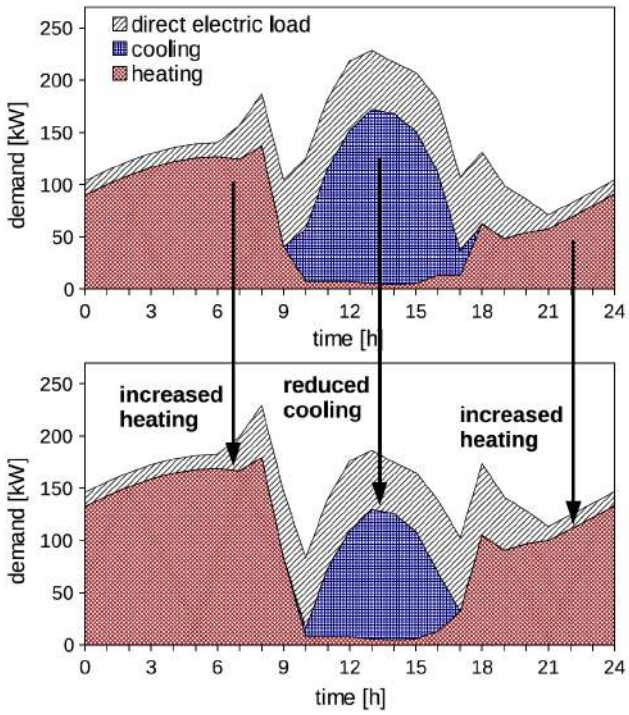

Figure 3.4: Energy demand of an office building on a workday with low indoor temperature reference (top) and high indoor temperature reference (bottom) [26].

On the other hand, references have been found focusing on P2P markets involving P2H operations at community level. In [27], a P2P model incorporating aggregated controls of residential EWH with TES is proposed, along with the implementation of a novel revenue for export response, which relies on real-time pricing conditions. The proposed method can increase aggregated PV self-consumption by 42% and reduce consumer's energy costs by 17%. Figure 3.6 shows the considerations of energy transfer for each household through simulations in TRNSYS and Python. The input data includes local weather data, base electrical load (excluding thermal loads), and DHW and cold water consumption profile. PV surpluses are managed by a logical control microprocessor, either to heat the water in the tank or to be injected into the UG. Figure 3.7 displays a graph of operation mode determination based on the heater SoC and electricity prices. The algorithm optimizes the operation based on costs, where demand or export response with the UG can be

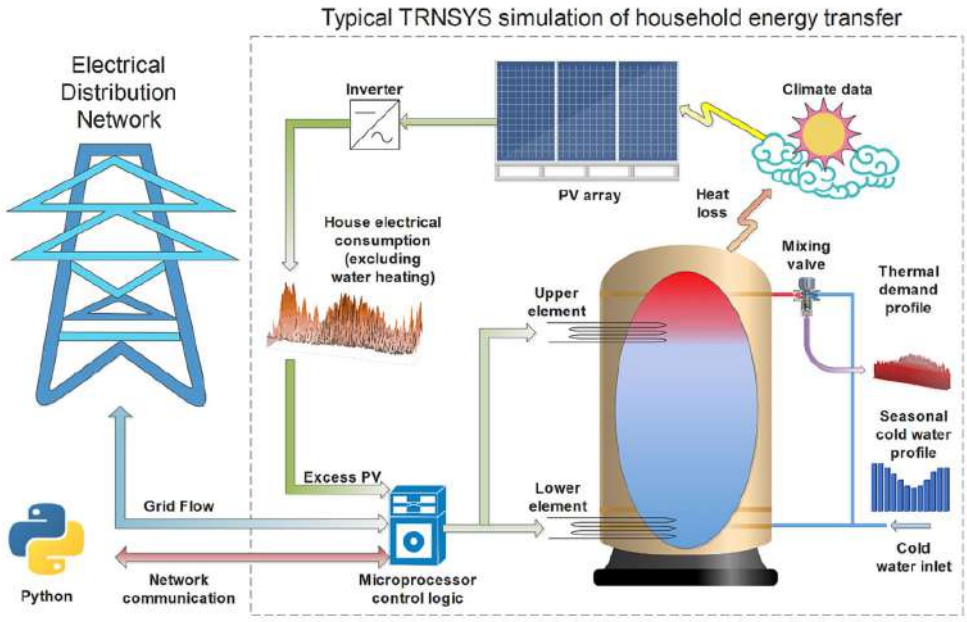

Figure 3.6: Representation of energy transfer considerations for each simulated household. The PV system was grid tied and net metered, such that excess PV was available for water heating or export to the grid [27].

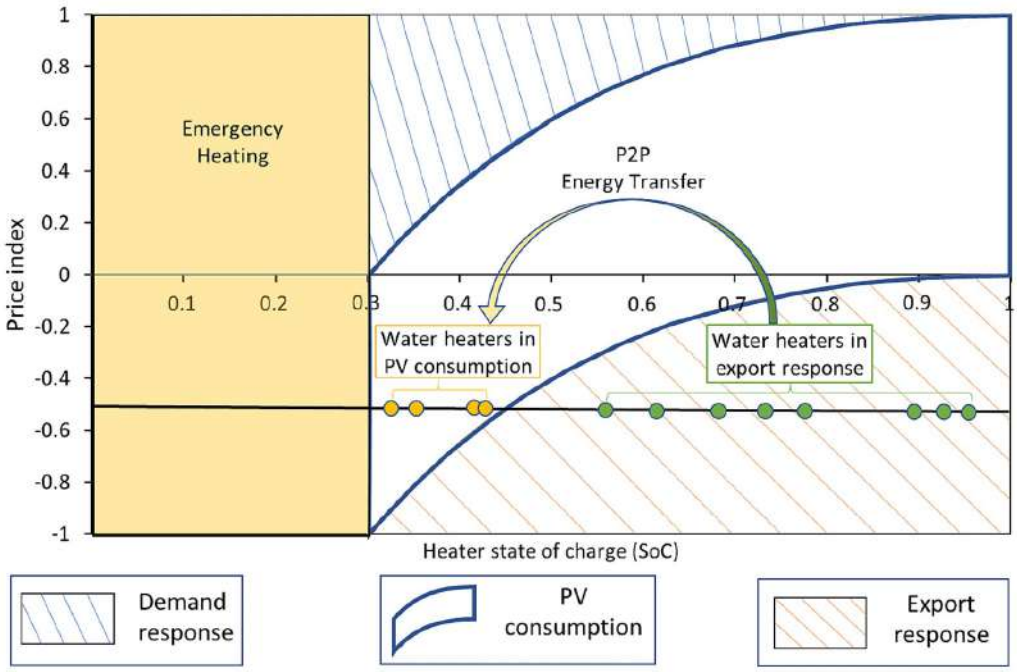

Figure 3.7: Operating mode determination for the electric water heater, based on demand/export response, PV consumption, emergency heating, price index and heater SoC [27].

applied, as well as selling surpluses in the P2P market. In [28], an analysis of building TES capability in P2P systems, and derivation of a time-varying virtual TES model to quantify its demand flexibility. The proposed method can reduce the prosumers costs by 3.7% and increase SCR by 3.1%.

In [29], the economic benefits of utilizing heat pumps demand flexibility through Local Energy Markets (LEMs) are examined, identifying factors that contribute to small economic benefits and the regulatory framework changes required to address them, such as high balancing costs and excessive taxes. The results showed that community annual costs can be reduced by 5.1% with a 40% penetration of HPs in the LEM. In [30], an energy management system for a commercial neighborhood is proposed, considering P2P trading, renewables-BESS sharing, and demand-side control of thermal loads and TESs. The model increases SSR and SCR by up to 22.8% and 11.3%, respectively, reduces annual operational costs by 24.6% and shifts peak demand from high-demand to high-generation periods, mitigating demand-supply mismatches. In [31], a P2P model is proposed for an electric-thermal network system, accommodating both supply and demand uncertainties. An aggregator equipped with a PV system, BESS for DR is included. Solar HP with TES is incorporated for prosumers, to supply DHW demand. The model decreases community energy costs by 26.7%, increases self-consumption by 61.8%, and reduces power fluctuations and peak loads. In [32], a P2P model with tariffs under the German levy regime is proposed. Representative RCs were modeled, considering Home Energy Management Systems (HEMSs), HPs, PV systems, BESSs, TESs, and DR. Suggestions are made for modifications to the Feed-in-Tariff (FiT) and transaction levies to make the model feasible. The model aims primarily to benefit consumers.

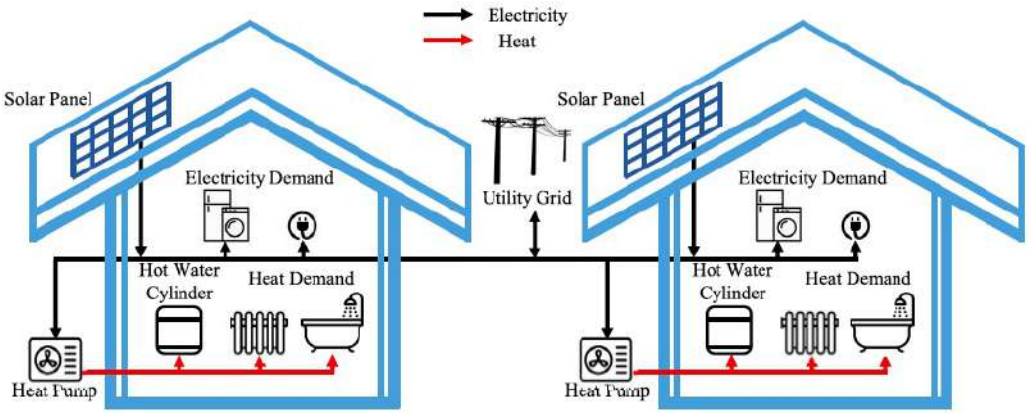

Figure 3.8: Schematic illustration of the P2P electricity trading between multi-energy prosumers [33].

Similarly, there are references such as [26], [33] and [34], that include the thermal comfort of occupants within the same line. In [33], a P2P model is proposed that considers HPs responding to retail electricity prices to supply heating loads and DHW demand, offering flexible indoor temperature control within comfort ranges, and incorporating a TES system. Figure 3.8 shows the proposed scheme, in where each prosumer is equipped with a PV system and other electrical and heating loads. The results showed that daily costs for RCs can be reduced by 41%, with TES complementing the heat supplied by the HP. In [34], a P2P model considering a community BESS, smart appliances, HVAC systems and thermal comfort through the PMV index is proposed. The model decreases community energy costs by up to 34.6% and reduces PV curtailment for prosumers. Other references such as [26] and [35], apply overcooling and overheating techniques of AC to maximize benefits. In [35], a P2P model to address power shortages is proposed. The

model considers online appliance scheduling, HVAC systems, thermal comfort and set point temperatures adjustment based on electricity prices. Depending on the demand flexibility of each RC, HVAC energy costs can be decreased by up to 26% and community energy costs by up to 36%.

3.3 Study Cases on the Application of Digital Twins in Residential Microgrids

The development of communication technologies, data science, and artificial intelligence has enabled the new resurgence of DTs during the last years. In [36], a chronological review on the development of DTs their variants, and applications is presented. Figure 3.9 shows that DTs are high-fidelity simulations that reflect states of a real-world system from the physical layer to a digital layer, based on historical data, real-time measurements, and physical models. Physical layer is composed by physical subsystems, such as electrical, thermal, or gas distribution networks, energy converters such as power-to-heat and power-to-gas devices, among others.

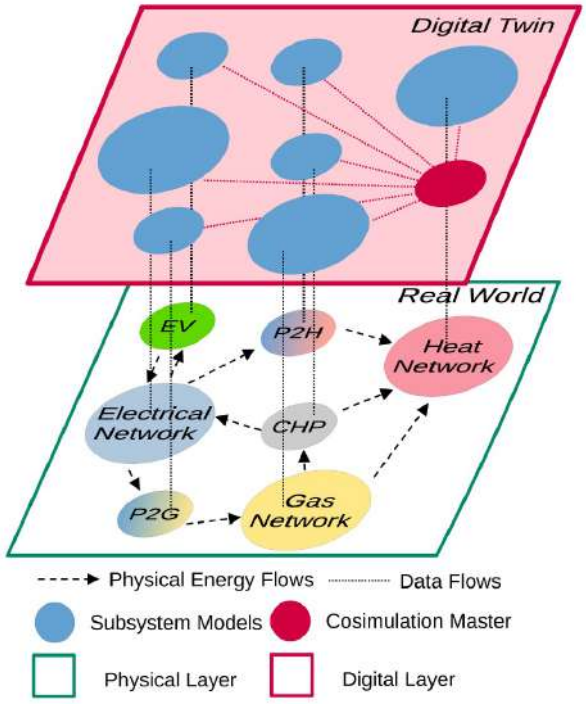

Figure 3.9: Digital twin in an integrated energy system. CHP: combined heat and power, EV: electric vehicle, P2H: power to heat, P2G: power to gas [36].

Lately, the concept of DT has been developed into a system composed of 5 layers: Real-space product, Virtual-space product, Connectivity, Data, and Services. These layers are periodically synchronized with real system data to maintain result fidelity. There are three main stages for DT applications, (1) design phase: which involves optimization, data generation and virtual evaluation, (2) operational phase: corresponding to project implementation, and (3) service phase [37].

Figure 3.10 depicts a schematic diagram of the operation of a DT within an application for conducting

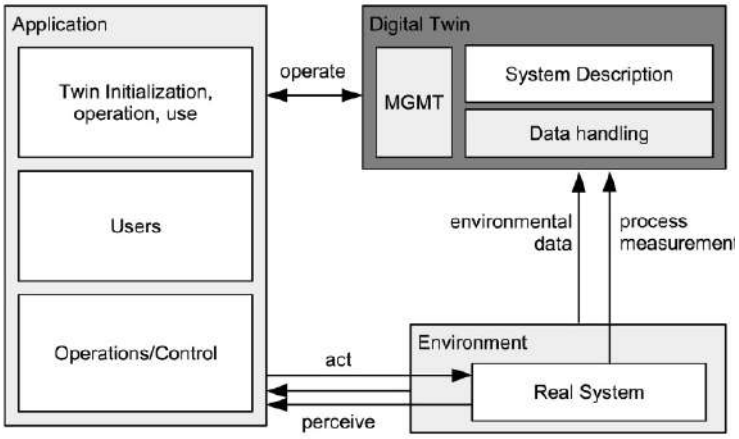

Figure 3.10: A digital twin system description enhanced with data flows. The digital twin gets updates from its enviroment and is used by an application. MGMT represent the system management [36].

operations and control by users. Both the DT layer and the application layer receive environmental data measured from the real system. The DT layer carries out a data handling stage to synchronize the real data with the data obtained in the system description stage, where operations and/or controls are optimized based on predictions from physics-based or data-driven models. On the other hand, users in the application layer can also interpret the measured data to conduct operations on the real system. Additionally, users can control and configure the DT as needed through the MGMT stage, such as initialization, start-ups, shutdowns, analysis of different scenarios, among others. This way, the DT assists users in decision-making in the real-world system.

Due to the wide range of specific applications where DTs can be implemented, they are commonly classified according to model fidelity and computing speed. Figure 3.11 illustrates a schematic diagram regarding this classification. Among the most basic models in terms of fidelity are dashboards, which describe states of the real system based on real-time measured data. Then, there are DTs based on stationary mathematical models, which can be used to optimize the design and/or sizing of real systems, placing less importance on computing speed, to DTs that rapidly predict future stationary behaviors for informed decision-making. Finally, there are dynamic DTs based on physics-based or data-driven models, which range from optimizing or describing transient processes in great detail, requiring high computational cost and low computing speed, as well as in anomaly detection in the real system by identifying divergences from model predictions, and lastly, in control applications, where future transient scenarios are predicted.

Case studies of DT implementation in communities with distributed renewable systems have been found. In [37], a DT is used in its design phase to replicate a city block, showing the results of a study on city renewal considering renewable sources for CO2 neutrality, HPs and EWHs. Local data was measured for simulations of energy demand and renewable supply, optimizing economic benefits, reducing total investment and greenhouse gas emissions. In [38], a model-based DT is proposed, integrating P2P trading, renewable sources, and price schemes such as bill sharing and mid-market rate. Transaction simulations in a replica minigrid quantify the impact on grid voltage and optimize BESS operation. The DT allows real-time testing of devices by interfacing simulation with the real system, reducing energy from the grid by 15.4% and individual bills by at least 11.3%.

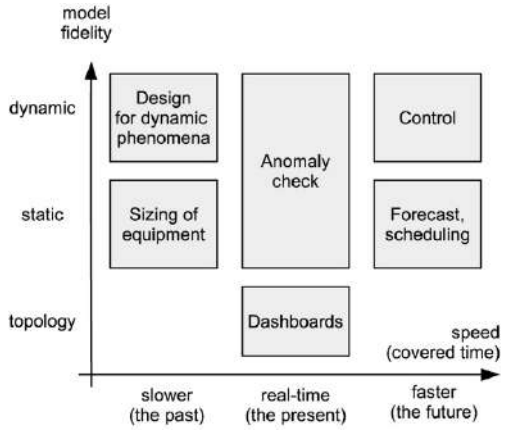

Figure 3.11: Usage of the different digital twin variants, depending on two of the dimensions to categorize digital twins, timing and model depth [36].

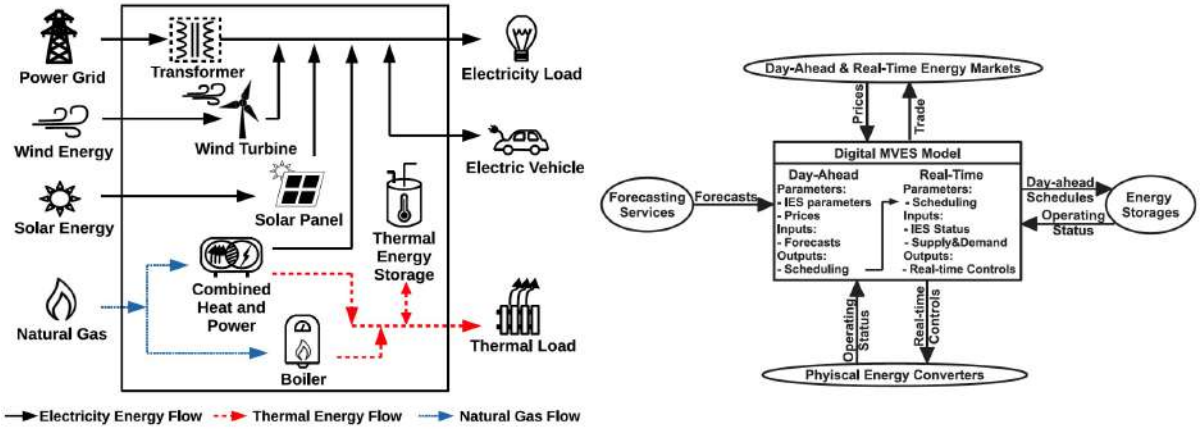

Figure 3.12: In the left, energy flows for a typical integrated energy system, which consist of transformers, wind turbines, solar panels, CHP systems, TESs, boilers and electric vehicles. In the right, data flows of a typical integrated energy system, where its virtual replica and physical devices form a DT system to interact with external enviroment [39].

In [39], a DT is proposed for an integrated energy system, considering day-ahead scheduling, renewable sources, and combined HPs and TESs. In the schematic diagram on the left of Figure 3.12, the flows corresponding to electrical, thermal, and natural gas distribution lines are observed. The real system is replicated in a digital multi-vector energy system model (MVES), fed by real-time measured data through Internet of Things (IoT) devices and 5G protocols (see schematic diagram on the right of Figure 3.12). Data is received from forecasting services (e.g., weather data), energy prices, and energy transactions in the market, as well as the operation and control states of energy storage systems and physical energy converters. With this information, MVES simulates, optimizes, and predicts future scenarios to achieve optimal control of renewable sources and energy converters, both in real-time and day-ahead. The DT enhances energy efficiency, reduces costs, and lowers CO2 emissions.

In [40], a DT was developed to assess energy efficiency indicators of buildings. Figure 3.13 shows the architecture of the DT, composed of the physical asset layer, the virtual model layer, and the operational assessment layer. In the physical layer, IoT devices are responsible for monitoring real-time data on energy consumption, while data on the level of information needs (LOIN), such as georeferenced data, building

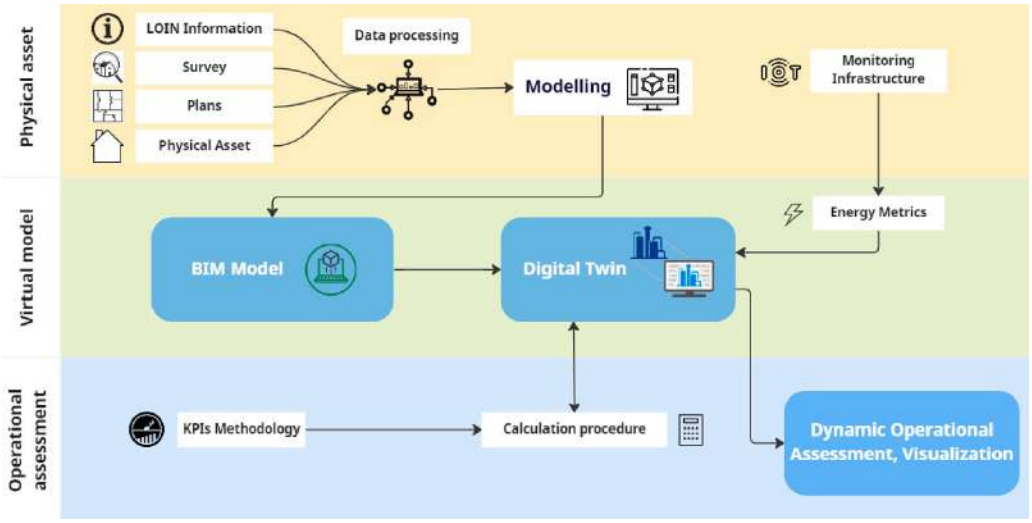

Figure 3.13: Operation assessment framework workflow [40].

dimensions and construction materials, as well as data from on-site surveys on the building's condition and technical plans, are collected and processed for a Building Information Modeling (BIM). In the virtual layer, the DT allows for spatial visualization of energy consumption metrics in real-time within the building's 3D modeling. Finally, in the operational assessment layer, users benefit from the DT through a visual interpretation of the measured data, aiding in decision-making and KPIs calculation.

Table 3.2 provides a summary of the analyzed case studies, highlighting the subsystems considered in the models. In Section 9, Table 9.1 summarizes the main contributions and results of the analyzed references, while Table 9.2 details the technical parameters of the subsystems, data collection methods, software used, among others. This reveals certain research gaps in the field. Firstly, there is a lack of studies on digital twins in the context of P2P markets, with no references integrating smart control of thermal loads and TESs through predictions from transient physics-based models and data-driven models, along with evaluating thermal comfort in this context. Secondly, sensitivity analysis studies are lacking, which would show how KPIs vary based on the sizing of AC systems, DHW tanks, and BESS. Lastly, there are no studies comparing results across different geographical locations with varying meteorological conditions and thermal insulation regulations at the residential level.

Table 3.2: References summary

Reference	[26]	[37]	[38]	[39]	[40]	[27]	[28]	[29]	[33]	[30]	[31]	[32]	[34]	[35]	Our
Year	2017	2023	2022	2022	2023	2024	2024	2024	2023	2022	2023	2020	2024	2021	Case
Digital Twin	x	✓	✓	✓	✓	x	x	x	x	x	x	x	x	x	✓
P2P markets	x	x	✓	x	x	✓	✓	✓	✓	✓	✓	✓	✓	✓	✓
PV systems	x	✓	✓	✓	x	✓	✓	✓	✓	✓	✓	✓	✓	✓	✓
BESS	x	✓	✓	✓	x	x	✓	✓	x	✓	✓	✓	✓	x	✓
Building parameters / Thermal inertia	✓	✓	x	x	✓	x	✓	x	✓	x	x	x	✓	x	✓
AC systems	✓	✓	x	✓	✓	x	✓	✓	✓	✓	x	✓	✓	✓	✓
Overcooling / Overheating	✓	x	x	x	x	x	x	x	x	x	x	x	x	✓	✓
Thermal comfort	✓	x	x	x	x	x	x	x	✓	x	x	x	✓	x	✓
DHW systems	x	✓	x	✓	✓	✓	✓	✓	✓	✓	✓	✓	x	x	✓
Thermal Storage	x	x	x	✓	x	✓	✓	✓	✓	✓	✓	✓	x	x	✓

4 | Methodology

4.1 Proposed Digital Twin Model

In this work, a DT scheme in its design phase is proposed for evaluating KPI in residential microgrids. Figure 4.1 shows the schematic diagram of the proposed DT model, which comprises a physical layer, a virtual layer, and a real-time operational assessment layer. The physical layer consists of monitoring data from physical systems, such as operational and technical parameters from DERs, base load corresponding to appliances and lighting, electricity prices from the UG, meteorological data, AC status, indoor temperature and humidity, occupancy status, building parameters, DHW tank status, DHW water temperature, and DHW demand. Local historical data were used to represent real-time monitoring of parameters from sensor nodes and measuring devices.

The virtual layer includes both physics-based sub-models, responsible for simulating and predicting the behavior of physical systems and the thermal comfort of occupants, and a data-driven sub-model that simulates P2P market behavior. The sub-models interact with each other through data fluxes. The HEMS is simulated by managing the outputs of each sub-model, executing smart thermal load management when required, and sending data on PV surpluses or electricity consumption to the P2P market aggregator. The P2P market sub-model then manages energy flows and monetary transactions between RCs and the UG. It also provides information on P2P market special offers for smart thermal load management in case of significant available surpluses. With these real-time simulations, the DT allows for real-time operational assessment, defining control mechanisms to implement smart thermal load management, BESS control, P2P market decisions, and obtaining KPIs for both RCs and the community.

On the other hand, the submodels that make up the virtual layer exchange data flows among themselves. Figure 4.2 presents the data flow diagram of the presented model. The RCs are simulated using physics-based models to simulate the behavior of PV systems, BESS, DHW tanks, and AC systems, in order to estimate relevant data such as local generation, energy stored in the BESS, thermal loads, energy imported/injected to the UG or to the P2P market, indoor temperatures, among others. The HEMS is simulated by managing the outputs of each submodel and carrying out smart thermal load management when required. The HEMS sends data on PV surpluses or electricity consumption to the P2P market aggregator. Then, the P2P market model manages energy flows between prosumers, consumers, and the UG, providing ancillary services to the RCs, providing them with information about energy traded in the P2P market, energy transferred with the UG, energy costs, and P2P market special offers to be able to carry out smart thermal load management in case there is a significant amount of surplus in the P2P market.

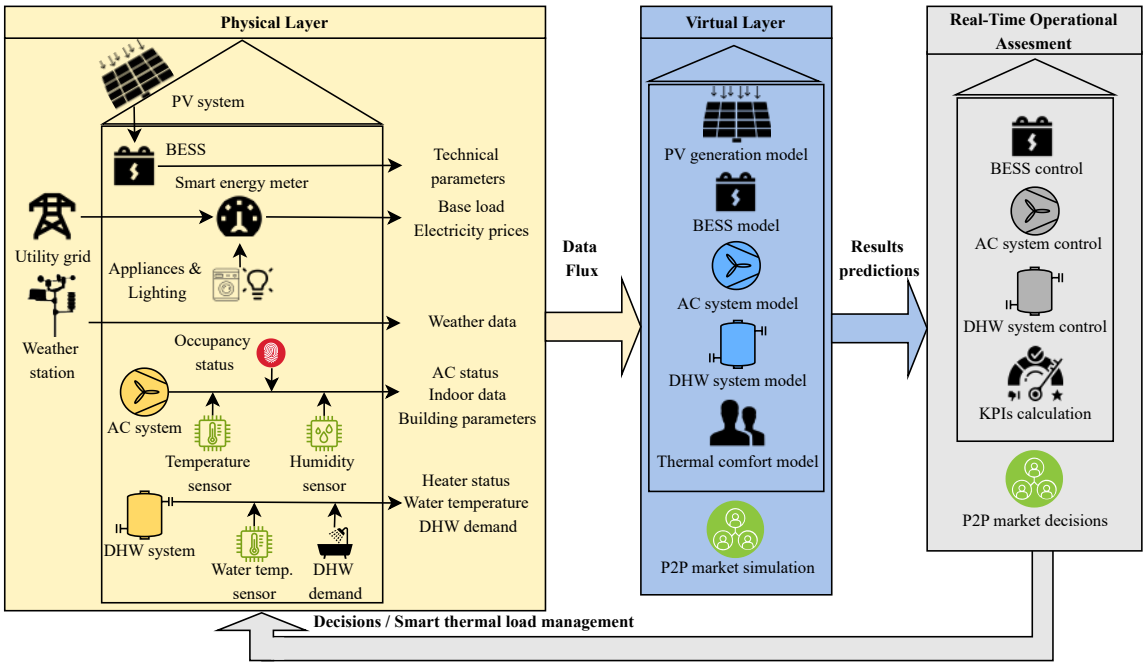

Figure 4.1: Schematic diagram of the proposed digital twin.

4.2 PV model

Local PV generation is calculated for prosumers. A control volume is defined at the photovoltaic panel as shown in Figure 4.3, which is formulated as given in (4.1).

$$\frac{\mathrm{dE_{CV}}}{\mathrm{dt}} = \mathrm{TG_t} - P_{pv} - Q_{rad} - Q_{conv} \tag{4.1}$$

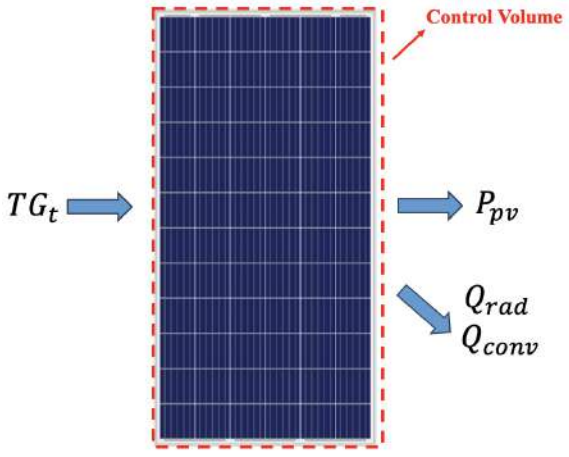

Figure 4.3: Control volume for energy balance in the PV panel.

where TG_t is the net shortwave solar irradiation, P_{pv} is the photovoltaic electrical generation, Q_{rad} is the heat transfer by radiation, and Q_{conv} is the heat transfer by convection. Meanwhile, TG_t is determined as

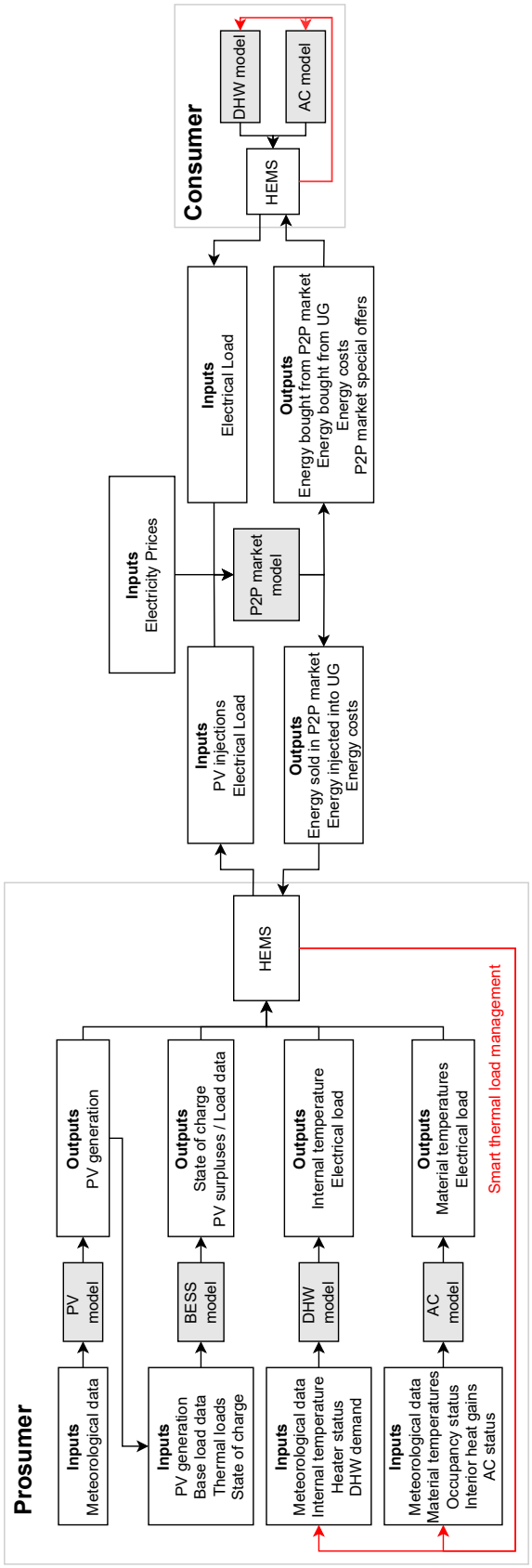

Figure 4.2: Main model and subsystems.

given in (4.2).

$$TG_t^i = G_t^i \cdot cos(\theta) \cdot (1 - \rho_{pv}) \cdot A_{pv} \tag{4.2}$$

where G_t is the incident solar irradiance, θ is the angle of incidence between the surface normal and the direction of sunlight, ρ_{pv} is the reflectivity of the panel, and A_{pv} is the effective area of the panel. Finally, the total generated energy is estimated after accounting for losses downstream of the photovoltaic panel, due to panel soiling, external shading, system unavailability, losses in DC wiring, inverter efficiency, and losses in AC wiring (see Figure 4.4).

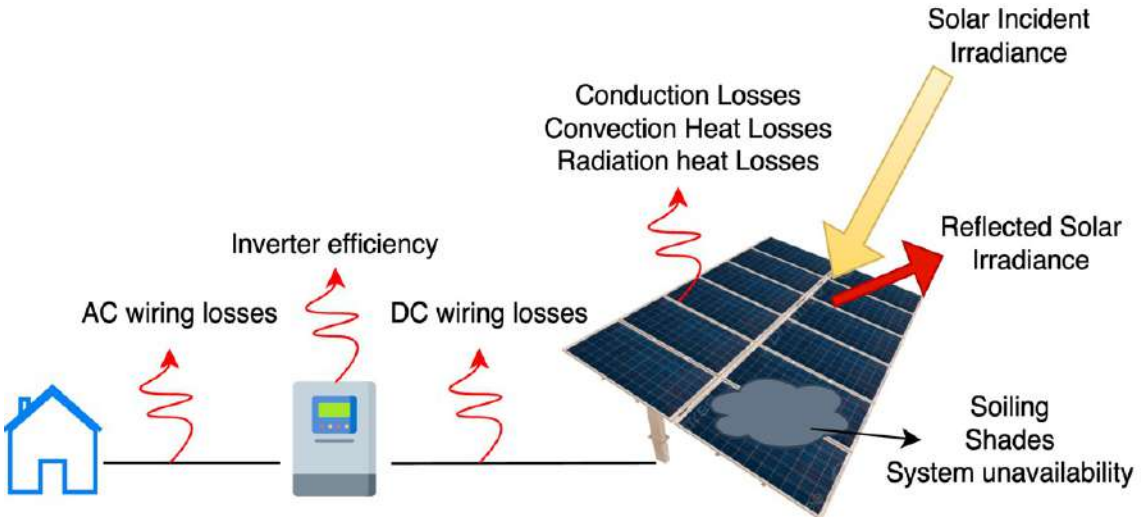

Figure 4.4: Energy balance in the PV model.

Table 4.1 summarizes the assumed parameters for PV systems, which were obtained from previous work [41]. The effective PV power generation (P_{PV}) at instant i is determined as given in (4.3).

$$\mathrm{P_{PV}^i} = \mathrm{N} \cdot \mathrm{L_f} \cdot \mathrm{Y^i} \cdot \left(\mathrm{TP_{PV}^i} + \mathrm{PL_t^i}\right) \tag{4.3}$$

where N represents the number of installed PV panels, L_f represents the system power loss factor, encompassing losses due to dust, shading, and electrical wiring, Y denotes the guaranteed yield of PV panels by the manufacturer, TP_{PV} signifies power generation without factoring in losses, and PL_t accounts for power losses attributed to thermal effects in PV panels. TP_{PV} is determined as given in (4.4).

$$\mathrm{TP_{PV}^i} = \mathrm{G_t^i} \cdot \mathrm{EA_{PV}} \cdot \mathrm{n_{PV}} \tag{4.4}$$

meanwhile, PL_t is determined as given in (4.5).

$$\mathrm{PL_t^i} = \frac{\mathrm{PTC}}{100} \cdot \left(\mathrm{CT^i} - \mathrm{NOCT}\right) \cdot \mathrm{TP_{PV}^i} \tag{4.5}$$

where PTC represents the loss coefficient attributed to variations in PV cell temperature concerning $NOCT$, and CT denotes the cell temperature of the PV panel, which is determined as given in (4.6).

$$\mathrm{CT^i} = \mathrm{T_a^i} + \frac{\alpha \cdot \mathrm{G_t^i}}{\mathrm{U}} \cdot (1 - \mathrm{n_{PV}}) \tag{4.6}$$

PV systems were dimensioned based on the day with the highest load during of the year, as given in (4.7) [41].

$$\mathrm{N} = \frac{L_{cr}}{E_{cr}} \tag{4.7}$$

where L_{cr} represents the highest daily load in the year, and E_{cr} is the energy generated by a panel on that critical day.

Table 4.1: PV Generation Parameters [41], [42].

Parameter	Value	Unit
Incident global irradiance (G_t)	Database[a]	W/m^2
Ambient Temperature (T_a)	Database[a]	$°C$
Thermal losses factor (U)	29	$W/(m^2°C)$
PV system losses factor (L_f)	0.7	-
PV panel efficiency (n_{PV})	20	%
PV panel rated power (RP_{PV})	410	Wp
Effective PV area of the panel (EA_{PV})	1.81	m^2
Absorption coefficient (α)	0.9	-
Temperature variation loss coefficient (PTC)	-0.36	$\%/°C$
Rated PV cell temperature ($NOCT$)	45	$°C$
Yield loss due to panel degradation (Y_L)	-0.64	$\%/year$
Initial Yield guaranteed by manufacturer (Y_0)	97	%

[a]From local database [42].

4.3 BESS model

The dimensioning of BESS was carried out as given in (4.8) [43].

$$RC_{BESS} = \max_{0 \le k \le TNP} \left(\sum_{i=0}^{j} L^i - \sum_{i=0}^{j} P_{PV}^i \right) \tag{4.8}$$

where TNP denotes the periods that commence and conclude at moments when local generation P_{PV}^i equals the load L^i. In simpler terms, these are time intervals where L^i exceeds P_{PV}^i. Consequently, j represents the number of time steps within the k^{th} period. Consequently, the required capacity of the BESS (RC_{BESS}) corresponds to the highest value of the difference between the total load and local generation across all periods. Figure 4.5 shows the control volume established to determine the energy balance in the BESS.

ΔP indicates the energy charged or discharged from the BESS, while thermal losses to the surroundings correspond to standby losses or losses due to charging and discharging efficiencies.

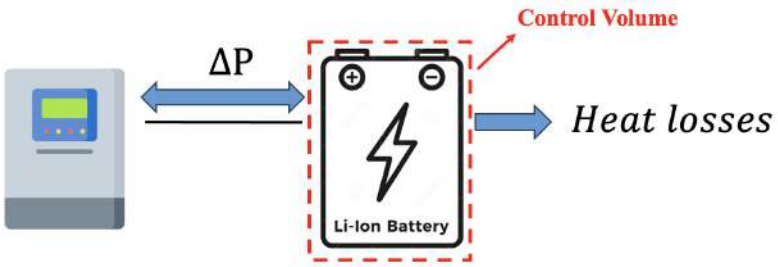

Figure 4.5: Energy balance in the BESS model.

Table 4.2 summarizes the assumed parameters for the BESS, derived from previous work.

Table 4.2: BESS Parameters For RCs [41], [44].

Parameter	Value	Unit
Technology	Lithium-ion	-
Useful Life	4500/~12.3	cycles/~years
Battery bank capacity (B_c)	10.56	kWh
Standby losses (S_l)	1	%/h
Initial state of charge (SoC)	20	%
Maximum/minimum SoC (Ma_s/Mi_s)	99/20	%
Charging/discharging efficiencies (C_e/D_e)	90/90	%
Maximum charging/discharging power (M_c/M_d)	30/30	% of total capacity

4.4 P2P market model

4.4.1 Proposed scheme

The proposed scheme corresponds to an adaptation of the architecture proposed in [21]. Although the architecture was developed for the trade of energy from electric vehicles, the architecture has a modular design that can be applied and adapted to different scenarios. Figure 4.6 shows the main entities of the P2P energy trading system. The primary participants include the UG, AGs, and RCs (consumers and prosumers with PV systems with or without BESS). The UG establishes energy contracts with the AGs, whereas the latter maintain contracts with RCs and oversee the coordination of the P2P market. The direction of the flows indicates the payments that are being made.

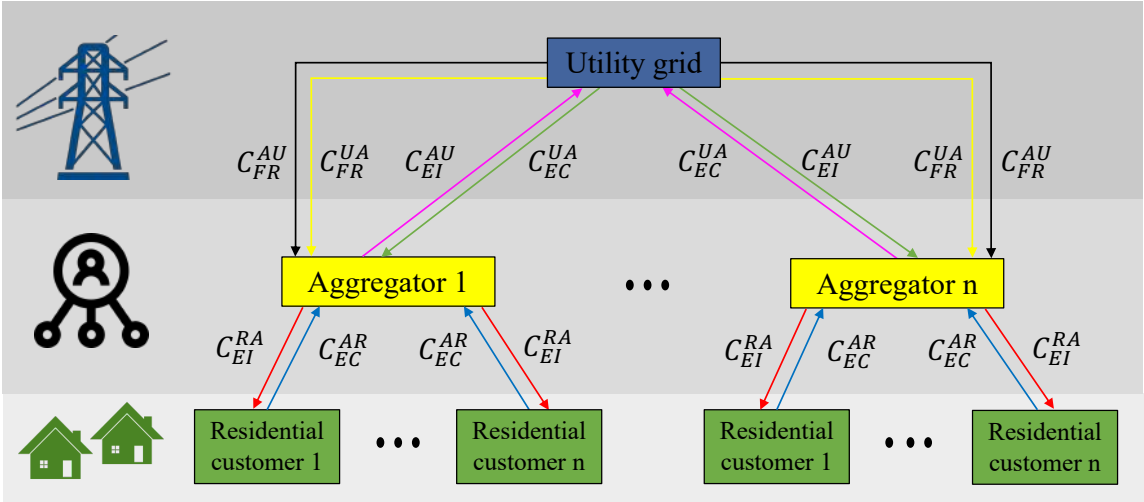

Figure 4.6: Schematic diagram illustrating the main entities of the P2P Trading System.

4.4.2 Residential customer trading contracts

RCs are responsible for paying their energy consumption to their AG, whereas the AG must compensate RCs for their energy injections. The total cost C_T^R for a RC is determined as given in (4.9).

$$\mathrm{C_T^R(t) = C_{EC}^{AR}(t) - C_{EI}^{RA}(t)} \tag{4.9}$$

where C_{EC}^{AR} and C_{EI}^{RA} represent the costs of energy consumption and energy injection to AG, respectively. C_{EC}^{AR} is determined as given in (4.10).

$$\begin{aligned}\mathrm{C_{EC}^{AR}(t)} = &\int_{t_s}^{t_e} \mathrm{r_C(t) \cdot P_{PC}^{AR}(t) \cdot W_{EC}^{PR}\, dt} + \\ &\int_{t_s}^{t_e} \mathrm{\left(1 - r_C(t)\right) \cdot P_{PC}^{AR}(t) \cdot W_{EC}^{UR}\, dt}\end{aligned} \tag{4.10}$$

where t_s represents the initial instant and t_e represents the end of the defined time interval, r_C denotes the fraction of energy consumed from the AG that is imported from the P2P market, while the remainder is imported from the UG. P_{PC}^{AR} represents the power consumed from the AG, W_{EC}^{PR} is the unit price of energy imported from the P2P market and W_{EC}^{UR} is the unit price of energy imported from the UG. Additionally, C_{EI}^{RA} is determined as given in (4.11).

$$\begin{aligned}\mathrm{C_{EI}^{RA}(t)} = &\int_{t_s}^{t_e} \mathrm{r_I(t) \cdot P_{PI}^{RA}(t) \cdot W_{EI}^{RP}\, dt} + \\ &\int_{t_s}^{t_e} \mathrm{\left(1 - r_I(t)\right) \cdot P_{PI}^{RA}(t) \cdot W_{EI}^{RU}\, dt}\end{aligned} \tag{4.11}$$

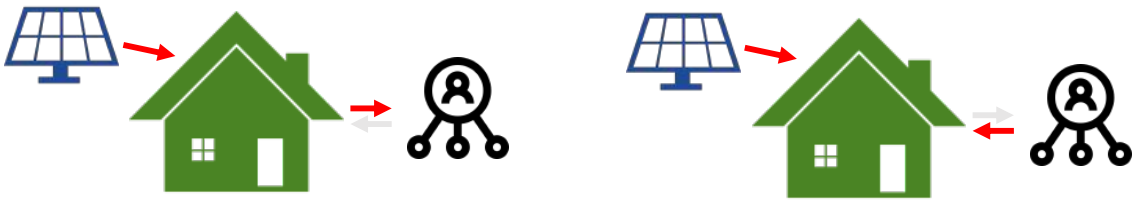

(a) Decision A. **(b)** Decision B.

Figure 4.7: Schematic diagram illustrating potential HEMS decisions for prosumers without BESS.

where r_I represents the fraction of energy injected into the AG that is sold in the P2P market, while the remainder is injected into the UG. P_{PI}^{RA} represents the power injected into the AG, W_{EI}^{RP} is the price of energy sold in the P2P market, and W_{EI}^{RU} is the price of energy injected into the UG.

4.4.2.1 HEMS algorithms

HEMS determine power transactions with the AG (represented as P_{PC}^{AR} and P_{PI}^{RA}) and self-consumption (S_c), using input parameters such as local generation (P_{PV}), load (L) and BESS state of charge (SoC). Two distinct HEMS algorithms are employed, one designed for prosumers with BESS and another for those without. Algorithm 1 summarises the logic behind a HEMS designed for prosumers without BESS. The inputs are P_{PV} and L, whereas the outputs include P_{PC}^{AR}, P_{PI}^{RA}, and S_c. At each time step (t), two possible decisions are considered depending on the presence of power surpluses or deficits (see Fig. 4.7).

Algorithm 1 HEMS algorithm for prosumers without BESS.

Input: P_{PV}, L
Output: P_{PC}^{AR}, P_{PI}^{RA}, S_c
1: **for** $t = 0$ to T **do**
2: **if** $P_{PV} \geq L$ **then**
3: A: $P_{PC}^{AR} = 0$; $P_{PI}^{RA} = P_{PV} - L$; $S_c = L$
4: **else**
5: B: $P_{PC}^{AR} = L - P_{PV}$; $P_{PI}^{RA} = 0$; $S_c = P_{PV}$
6: **end if**
7: **end for**

Algorithm 2 summarises the logic behind a HEMS for prosumers with BESS. The inputs correspond to P_{PV}, L, and SoC, whereas the outputs include P_{PC}^{AR}, P_{PI}^{RA}, S_c and SoC. At each time step (t), seven possible decisions are considered depending on the availability of surplus power, power deficits, and BESS constraints (see Fig. 4.8).

4.4.2.2 Proposed electricity price market

In Chile, while the distribution sector is intended to be competitive, there are only two main distribution companies that serve the majority of customers. The purchase of long-term contracts helps the distribution companies maintain the market power. This directly impacts customers, as distribution companies play the dual role of both distributor and retailer, explaining why fixed prices persist. To determine the prices of consumed energy (W_{EC}^{PR}) and injected energy (W_{EI}^{RP}) into the P2P market, as well as the prices of consumed energy (W_{EC}^{UR}) and injected energy (W_{EI}^{RU}) into the UG, two scenarios were established based on market availability (see Table 4.3). If the P2P market is unavailable, energy prices are determined by the local UG

Algorithm 2 HEMS algorithm for prosumers with BESS.

Input: P_{PV}, SoC, L
Output: $P_{PC}^{AR}, P_{PI}^{RA}, S_c, SoC$

for $t = 0$ to T **do**
  $SoC' = SoC - S_l$
  if $P_{PV} \geq L$ **then**
    $\Delta P = P_{PV} - L$; $P_{PC}^{AR} = 0$; $S_c = L$
    if $\frac{B_c M_c}{100} \geq \Delta P$ **then**
      if $SoC' + \frac{C_e \Delta P}{B_c} \leq Ma_s$ **then**
        A: $P_{PI}^{RA} = 0$; $SoC = SoC' + \frac{C_e \Delta P}{B_c}$
      else
        B: $P_{PI}^{RA} = \Delta P - \frac{B_c (Ma_s - SoC')}{100}$; $SoC = SoC' + \frac{C_e (Ma_s - SoC')}{100}$
      end if
    else
      if $SoC' + \frac{C_e M_c}{100} \leq Ma_s$ **then**
        C: $P_{PI}^{RA} = \Delta P - \frac{B_c M_c}{100}$; $SoC = SoC' + \frac{C_e M_c}{100}$
      else
        B
      end if
    end if
  else
    $\Delta P = L - P_{PV}$; $P_{PI}^{RA} = 0$
    if $\frac{B_c M_d}{100} \geq \Delta P$ **then**
      if $SoC' - \frac{\Delta P \cdot 100^2}{B_c D_e} \geq Mi_s$ **then**
        D: $P_{PC}^{AR} = 0$; $S_c = L$; $SoC = SoC' - \frac{\Delta P \cdot 100^2}{B_c D_e}$
      else
        if $SoC' \geq Mi_s$ **then**
          E: $P_{PC}^{AR} = \Delta P - \frac{B_c (SoC' - Mi_s) D_e}{100^2}$; $S_c = P_{PV} + \frac{B_c (SoC' - Mi_s) D_e}{100^2}$; $SoC = Mi_s$
        else
          F: $P_{PC}^{AR} = \Delta P$; $S_c = P_{PV}$; $SoC = SoC'$
        end if
      end if
    else
      if $SoC' - \frac{B_c M_d}{100} \geq Mi_s$ **then**
        G: $P_{PC}^{AR} = \Delta P - \frac{B_c M_d D_e}{100^2}$; $S_c = P_{PV} + \frac{B_c M_d D_e}{100^2}$; $SoC = SoC' - \frac{B_c M_d}{100}$
      else
        if $SoC' \geq Mi_s$ **then**
          E
        else
          F
        end if
      end if
    end if
  end if
end for

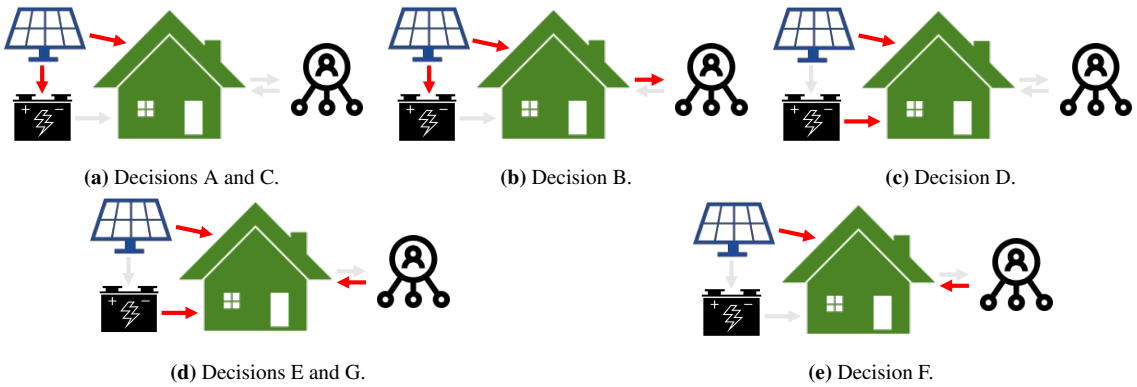

(a) Decisions A and C. **(b)** Decision B. **(c)** Decision D.

(d) Decisions E and G. **(e)** Decision F.

Figure 4.8: HEMS decision options for prosumers with BESS. a) Local generation covers the load, and surplus is stored in the BESS. b) A fraction of local generation covers the load, another fraction fully charges the BESS, and surplus is injected into the AG. c) Fraction of the load is supplied by local generation, and the rest comes from the BESS. d) The load is partially met by local generation, BESS, and the AG. e) Fraction of the load is covered by local generation, while the rest is provided by the AG.

Table 4.3: Electricity Costs for RCs [45].

Market status	Parameter	Value	Unit
P2P unavailable	Imported energy from the UG	0.17	USD/kWh
	Injected energy into the UG	0.10	USD/kWh
P2P available	Imported energy from the AG	0.16	USD/kWh
	Injected energy into the AG	0.14	USD/kWh
	Special import/injection price	0.15	USD/kWh

[45]. A dolar value equivalent to 972 CLP is assumed. However, if the P2P market is available, prices are set by the AG. Additionally, to encourage P2P transactions and promote smart thermal load management among consumers, the aggregator offers a special purchase and sale price.

Figure 4.9 illustrates the community's total energy costs as a function of PV penetration in a local microgrid. Four different market price scenarios were analyzed using electricity market price data from [11], Conventional Method (CM), Bill Sharing (BS), Mid-Market Rate (MMR) and Auction-based Pricing Strategy (APS). For a 50% PV penetration in a microgrid, the MMR method shows lower energy costs for RCs. According to price data from an MMR market, fixed imported and injected energy prices into the P2P market are assumed to be 93% and 134% of the UG import and injection prices, respectively. Therefore, the P2P market enables RCs to engage in energy transactions by purchasing energy at a lower cost from other prosumers or selling PV surpluses at a higher price compared to transactions with the UG.

4.4.2.3 Special electricity price for P2P market

In order to incentivize the local utilization of generation surpluses, the AG offers a special price for consumers who wish to use smart thermal load management techniques. Figure 4.10 illustrates the potential allocation of a prosumer's surplus PV energy. Firstly, each household maintains a HEMS, responsible for managing energy loads within the home. Each HEMS is coordinated with other HEMS and the aggregator through a public communication network, while controlling local devices through a private local network. The HEMS is directly connected to the DC/AC Inverter, in order to define the priorities for the destination of PV surpluses. As priority (1), the household's base load is supplied, corresponding to appliances and lighting.

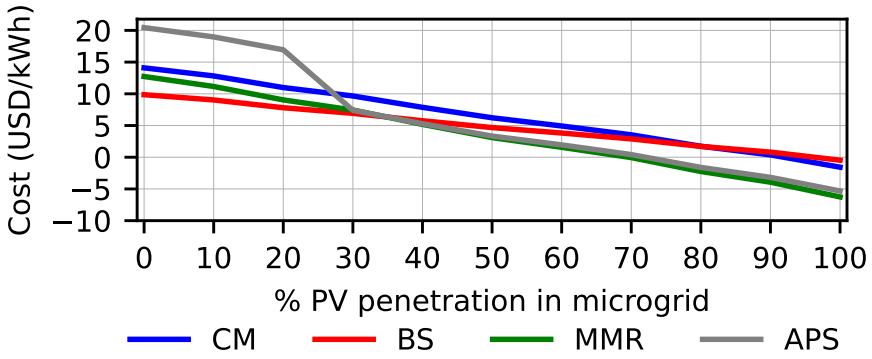

Figure 4.9: Community total energy cost v/s PV penetration in a local microgrid.

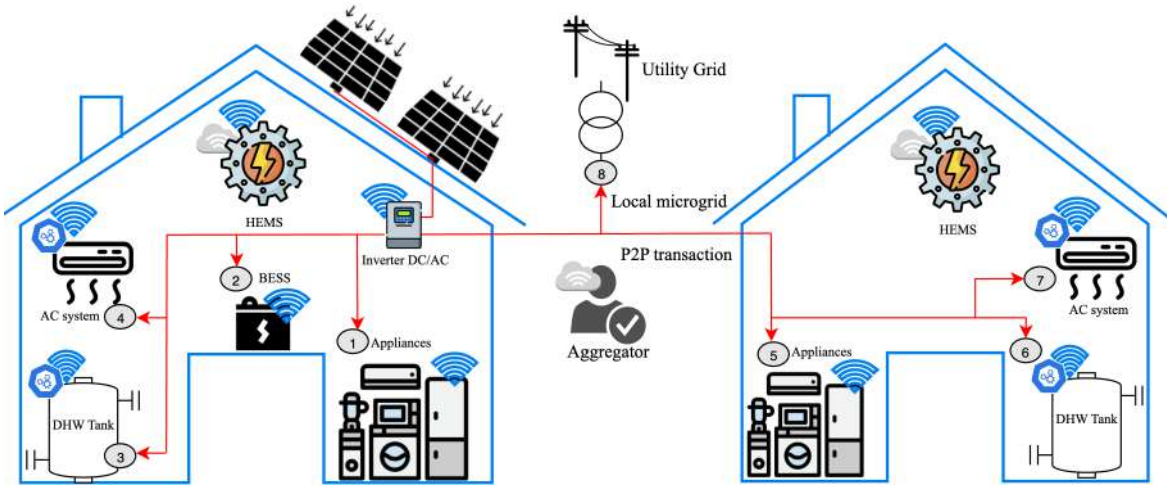

Figure 4.10: Cascade of self-consumption priorities for prosumers and consumers.

Then, (2) once the base load is supplied, surpluses are stored in the local BESS. Once the BESS reaches its maximum SoC, (3) thermal storage of surpluses in the local DHW tank is sought, heating the interior hot water. If the DHW tank reaches its maximum operating temperature, (4) the AC system is controlled to apply overheating/overcooling techniques. If all local loads have been met, then (5) the option of energy transfer to other households appears, where consumers will prioritize supplying their base load from the P2P market. Once the base load is supplied, they then (6) opt to store in the DHW tank and subsequently (7) intelligently control the AC system. If the local loads of the microgrid have been completely supplied, then (8) as a last resort, surplus injection into the UG is considered.

4.4.3 AG trading contracts

AGs act as intermediaries between RCs and the UG, generating profits through the coordination of energy transactions within the P2P market. This involves purchasing energy from prosumers at a lower cost than the selling price to RCs within the P2P market, while also receiving incentives from the UG for frequency response (FR) participation. Algorithm 3 summarises the management of power flows between the AG, the UG, and RCs. The inputs include the time step (Δt), P_{PC}^{AR} and P_{PI}^{RA} for each RC, as well as the electricity prices from Table 4.3. The outputs consist of C_T^R for each RC, $\mathrm{P}_{\mathrm{PI}}^{\mathrm{AU}}$ and $\mathrm{P}_{\mathrm{PC}}^{\mathrm{UA}}$. At each time step t, three possible

decisions are considered depending on the presence of surplus power and power deficits within the P2P market (see Fig. 4.11).

Algorithm 3 AG decision algorithm.

Input: Δt, $P_{PC}^{AR}(i_R)$, $P_{PI}^{RA}(i_R)$, W_{EC}^{PR}, W_{EI}^{RP}, W_{EC}^{UR}, W_{EI}^{RU}
Output: $C_T^R(i_R)$, P_{PI}^{AU}, P_{PC}^{UA}

for $t = 0$ to T **do**
  if $\Sigma P_{PI}^{RA}(i_R) > 0$ **and** $\Sigma P_{PC}^{AR}(i_R) > 0$ **then**
    P2P market = Available
    if $\Sigma P_{PI}^{RA}(i_R) \geq \Sigma P_{PC}^{AR}(i_R)$ **then**
      A: $\mathrm{r_C} = 1; \mathrm{r_I} = \frac{\Sigma P_{PC}^{AR}(i_R)}{\Sigma P_{PI}^{RA}(i_R)}$
    else
      B: $\mathrm{r_C} = \frac{\Sigma P_{PI}^{RA}(i_R)}{\Sigma P_{PC}^{AR}(i_R)}; \mathrm{r_I} = 1$
    end if
  else
    P2P market = Unvailable
    C: $\mathrm{r_C} = 0; \mathrm{r_I} = 0$
  end if
  for i_R in RCs **do**
    $C_{EI}^{RA}(i_R) = P_{PI}^{RA}(i_R)(\mathrm{r_I} W_{EI}^{RP} + (1 - \mathrm{r_I}) W_{EI}^{RU})\Delta t$
    $C_{EC}^{AR}(i_R) = P_{PC}^{AR}(i_R)(\mathrm{r_C} W_{EC}^{PR} + (1 - \mathrm{r_C}) W_{EC}^{UR})\Delta t$
    $C_T^R(i_R) = C_{EC}^{AR}(i_R) - C_{EI}^{RA}(i_R)$
  end for
  $\mathrm{P_{PI}^{AU}} = (1 - \mathrm{r_I})\Sigma \mathrm{P_{PI}^{RA}(i_R)}$; $\mathrm{P_{PC}^{UA}} = (1 - \mathrm{r_C})\Sigma P_{PC}^{AR}(i_R)$
end for

The total cost of energy consumed by community from AG is determined as given in (4.12).

$$\mathrm{TC_{EC}^{AC}(t)} = \sum_{i_R=1}^{n} \mathrm{C_{EC}^{AR}(i_R, t)} \tag{4.12}$$

where n represents the number of RCs. Likewise, the total cost of energy injected from the community to the AG is determined as given in (4.13).

$$\mathrm{TC_{EI}^{CA}(t)} = \sum_{i_R=1}^{n} \mathrm{C_{EI}^{RA}(i_R, t)} \tag{4.13}$$

Also, the cost of energy injected from the AG to the UG is determined as given in (4.14).

$$\mathrm{C_{EI}^{AU}(t)} = \int_{t_s}^{t_e} \mathrm{P_{PI}^{AU}(t) \cdot W_{EI}^{RU}\, dt} \tag{4.14}$$

Similarly, the cost of energy consumed and paid by the AG to the UG is determined as given in (4.15).

$$\mathrm{C_{EC}^{UA}(t)} = \int_{t_s}^{t_e} \mathrm{P_{PC}^{UA}(t) \cdot W_{EC}^{UR}\, dt} \tag{4.15}$$

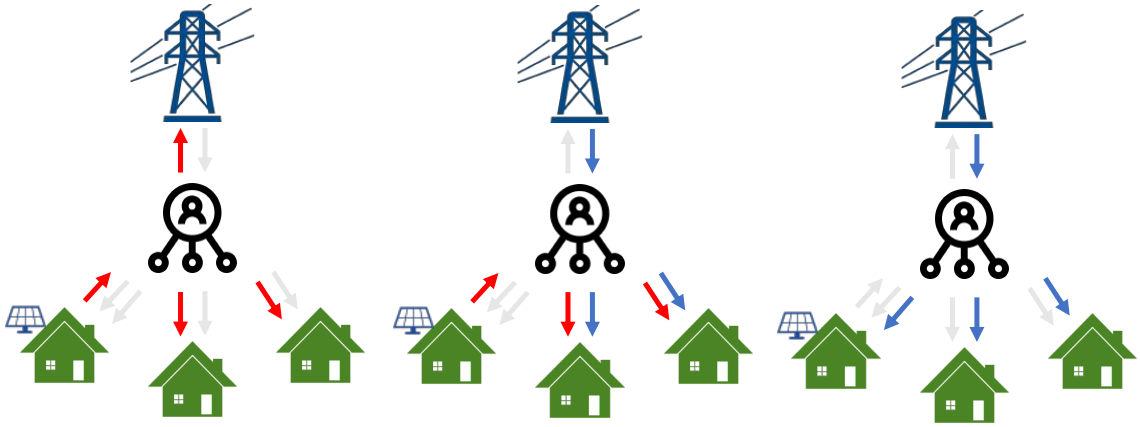

(a) Decision A. **(b)** Decision B. **(c)** Decision C.

Figure 4.11: Schematic diagram with possible AG decisions for energy transactions.

Table 4.4: Incentive Costs For The AG From The UG For FR.

Parameter	Value	Unit
Incentive cost by receiving (W^{UA}_{FRR})	0.02	USD/kWh
Incentive cost by injecting (W^{AU}_{FRI})	0.01	USD/kWh

Additionally, an economic incentive from UG to AG is proposed, involving the receipt or injection of energy during critical periods when FR is needed. The proposed incentive costs, as detailed in Table 4.4, are assumed to be 10% of the energy costs set by the UG. During periods when the current load on the UG is lower than the average load of the past week, an increase in demand is required to stabilize the grid frequency. Consequently, the UG rewards AGs that consume power during this period. This is determined as specified in (4.16).

$$C^{UA}_{FR}(t) = \int_{t_s}^{t_e} P^{UA}_{PC}(t) \cdot W^{UA}_{FRR}\, dt \tag{4.16}$$

Similarly, when the current load exceeds the average load of the past week, surplus power injections into the UG become necessary. Consequently, the UG will provide rewards to AGs that inject power during this period, determined as given in (4.17).

$$C^{AU}_{FR}(t) = \int_{t_s}^{t_e} P^{AU}_{PI}(t) \cdot W^{AU}_{FRI}\, dt \tag{4.17}$$

Finally, the total income for an AG is determined as given in (4.18).

$$\begin{aligned} TI_{AG}(t) = TC^{AC}_{EC}(t) + C^{AU}_{EI}(t) + C^{UA}_{FR}(t) + C^{AU}_{FR}(t) \\ -TC^{CA}_{EI}(t) - C^{UA}_{EC}(t) \end{aligned} \tag{4.18}$$

4.4.4 Grid trading contract

The total income for the UG is determined as given in (4.19).

$$TI_{UG}(t) = C_{EC}^{UA}(t) - C_{EI}^{AU}(t) - C_{FR}^{UA}(t) - C_{FR}^{AU}(t) \tag{4.19}$$

4.5 DHW Model

The model of TES for DHW is an adaptation of [46] and [47] (see Fig. 4.12). The model considers a control volume that corresponds to the internal volume of the water tank. At each time step i, the model considers the input of a mass flow rate of water $\dot{m}^i_{in}$ at a temperature IT^i_{dhw} and the output of a mass flow rate of water $\dot{m}^i_{out}$ at an average temperature T^i_{dhw}. The model assumes an internally unstratified mass of water, meaning that the entire internal volume of water is fully mixed and at the same temperature. Inside the tank, there is an electric coil that provides heat at a power P^i_{dhw}, and thermal losses due to heat transfer to the outside are considered Q^i_{loss}.

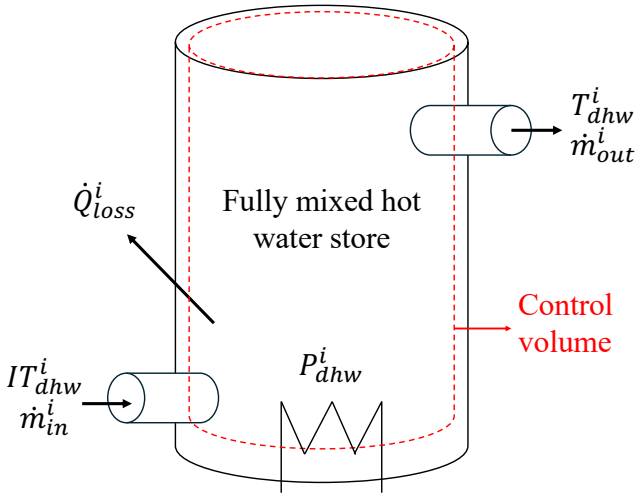

Figure 4.12: Unstratified hot water storage tank.

A one-dimensional transient heat conduction model is proposed with two nodes, one for the internal water and the other for the outdoor air [48]. The mass balance for the established control volume is determined as given in (4.20).

$$\frac{dm_{CV}}{dt} = \dot{m}_{in} - \dot{m}_{out} = 0 \tag{4.20}$$

Where the mass flow rates $\dot{m}_{in}$ and $\dot{m}_{out}$ are assumed to be equal at all times, so there is no change in the internal mass in the control volume. In other words, at each time instant, the mass of water extracted from the tank is equal to the mass of water injected from the supply. On the other hand, the energy balance for the established control volume is determined as given in (4.21).

$$\frac{dE_{CV}}{dt} = \sum \dot{Q} + \dot{E}_{dhw} \tag{4.21}$$

Where $\sum \dot{Q}$ corresponds to the heat transfer through the surfaces, $\dot{E}_{dhw}$ is the heat contribution from the electric coil, which will correspond to the power of the heater P_{dhw}. The rate of change of internal energy is determined as given in (4.22).

$$\frac{dE_{CV}}{dt} = \rho_w V_{dhw} c_w \frac{dT_{dhw}}{dt} \tag{4.22}$$

Where ρ_w is the density of water at the average internal temperature, V_{dhw} is the internal volume, c_w is the specific heat of water at the average internal temperature, and $\frac{dT_{dhw}}{dt}$ is the rate of change of the average internal temperature. On the other hand, the heat flows through the control volume surfaces are determined as given in (4.23).

$$\sum \dot{Q} = \dot{Q}_{in} - \dot{Q}_{out} - \dot{Q}_{loss} \tag{4.23}$$

Where $\dot{Q}^i_{loss}$, $\dot{Q}^i_{in}$ and $\dot{Q}^i_{out}$ are the heat flow through the tank walls, the inlet duct and the outlet duct, respectively, which are determined as given in (4.24),(4.25) and (4.26), respectively.

$$\dot{Q}_{in} = c_w \dot{m}_{dhw} IT_{dhw} \tag{4.24}$$

$$\dot{Q}_{out} = c_w \dot{m}_{dhw} T_{dhw} \tag{4.25}$$

$$\dot{Q}_{loss} = U_{dhw} A_{dhw} (T_{dhw} - T_a) \tag{4.26}$$

Where $\dot{m}_{dhw}$ is the mass flow, IT_{dhw} is the inlet water flow temperature, T_{dhw} is the outlet water flow temperature, T_a is the ambient temperature, A_{dhw} is the surface area of the tank and U_{dhw} is the tank thermal transmittance. In this way, equation 4.21 can be expressed in terms of equation 4.27. Subsequently, applying finite differences to discretize explicitly, equation 4.28 is obtained.

$$\rho_w V_{dhw} c_w \frac{dT_{dhw}}{dt} = c_w \dot{m}_{dhw} IT_{dhw} - c_w \dot{m}_{dhw} T_{dhw} - U_{dhw} A_{dhw} (T_{dhw} - T_a) + P_{dhw} \tag{4.27}$$

$$\frac{\rho_w V_{dhw} c_w (T^{i+1}_{dhw} - T^i_{dhw})}{\Delta t} = c_w \dot{m}^i_{dhw} IT^i_{dhw} - c_w \dot{m}^i_{dhw} T^i_{dhw} - U_{dhw} A_{dhw} (T^i_{dhw} - T^i_a) + P^i_{dhw} \tag{4.28}$$

Finally, using equation 4.29, an iterative process is applied to obtain the average internal temperature in the tank for each time step. Table 4.5 summarizes the parameters used.

$$T^{i+1}_{dhw} = \frac{\Delta t}{\rho_w V_{dhw} c_w} \left(c_w \dot{m}^i_{dhw} (IT^i_{dhw} - T^i_{dhw}) - U_{dhw} A_{dhw} (T^i_{dhw} - T^i_a) + P^i_{dhw} \right) + T^i_{dhw} \tag{4.29}$$

4.5.1 DHW tank parameters

Commercially available hot water storage tank parameters were obtained from [49] (see Fig. 9.1). Table 4.5 summarizes the technical parameters of the tanks used according to their storage capacity.

Table 4.5: Parameters.

Parameter	Value	Unit	Section
Water density (ρ_w)	1000	kg/m^3	-
Water specific heat (c_w)	4183	$J/(kg \cdot K)$	-
Water initial temperature (T_{w0})	65	$°C$	-
Air external velocity (W_v)	0.1	m/s	-
Air kinematic viscosity (ν_a)	$1.4 \cdot 10^{-5}$	m^2/s	-
Air dynamic viscosity (μ_a)	$1.8 \cdot 10^{-5}$	$kg/(m \cdot s)$	-
Air specific heat (c_a)	1007	$J/(kg \cdot K)$	-
Air thermal conductivity (k_a)	0.025	$W/(m \cdot K)$	-
Dry bulb ambient temperature (T_a)	Database	$°C$	Defined in section 4.5.4
DHW mass flux ($\dot{m}_{dhw}$)	Calculated	kg/s	Defined in section 4.5.2
Litres of DHW supplied (L_{wsup})	Database	L/s	Defined in section 5.6
DHW supply temperature (T_{wsup})	45	C	Defined in section 5.6
Commercial tank parameters according to capacity (100L, 200L, 300 L)			
Internal volume (V_{dhw})	[0.1, 0.2, 0.3]	m^3	Defined in section 9.1
Average surface (A_{dhw})	[1.48, 2.36, 2.91]	m^2	Defined in section 9.1
Electric coil rated power (P_{dhw})[a]	[1.5, 2, 3]	kW	Defined in section 9.1
Max. electric coil power (MP_{dhw})[a]	[3, 5, 6]	kW	Defined in section 9.1
External diameter (D_{dhw})	[450, 520, 620]	mm	Defined in section 9.1
External height (H_{dhw})	[1114, 1516, 1520]	mm	Defined in section 9.1
Thermal insulation thickness (x_f)	40	mm	Defined in section 9.1
Insulating foam heat loss factor (I_f)	16	$W/(m^3 \cdot K)$	Defined in section 9.1
Stainless steel layer thickness (x_s)	4	mm	-
Stainless steel thermal conductivity (k_{ss})	16.3	$W/(m \cdot K)$	-
Operating temp. range (T_{wmin}, T_{wmax})	[50 - 80]	$°C$	Defined in section 9.1
Inlet temperature (IT_{dhw})	Wet bulb temp.	$°C$	Defined in section 4.5.4
Thermodynamic parameters (100L, 200L, 300L)			
Internal convection coefficient (h_{Wi})	390	$W/(m^2 \cdot K)$	Defined in section 4.5.3
Prandtl number (Pr)	0.725	–	
External convection coefficient (h_{We})	[1.469, 1.359, 1.253]	$W/(m^2 \cdot K)$	
Reynolds number (Re_D)	[3214, 3714, 4428]	–	
Nusselt number ($\overline{Nu}_D$)	[26.3, 28.3, 31.0]	–	
Tank thermal transmittance (U_{dhw})	[0.445, 0.435, 0.423]	$W/(m^2 \cdot K)$	

4.5.2 Mass flow rate calculation

To estimate the mass flow rate of DHW extracted from the tank ($\dot{m}_{dhw}$) at a temperature T_{dhw}, the heat flow out of the tank ($\dot{Q}_{out}$) must be equated to the heat flow to be supplied to the household ($\dot{Q}_{wsup}$), as given in (4.30).

$$\begin{aligned} \dot{Q}^i_{out} &= \dot{Q}^i_{wsup} \\ c_w \dot{m}^i_{dhw} T^i_{dhw} &= \frac{c_w \rho_w L^i_{wsup} T_{wsup}}{1000} \\ \dot{m}^i_{dhw} &= \frac{\rho_w L^i_{wsup} T_{wsup}}{1000 T^i_{dhw}} \end{aligned} \tag{4.30}$$

Where L_{wsup} is the litres of DHW supplied to the household at a supply temperature T_{wsup}, detailed in section 5.6.

4.5.3 Tank thermal transmittance calculation

Figure 4.13 presents a schematic diagram of the DHW tank layers, consisting of inner and outer layers of stainless steel sheet, both with a thickness of x_s, separated by an insulating foam layer of thickness x_f. This composition of layers separates the external air from the internal hot water. Figure 4.14 shows an equivalent scheme of thermal resistances, where R_{1v} and R_{2v} correspond to the external and internal convection thermal resistances, respectively. R_{1d} and R_{3d} correspond to the thermal resistances due to conduction of the stainless steel sheets, and R_{2d} is the thermal resistance due to conduction of the insulating foam. On the other hand, C_w corresponds to the thermal capacitance of the internal hot water, responsible for storing thermal energy. The value of U_W is determined as given in (4.31).

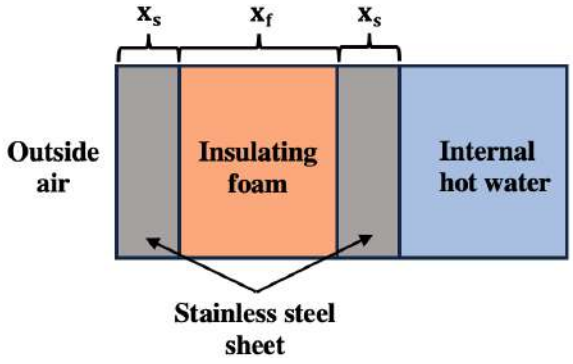

Figure 4.13: Schematic diagram of the insulation layers of the DHW tank.

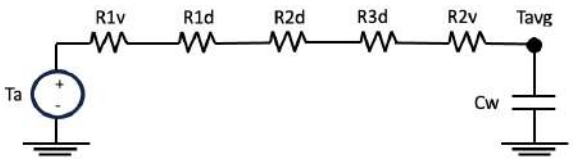

Figure 4.14: Equivalent thermal resistance scheme of the DHW tank.

$$U_w = \frac{1}{R_{1v} + R_{1d} + R_{2d} + R_{3d} + R_{2v}} = \frac{1}{\frac{1}{h_{We}} + \frac{x_s}{k_{ss}} + \frac{1}{I_f x_f} + \frac{x_s}{k_{ss}} + \frac{1}{h_{Wi}}} \tag{4.31}$$

Where k_{ss} is the stainless steel thermal conductivity, I_f is the insulating foam heat loss factor, h_{We} is the convection coefficient with the external air, and h_{Wi} is the convection coefficient with the internal hot water. Thus, h_{Wi} is determined from [50], where convection coefficients were estimated for residential DHW storage tanks in solar thermal systems, with aspect ratios up to 3. Table 4.6 presents the values used for the top, bottom, and sidewall surfaces, along with the weighted value of h_{Wi}.

Table 4.6: Internal heat convection transfer coefficient (h_{Wi}) values [50].

h_{Wi} (top)	h_{Wi} (bottom)	h_{Wi} (side)	h_{Wi} (weighted)	Units
680	80	360	390	$W/(m^2 \cdot K)$

On the other hand, h_{We} is determined using an empirical correlation for a cylinder in cross-flow [51]. For the external surface of a cylinder, it is determined based on the Nusselt number at each angle (θ) from the stagnation point ($\theta = 0$). However, for engineering applications, the empirical correlation given in (4.32) allows us to obtain an average external convection coefficient ($\overline{h}_{ext}$) around the external surface.

$$h_{We} = \overline{h}_{We} = \frac{k_a}{D_{dhw}\overline{Nu}_D} \tag{4.32}$$

Where k_a is the thermal conductivity of outside air, D_{dhw} is the external diameter of the tank, and $\overline{Nu}_D$ is the Nusselt number. The latter is determined as given in (4.33), as a function of the Reynolds number (Re_D) and the Prandtl number (Pr) (for $Pr \geq 0.7$), which are determined as given in (4.34) and (4.35), respectively.

$$\overline{Nu}_D = \begin{cases} 0.683 Re_D^{0.466} Pr^{1/3} & \text{if } 40 \leq Re_D \leq 4000 \\ 0.193 Re_D^{0.618} Pr^{1/3} & \text{if } 4000 \leq Re_D \leq 40000 \end{cases} \tag{4.33}$$

$$Re_D = \frac{W_v D_{dhw}}{\nu_a} \tag{4.34}$$

$$Pr = \frac{\mu_a c_a}{k_a} \tag{4.35}$$

Where W_v is the external air velocity, ν_a is the kinematic viscosity of air, μ_a is the dynamic viscosity of air, and c_a is the specific heat of air.

4.5.4 External conditions

To obtain the inlet temperature in the DHW tank (IT_{dhw}), it is assumed that the piping network of the supply system is long enough for the air inside to reach its saturation point, i.e., it reaches a relative humidity of 100% and the adiabatic saturation temperature or wet-bulb temperature (T_{wb}) (expressed as T_2 in Figure 4.15). With these assumptions, it can be assumed that IT_{dhw} is equivalent to the ambient wet bulb temperature T_{wb} [52].

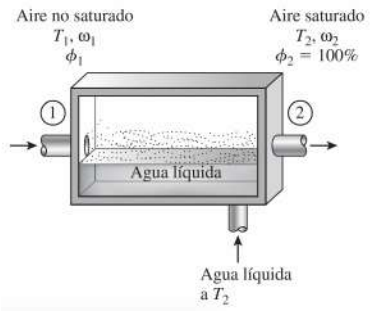

Figure 4.15: Adiabatic saturation process.

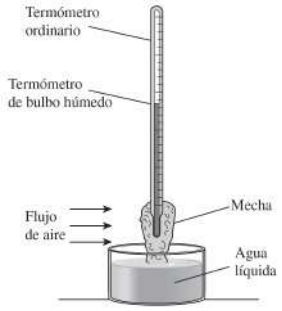

Figure 4.16: Wet-bulb thermometer.

In practice, T_{wb} is obtained using a wet-bulb thermometer (see Figure 4.16), which measures the temperature of the air saturated inside the wick moistened with liquid water, equivalent to the temperature of the liquid water. However, for our case study, there are no local data for T_{wb}, so Equation 4.36 is used, based on the relative humidity of the air (RH_a) and the dry-bulb temperature (T_a) in $°C$ [53]. Finally, typical meteorological year (TMY) data for RH_a, T_a, and T_{wb} are described in more detail in section 5.2.

$$T_{in} = T_{wb} = T_a \arctan[0.151977(RH_a + 8.313659)^{0.5}] + \arctan(T_a + RH_a) - \arctan(RH_a - 1.676331) + 0.00391838(RH_a)^{1.5} \arctan(0.023101 RH_a) - 4.686035 \quad (4.36)$$

4.5.5 Logic Algoritms

Two logical algorithms are presented to control the temperature inside the DHW tank, Algorithm 4 and Algorithm 5. Algorithm 4 presents the logical sequence corresponding to a conventional control mode based on [47]:

- The operation mode of the previous time step ($mode^{i-1}$) and the current internal temperature of the DHW tank (T^i_{dhw}) are received. If heating, it is checked if T^i_{dhw} is less than or equal to the maximum operating temperature T_{wmax}.
  - (A) If so, then it is heated at a power P^i_{dhw} equal to the rated power. (B) Otherwise, the heater is turned off.
- If it is off, it is checked if T^i_{dhw} is less than T_{wmin}.
  - If so, (A) is carried out, and otherwise it remains off.
- Finally, the new internal temperature T^{i+1}_{dhw} is computed.

On the other hand, Algorithm 5 presents the logical sequence of the proposed control model (referred to as DHW Self), which aims to increase the self-consumption of PV surpluses by prosumers and the purchase of surpluses in the P2P market at a special price (W^{PR}_{SP}) by consumers, to be used for DHW tank consumption. First, the operation mode of the previous time step ($mode^{i-1}$), the internal temperature (T^i_{dhw}), and the available surplus power (P^i_{ava}) to be used in the operation of the DHW tank are received. If P^i_{ava} is available:

- It is checked if T^i_{dhw} is less than or equal to T_{wmax}.
  - If so, it is checked if P^i_{ava} is less than the maximum permissible power for the heater MP_{dhw}.
    - If so, then the heater is turned on at a power equal to P^i_{ava}. Otherwise, the power is limited to MP_{dhw}.
- If T^i_{dhw} has exceeded T_{wmax}, then the heater is turned off.
- Finally, the new internal temperature T^{i+1}_{dhw} is computed.

If P^i_{ava} is not available, then Algorithm 4 should be continued with.

Algorithm 4 ALG DHW 01

Input: $mode^{i-1}, T^{i}_{dhw}$
Output: $mode^{i}, T^{i+1}_{dhw}$
if $mode^{i-1} = On$ **then**
  if $T^{i}_{dhw} \leq T_{wmax}$ **then**
    A: $mode^{i} = On$; $P^{i}_{dhw} = Rated$
  else
    B: $mode^{i} = Off$; $P^{i}_{dhw} = 0$
  end if
else if $T^{i}_{dhw} \leq T_{wmin}$ **then**
  A
else
  B
end if
Compute T^{i+1}_{dhw}

Algorithm 5 ALG DHW 02

Input: $mode^{i-1}, P^{i}_{ava}, T^{i}_{dhw}$
Output: $mode^{i}, T^{i+1}_{dhw}$
if $P^{i}_{ava} > 0$ **then**
  if $T^{i}_{dhw} \leq T_{wmax}$ **then**
    if $P^{i}_{ava} < MP_{dhw}$ **then**
      $mode^{i} = On$, $P^{i}_{dhw} = P^{i}_{ava}$
    else
      $mode^{i} = On$, $P^{i}_{dhw} = MP_{dhw}$
    end if
  else
    $mode^{i} = Off$, $P^{i}_{dhw} = 0$
  end if
  Compute T^{i+1}_{dhw}
else
  Continue with ALG DHW 01
end if

4.6 Air Conditioning Model

The equivalent thermal model of resistances and capacitances for a residential construction was adapted from [54], [55], and [48], corresponding to a one-dimensional transient heat conduction model with five nodes: outside air (n_a), walls (n_W), roof (n_R), windows (n_{ws}), and indoor air (n_H). Figure 4.17 shows a schematic diagram of the equivalent thermal model.

Each node is associated with a defined control volume. The node (n_a) corresponds to an infinite reservoir, so the energy balance analysis in this node is trivial. On the other hand, the floor of the house is assumed to be an adiabatic surface, so it is not considered in the thermal model. The mass balance for control volume is determined as given in (4.37). However, control volumes do not exhibit mass flow exchanges

at their boundaries, except for node n_H, which maintains a mass balance between the mass flows due to infiltrations to/from the outside air.

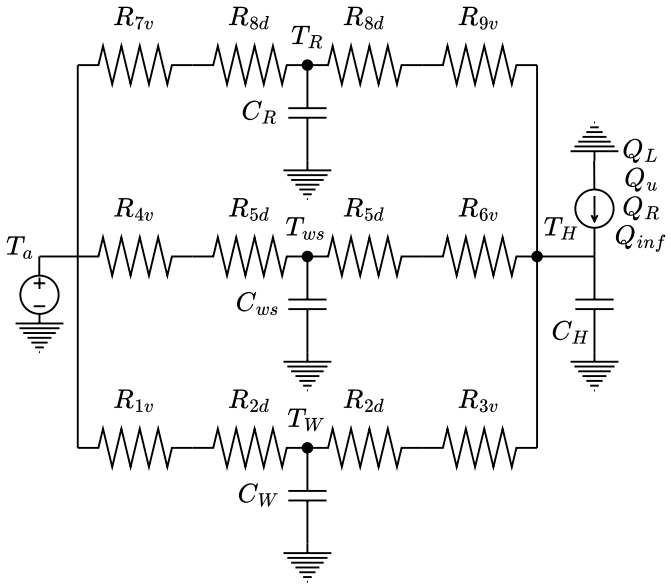

Figure 4.17: Schematic diagram of thermal resistances [55].

$$\frac{dm_{CV}}{dt} = \dot{m}_{in} - \dot{m}_{out} = 0 \tag{4.37}$$

On the other hand, the energy balance for a control volume is determined as given in (4.38).

$$\frac{dE_{CV}}{dt} = \rho V c \frac{dT}{dt} = \sum \dot{Q} + \dot{G} \tag{4.38}$$

Where $\sum \dot{Q}$ corresponds to the heat transfer through the surfaces, $\dot{G}$ corresponds to the internal heat generation, $\frac{dT}{dt}$ to the change in internal temperature over time, while ρ, V, and c correspond to the density, internal volume, and specific heat, respectively. The heat transfer by convection-radiation between nodes A and B is determined as given in (4.39).

$$\dot{Q}_{\text{conv-rad}} = h_s A \Delta T \tag{4.39}$$

Where h_s is the surface radiative-convective coefficient, A is the area perpendicular to the heat flow direction, and ΔT is the temperature difference between the nodes. On the other hand, the heat transfer by conduction between two nodes is determined as given in (4.40).

$$\dot{Q}_{\text{cond}} = A \Delta T \frac{1}{2} \sum_{j=1}^{n} \frac{k_j}{e_j} \tag{4.40}$$

Where k_j and e_j correspond to the thermal conductivity and thickness of each material layer j in

the construction solution, respectively. On the other hand, the heat capacity of the construction solution is determined as given in (4.41).

$$C = \sum_{j=1}^{n} \rho_j V_j c_j \tag{4.41}$$

Where ρ_j, V_j, and c_j correspond to the density, volume, and specific heat of each material layer j in the construction solution, respectively.

4.6.1 Energy balance at node R

The energy balance at node R is determined as given in (4.42).

$$\frac{dT_R}{dt} \sum_{j=1}^{n} \rho_j V_j c_j = \dot{Q}_{\text{conv-rad(a/R)}} + \dot{Q}_{\text{cond(a/R)}} + \dot{Q}_{\text{cond(H/R)}} + \dot{Q}_{\text{conv-rad(H/R)}} \tag{4.42}$$

Where $\dot{Q}_{\text{conv-rad(a/R)}}$ and $\dot{Q}_{\text{cond(a/R)}}$ are the heat transfer rates by convection-radiation and conduction to/from the exterior, respectively, while $\dot{Q}_{\text{conv-rad(H/R)}}$ and $\dot{Q}_{\text{cond(H/R)}}$ are those with the interior. By discretizing implicitly in time, we arrive at equation (4.43).

$$\begin{aligned} C_R \frac{T_R^{i+1} - T_R^i}{\Delta t} = {} & h_{seR} A_R (T_a^{i+1} - T_R^{i+1}) + A_R (T_a^{i+1} - T_R^{i+1}) \frac{1}{2} \sum_{j=1}^{n} \frac{k_j}{e_j} \\ & + A_R (T_H^{i+1} - T_R^{i+1}) \frac{1}{2} \sum_{j=1}^{n} \frac{k_j}{e_j} + h_{siR} A_R (T_H^{i+1} - T_R^{i+1}) \end{aligned} \tag{4.43}$$

Finally, equation (4.43) can be rewritten in terms of thermal resistances as given in (4.44).

$$\begin{aligned} C_R \frac{T_R^{i+1} - T_R^i}{\Delta t} &= \frac{1}{R_{7v}} (T_a^{i+1} - T_R^{i+1}) + \frac{1}{R_{8d}} (T_a^{i+1} - T_R^{i+1}) + \frac{1}{R_{8d}} (T_H^{i+1} - T_R^{i+1}) + \frac{1}{R_{9v}} (T_H^{i+1} - T_R^{i+1}) \\ -\frac{C_R}{\Delta t} T_R^i &= \left(\frac{1}{R_{7v}} + \frac{1}{R_{8d}} \right) T_a^{i+1} + \left(-\frac{1}{R_{7v}} - \frac{2}{R_{8d}} - \frac{1}{R_{9v}} - \frac{C_R}{\Delta t} \right) T_R^{i+1} + \left(\frac{1}{R_{8d}} + \frac{1}{R_{9v}} \right) T_H^{i+1} \end{aligned} \tag{4.44}$$

4.6.2 Energy balance at node ws

Similarly to node R, the energy balance at node ws is determined as given in (4.45).

$$\frac{dT_{ws}}{dt} \sum_{j=1}^{n} \rho_j V_j c_j = \dot{Q}_{\text{conv-rad(a/ws)}} + \dot{Q}_{\text{cond(a/ws)}} + \dot{Q}_{\text{cond(H/ws)}} + \dot{Q}_{\text{conv-rad(H/ws)}} \tag{4.45}$$

By discretizing implicitly in time, we arrive at equation (4.46).

$$C_{ws}\frac{T_{ws}^{i+1}-T_{ws}^{i}}{\Delta t} = h_{sews}A_{ws}(T_a^{i+1}-T_{ws}^{i+1}) + A_{ws}(T_a^{i+1}-T_{ws}^{i+1})\frac{1}{2}\sum_{j=1}^{n}\frac{k_j}{e_j} + A_{ws}(T_H^{i+1}-T_{ws}^{i+1})\frac{1}{2}\sum_{j=1}^{n}\frac{k_j}{e_j} + h_{siws}A_{ws}(T_H^{i+1}-T_{ws}^{i+1}) \tag{4.46}$$

Rewriting in terms of thermal resistances, we arrive at equation (4.47).

$$\begin{aligned} C_{ws}\frac{T_{ws}^{i+1}-T_{ws}^{i}}{\Delta t} &= \frac{1}{R_{4v}}(T_a^{i+1}-T_{ws}^{i+1}) + \frac{1}{R_{5d}}(T_a^{i+1}-T_{ws}^{i+1}) + \frac{1}{R_{5d}}(T_H^{i+1}-T_{ws}^{i+1}) + \frac{1}{R_{6v}}(T_H^{i+1}-T_{ws}^{i+1}) \\ -\frac{C_{ws}}{\Delta t}T_{ws}^{i} &= \left(\frac{1}{R_{4v}}+\frac{1}{R_{5d}}\right)T_a^{i+1} + \left(-\frac{1}{R_{4v}}-\frac{2}{R_{5d}}-\frac{1}{R_{6v}}-\frac{C_{ws}}{\Delta t}\right)T_{ws}^{i+1} + \left(\frac{1}{R_{5d}}+\frac{1}{R_{6v}}\right)T_H^{i+1} \end{aligned} \tag{4.47}$$

4.6.3 Energy balance at node W

Similarly to the previous nodes, the energy balance at node W is determined as given in (4.48).

$$\frac{dT_W}{dt}\sum_{j=1}^{n}\rho_j V_j c_j = \dot{Q}_{\text{conv-rad(a/W)}} + \dot{Q}_{\text{cond(a/W)}} + \dot{Q}_{\text{cond(H/W)}} + \dot{Q}_{\text{conv-rad(H/W)}} \tag{4.48}$$

By discretizing implicitly in time, we arrive at equation (4.49).

$$C_W\frac{T_W^{i+1}-T_W^{i}}{\Delta t} = h_{seW}A_W(T_a^{i+1}-T_W^{i+1}) + A_W(T_a^{i+1}-T_W^{i+1})\frac{1}{2}\sum_{j=1}^{n}\frac{k_j}{e_j} + A_W(T_H^{i+1}-T_W^{i+1})\frac{1}{2}\sum_{j=1}^{n}\frac{k_j}{e_j} + h_{siW}A_W(T_H^{i+1}-T_W^{i+1}) \tag{4.49}$$

Rewriting in terms of thermal resistances, we arrive at equation (4.50).

$$\begin{aligned} C_W\frac{T_W^{i+1}-T_W^{i}}{\Delta t} &= \frac{1}{R_{1v}}(T_a^{i+1}-T_W^{i+1}) + \frac{1}{R_{2d}}(T_a^{i+1}-T_W^{i+1}) + \frac{1}{R_{2d}}(T_H^{i+1}-T_W^{i+1}) + \frac{1}{R_{3v}}(T_H^{i+1}-T_W^{i+1}) \\ -\frac{C_W}{\Delta t}T_W^{i} &= \left(\frac{1}{R_{1v}}+\frac{1}{R_{2d}}\right)T_a^{i+1} + \left(-\frac{1}{R_{1v}}-\frac{2}{R_{2d}}-\frac{1}{R_{3v}}-\frac{C_W}{\Delta t}\right)T_W^{i+1} + \left(\frac{1}{R_{2d}}+\frac{1}{R_{3v}}\right)T_H^{i+1} \end{aligned} \tag{4.50}$$

4.6.4 Energy balance at node H

The energy balance at node H is determined as given in (4.51).

$$\frac{dT_H}{dt}\rho_H V_H c_H = \dot{Q}_{\text{conv-rad(H/R)}} + \dot{Q}_{\text{cond(H/R)}} + \dot{Q}_{\text{conv-rad(H/ws)}} + \dot{Q}_{\text{cond(H/ws)}} + \dot{Q}_{\text{conv-rad(H/W)}} + \dot{Q}_{\text{cond(H/W)}} + \dot{Q}_{\text{u}} + \dot{Q}_{\text{L}} + \dot{Q}_{\text{R}} + \dot{Q}_{\text{inf}} \tag{4.51}$$

Where $\dot{Q}_{\text{u}}$ is the heat input from the AC system, $\dot{Q}_{\text{L}}$ is the heat input from appliances, lighting, and heat generated by occupants of the home, $\dot{Q}_{\text{R}}$ is the heat input from solar radiation that filters through the window area, and $\dot{Q}_{\text{inf}}$ is the heat input due to outside air infiltration. Rewriting equation (4.51) in terms of thermal resistances, we obtain equation (4.52).

$$\begin{aligned} C_H\frac{T_H^{i+1}-T_H^i}{\Delta t} &= \frac{1}{R_{9v}}(T_R^{i+1}-T_H^{i+1}) + \frac{1}{R_{8d}}(T_R^{i+1}-T_H^{i+1}) + \frac{1}{R_{6v}}(T_{ws}^{i+1}-T_H^{i+1}) + \frac{1}{R_{5d}}(T_{ws}^{i+1}-T_H^{i+1}) \\ &\quad + \frac{1}{R_{3v}}(T_W^{i+1}-T_H^{i+1}) + \frac{1}{R_{2d}}(T_W^{i+1}-T_H^{i+1}) + Q_L^{i+1} + Q_R^{i+1} + Q_u^{i+1} + Q_{inf}^{i+1} \\ -C_H\frac{T_H^i}{\Delta t} &= \left(\frac{1}{R_{9v}}+\frac{1}{R_{8d}}\right)T_R^{i+1} + \left(\frac{1}{R_{6v}}+\frac{1}{R_{5d}}\right)T_{ws}^{i+1} + \left(\frac{1}{R_{3v}}+\frac{1}{R_{2d}}\right)T_W^{i+1} \\ &\quad + \left(-\frac{1}{R_{9v}}-\frac{1}{R_{8d}}-\frac{1}{R_{6v}}-\frac{1}{R_{5d}}-\frac{1}{R_{3v}}-\frac{1}{R_{2d}}-\frac{C_H}{\Delta t}\right)T_H^{i+1} + Q_L^{i+1} + Q_R^{i+1} + Q_u^{i+1} + Q_{inf}^{i+1} \end{aligned} \tag{4.52}$$

4.6.5 System of equations

Finally, we arrive at the following system of equations to solve:

$$\begin{aligned} -\frac{C_R}{\Delta t}T_R^i &= \left(\frac{1}{R_{7v}}+\frac{1}{R_{8d}}\right)T_a^{i+1} + \left(-\frac{1}{R_{7v}}-\frac{2}{R_{8d}}-\frac{1}{R_{9v}}-\frac{C_R}{\Delta t}\right)T_R^{i+1} + \left(\frac{1}{R_{8d}}+\frac{1}{R_{9v}}\right)T_H^{i+1} \\ -\frac{C_{ws}}{\Delta t}T_{ws}^i &= \left(\frac{1}{R_{4v}}+\frac{1}{R_{5d}}\right)T_a^{i+1} + \left(-\frac{1}{R_{4v}}-\frac{2}{R_{5d}}-\frac{1}{R_{6v}}-\frac{C_{ws}}{\Delta t}\right)T_{ws}^{i+1} + \left(\frac{1}{R_{5d}}+\frac{1}{R_{6v}}\right)T_H^{i+1} \\ -\frac{C_W}{\Delta t}T_W^i &= \left(\frac{1}{R_{1v}}+\frac{1}{R_{2d}}\right)T_a^{i+1} + \left(-\frac{1}{R_{1v}}-\frac{2}{R_{2d}}-\frac{1}{R_{3v}}-\frac{C_W}{\Delta t}\right)T_W^{i+1} + \left(\frac{1}{R_{2d}}+\frac{1}{R_{3v}}\right)T_H^{i+1} \\ -C_H\frac{T_H^i}{\Delta t} &= \left(\frac{1}{R_{9v}}+\frac{1}{R_{8d}}\right)T_R^{i+1} + \left(\frac{1}{R_{6v}}+\frac{1}{R_{5d}}\right)T_{ws}^{i+1} + \left(\frac{1}{R_{3v}}+\frac{1}{R_{2d}}\right)T_W^{i+1} \\ &\quad + \left(-\frac{1}{R_{9v}}-\frac{1}{R_{8d}}-\frac{1}{R_{6v}}-\frac{1}{R_{5d}}-\frac{1}{R_{3v}}-\frac{1}{R_{2d}}-\frac{C_H}{\Delta t}\right)T_H^{i+1} + Q_L^{i+1} + Q_R^{i+1} + Q_u^{i+1} + Q_{inf}^{i+1} \end{aligned}$$

To simplify the expressions, the thermal resistances are regrouped as:

$$R_1 = \frac{1}{R_{1v}}+\frac{1}{R_{2d}} \qquad R_2 = \frac{1}{R_{3v}}+\frac{1}{R_{2d}} \qquad R_3 = \frac{1}{R_{4v}}+\frac{1}{R_{5d}}$$
$$R_4 = \frac{1}{R_{6v}}+\frac{1}{R_{5d}} \qquad R_5 = \frac{1}{R_{7v}}+\frac{1}{R_{8d}} \qquad R_6 = \frac{1}{R_{9v}}+\frac{1}{R_{8d}}$$

This way, the system of equations becomes:

$$
\begin{aligned}
-\frac{C_R}{\Delta t}T_R^i &= R_5 T_a^{i+1} + (-R_5 - R_6 - \frac{C_R}{\Delta t})T_R^{i+1} + R_6 T_H^{i+1} \\
-\frac{C_{ws}}{\Delta t}T_{ws}^i &= R_3 T_a^{i+1} + (-R_3 - R_4 - \frac{C_{ws}}{\Delta t})T_{ws}^{i+1} + R_4 T_H^{i+1} \\
-\frac{C_W}{\Delta t}T_W^i &= R_1 T_a^{i+1} + (-R_1 - R_2 - \frac{C_W}{\Delta t})T_W^{i+1} + R_2 T_H^{i+1} \\
-C_H\frac{T_H^i}{\Delta t} &= R_6 T_R^{i+1} + R_4 T_{ws}^{i+1} + R_2 T_W^{i+1} + (-R_6 - R_4 - R_2 - \frac{C_H}{\Delta t})T_H^{i+1} + Q_L^{i+1} + Q_R^{i+1} + Q_u^{i+1} + Q_{inf}^{i+1}
\end{aligned}
$$

Then, expressing it in matrix form, we have:

$$
\begin{bmatrix}
-R_5 - R_6 - \frac{C_R}{\Delta t} & 0 & 0 & R_6 \\
0 & -R_1 - R_2 - \frac{C_W}{\Delta t} & 0 & R_2 \\
0 & 0 & -R_3 - R_4 - \frac{C_{ws}}{\Delta t} & R_4 \\
R_6 & R_2 & R_4 & -R_6 - R_4 - R_2 - \frac{C_H}{\Delta t}
\end{bmatrix}
\begin{bmatrix} T_R^{i+1} \\ T_W^{i+1} \\ T_{ws}^{i+1} \\ T_H^{i+1} \end{bmatrix}
$$

$$
+ \begin{bmatrix} R_5 T_a^{i+1} \\ R_1 T_a^{i+1} \\ R_3 T_a^{i+1} \\ Q_L^{i+1} + Q_R^{i+1} + Q_u^{i+1} + Q_{inf}^{i+1} \end{bmatrix} = -\frac{1}{\Delta t}\begin{bmatrix} C_R T_R^i \\ C_W T_W^i \\ C_{ws} T_{ws}^i \\ C_H T_H^i \end{bmatrix}
$$

Then, solving for the values of the temperatures at the nodes for $t = i + 1$:

$$
\begin{bmatrix} T_R^{i+1} \\ T_W^{i+1} \\ T_{ws}^{i+1} \\ T_H^{i+1} \end{bmatrix} =
\begin{bmatrix}
-R_5 - R_6 - \frac{C_R}{\Delta t} & 0 & 0 & R_6 \\
0 & -R_1 - R_2 - \frac{C_W}{\Delta t} & 0 & R_2 \\
0 & 0 & -R_3 - R_4 - \frac{C_{ws}}{\Delta t} & R_4 \\
R_6 & R_2 & R_4 & -R_6 - R_4 - R_2 - \frac{C_H}{\Delta t}
\end{bmatrix}^{-1}
$$

$$
\begin{bmatrix}
-\frac{C_R T_R^i}{\Delta t} - R_5 T_a^{i+1} \\
-\frac{C_W T_W^i}{\Delta t} - R_1 T_a^{i+1} \\
-\frac{C_{ws} T_{ws}^i}{\Delta t} - R_3 T_a^{i+1} \\
-\frac{C_H T_H^i}{\Delta t} - Q_L^{i+1} - Q_R^{i+1} - Q_u^{i+1} - Q_{inf}^{i+1}
\end{bmatrix}
$$

Where the system of equations must be solved at each time step to obtain the temperatures of the layers of the construction solution and the interior air.

4.6.6 Determining thermal resistances and heat capacities

A generic $120m^2$ house was selected for the case study (see Figures 4.18 and 4.19). The selection of construction materials for typical homes in Chile was obtained from recommendations and standards described in [56] and [57]. Figures 4.20, 4.21, and 4.22 show detailed views of the composition of the wall, roof, and

double-glazed windows, respectively. Table 4.7 details the parameters of the materials in the construction solution for the house. Table 4.8 shows the ranges of values of the thermal resistances obtained.

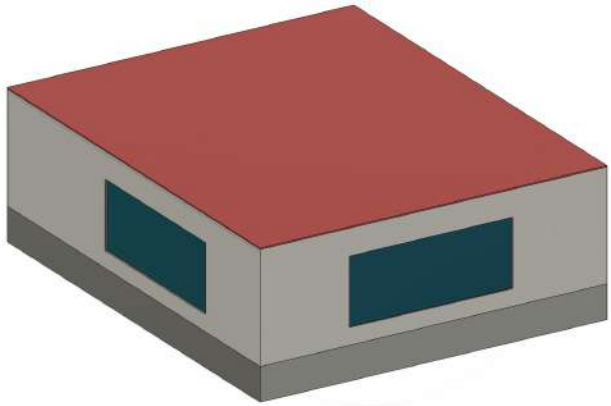

Figure 4.18: Isometric view of the home.

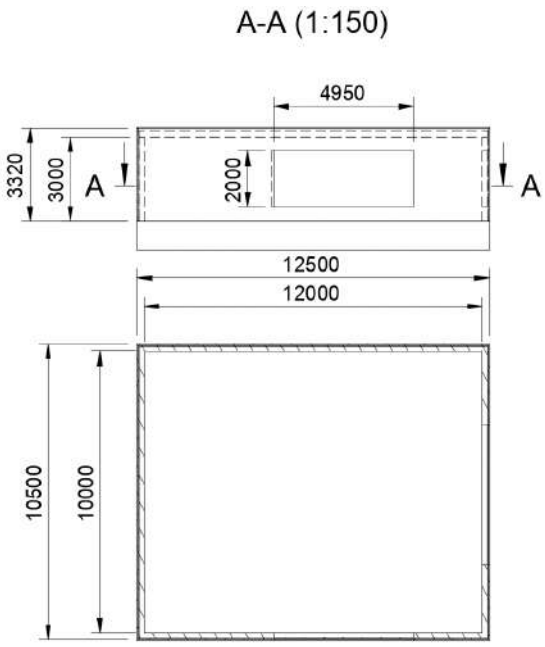

Figure 4.19: Top view of the home and section A-A.

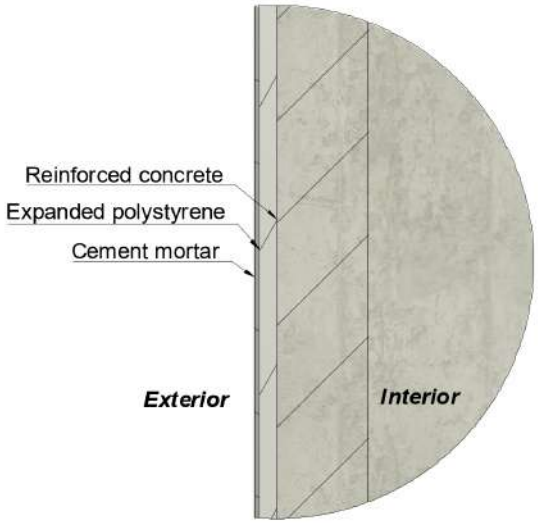

Figure 4.20: Detail view of wall construction materials.

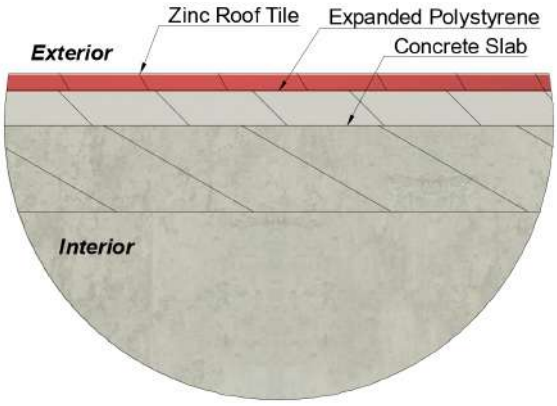

Figure 4.21: Detail view of roof construction materials.

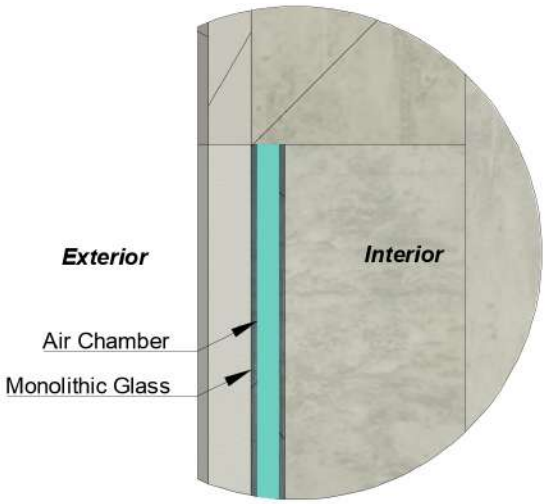

Figure 4.22: Detail view of double-glazed window construction materials.

Table 4.8: Thermal resistances obtained.

Thermal resistance	Value	Units
R_{1v}	$[2.130 \cdot 10^{-4}, 1.092 \cdot 10^{-3}]$	K/W
R_{2d}	$5.973 \cdot 10^{-3}$	
R_{3v}	$[1.042 \cdot 10^{-3}, 1.338 \cdot 10^{-3}]$	
R_{4v}	$6.566 \cdot 10^{-3}$	
R_{5d}	$4.672 \cdot 10^{-3}$	
R_{6v}	$2.020 \cdot 10^{-3}$	
R_{7v}	$[1.992 \cdot 10^{-4}, 1.021 \cdot 10^{-3}]$	
R_{8d}	$8.583 \cdot 10^{-3}$	
R_{9v}	$[7.537 \cdot 10^{-4}, 1.529 \cdot 10^{-3}]$	

Table 4.7: Building construction materials.

Component	Material	Parameter		Value	Unit
Windows	General	Area	A_{ws}	19.8	m^2
		Materials emissivity	ϵ_{ws}	0.82	–
		Heat capacity	C_{ws}	497	kJ/K
	Monolithic Glass	Thickness	e_{ws1}	2 x 0.006	m
		Volume	V_{ws1}	2 x 0.1188	m^3
		Thermal conductivity	k_{ws1}	1.2	$W/(m \cdot K)$
		Density	ρ_{ws1}	2500	kg/m^3
		Specific heat	c_{ws1}	837	$J/(kg \cdot K)$
	Air Chamber	Thickness	e_{ws2}	0.02	m
		Volume	V_{ws2}	0.396	m^3
		Density	ρ_a	1.225	kg/m^3
Wall	General	Area	A_W	112.2	m^2
		Materials emissivity	ϵ_W	0.9	–
		Heat capacity	C_W	48619	kJ/K
	Reinforced concrete	Thickness	e_{W1}	0.2	m
		Volume	V_{W1}	22.92	m^3
		Thermal conductivity	k_{W1}	1.63	$W/(m \cdot K)$
		Density	ρ_{W1}	2400	kg/m^3
		Specific heat	c_{W1}	840	$J/(kg \cdot K)$
	Expanded polystyrene	Thickness	e_{W2}	0.05	m
		Volume	V_{W2}	3.52	m^3
		Thermal conductivity	k_{W2}	0.0413	$W/(m \cdot K)$
		Density	ρ_{W2}	15	kg/m^3
		Specific heat	c_{W2}	1200	$J/(kg \cdot K)$
	Cement Mortar	Thickness	e_{W3}	0.01	m
		Volume	V_{W3}	1.18	m^3
		Thermal conductivity	k_{W3}	1.4	$W/(m \cdot K)$
		Density	ρ_{W3}	2000	kg/m^3
		Specific heat	c_{W3}	920	$J/(kg \cdot K)$
Roof	General	Area	A_R	120	m^2
		Materials emissivity	ϵ_R	0.9	–
		Heat capacity	C_R	65120	kJ/K
	Reinforced concrete slab	Thickness	e_{R1}	0.2	m
		Volume	V_{R1}	26.16	m^3
	Expanded polystyrene	Thickness	e_{R2}	0.08	m
		Volume	V_{R2}	10.46	m^3
	Zinc Roof Tile	Thickness	e_{R3}	0.03	m
		Volume	V_{R3}	1.18	m^3
		Thermal conductivity	k_{R3}	112	$W/(m \cdot K)$
		Density	ρ_{R3}	7000	kg/m^3
		Specific heat	c_{R3}	380	$J/(kg \cdot K)$
Internal Air	Air	Volume	V_H	360	m^3
		Heat capacity	C_H	443	kJ/K

Note: The parameters ρ_{R1}, ρ_{R2}, c_{R1}, c_{R2}, k_{R1}, k_{R2}, ρ_H, and c_H have been omitted as the selected material is repeated in different construction solutions.

4.6.7 Thermal requirements and regulations

Chile is divided into 9 thermal zones, and because each zone has different weather conditions, different degrees of thermal insulation regulations are applied for residential buildings, leading to varying heating/cooling demands. The case study established in Viña del Mar is within thermal zone C. Therefore, the home must comply with the requirements indicated in the Chilean Official Standard Nch 853:2021 and in Art. 4.1.10 of the Thermal Regulation of the General Urban Planning and Construction Ordinance. Table 4.9 presents the compliance with criteria in the home design to meet thermal standards and regulations, in relation to thermal transmittance values and the thermal mass index.

Table 4.9: Construction criteria for thermal zone C.

Criterion	Description	Used Value	Normative	Unit
A	Recommended maximum roof U-value	[0.43 - 0.46]	0.47	$W/(m^2 \cdot K)$
B	Recommended maximum wall U-value	[0.62 - 0.67]	0.80	$W/(m^2 \cdot K)$
C	Recommended maximum windows U-value	2.82	3.60	$W/(m^2 \cdot K)$
D	Recommended minimum Thermal Mass Index	201.6 / Heavy	70 / Light	$kJ/(m^2 \cdot K)$; Category

Below, each criterion is explained in detail:

- Criterion A - Maximum U-value of the roof: The value of U_R was calculated according to the methodology presented in section 4.6.7.1, determined as given in (4.53).

$$U_R = \frac{1}{R_{7v} + 2R_{8d} + R_{9v}} \tag{4.53}$$

  Where R_{7v} is the external surface thermal resistance, R_{8d} is the thermal resistance due to conduction, and R_{9v} is the internal surface thermal resistance. The value varies mainly because the external convective heat transfer coefficient h_{ce} varies with the wind speed V_{wind}, and the internal convective heat transfer coefficient h_{ci} varies with the internal temperature T_H and the temperature of the roof materials T_R. When T_H is higher than T_R, the internal surface resistance R_{si} decreases mainly because the internal air has a higher temperature, and thus, decreasing its density, it tends to rise towards the roof surface, favoring heat transfer as it is in the same direction as the heat flow, which is upward. Conversely, when T_R is higher than T_H, the heat flow direction is downward; however, the warmer air inside the house tends to stay near the internal surface of the roof, hindering heat transfer and increasing R_{si}.

- Criterion B - Maximum U-value of the wall: Similar to criterion A, the value of U_W was calculated according to the methodology presented in section 4.6.7.1, determined as given in (4.53).

$$U_W = \frac{1}{R_{1v} + 2R_{2d} + R_{3v}} \tag{4.54}$$

  Where R_{1v} is the external surface thermal resistance, R_{2d} is the thermal resistance due to conduction, and R_{3v} is the internal surface thermal resistance. In this case, variability arises mainly due to h_{ce} and the internal and external radiative coefficients.

- Criterion C - Maximum U-value of the window: Similar to the previous criteria, the value of U_{ws} was calculated according to the methodology presented in section 4.6.7.1, determined as given in (4.55).

$$U_{ws} = \frac{1}{R_{4v} + 2R_{5d} + R_{3v}} \tag{4.55}$$

  The value of U_{ws} does not vary because fixed design values were used, as they provided more consistent results in the numerical model. On the other hand, R_{5d} is as given in (4.56).

$$R_{5d} = \frac{R_{cond} + R_g}{2} \tag{4.56}$$

- Criterion D - Thermal Mass Indicator: The heat capacity per unit area of the building's construction solution was calculated according to the methodology presented in section 4.6.7.2. Based on [57], a heavy construction solution was selected to take advantage of thermal inertia in smart AC load management models.

4.6.7.1 U-value calculation

The calculation method for thermal transmittance (U) was obtained from [58]. According to the regulations in Table 4.10, for each thermal zone, the set of layers of materials for both the roof, the wall, and the windows must comply with a thermal transmittance value lower than the specified ones, respectively. Thus, U is determined as given in (4.57) for the roof and the wall.

Table 4.10: Values of thermal transmittance U [59].

Thermal Zone	A	B	C	D	E	F	G	H	I	Unit
Roofs	0.84	0.47	0.47	0.38	0.33	0.28	0.28	0.25	0.25	$W/(m^2 \cdot K)$
Walls	2.10	0.80	0.80	0.80	0.60	0.45	0.40	0.30	0.35	
Windows	5.8	3.6	3.6	3.6	3.0	3.0	2.4	2.4	2.4	

$$U = \frac{1}{R_{se} + R_{cond} + R_{si}} \tag{4.57}$$

Where R_{se} and R_{si} are the external and internal surface thermal resistances, respectively, and R_{cond} is the thermal resistance due to conduction. The thermal resistances due to conduction are determined as given in (4.58).

$$R_{cond} = \frac{1}{\sum_{i=1}^{n} t_i/k_i} \tag{4.58}$$

Where t_i and k_i are the thicknesses and thermal conductivities of construction material i. On the other hand, the surface thermal resistances R_s are determined from convective and radiative effects as given in (4.59).

$$R_s = \frac{1}{h_c + h_r} \tag{4.59}$$

Where h_c is the convective coefficient and h_r is the radiative coefficient. The determination of h_c will depend on whether we are calculating interior or exterior surfaces. For interior surfaces, the interior convective surface coefficient h_{ci} is calculated from Table 4.11, assuming a horizontal flow direction for the walls, while for the roof, the direction of the heat flow will depend on the internal temperature of the house and the average temperature of the roof materials, as given in (4.60).

Table 4.11: Values of the convective surface coefficient [58].

Surperficial convective coefficient	Heat flow direction			Units
	Upward	Horizontal	Downward	
h_{ci}	5.0	2.5	0.7	$W/(m^2 \cdot K)$

$$h_{ci} = \begin{cases} 5.0 & \text{if } T_R < T_H \\ 0.7 & \text{if } T_R \geq T_H \end{cases} \tag{4.60}$$

On the other hand, for exterior surfaces, the external convective surface coefficient h_{ce} is obtained, which will depend on the wind speed adjacent to the surface (W_v) in m/s, as given in (4.61).

$$h_{ce} = 4 + 4 \cdot W_v \tag{4.61}$$

Similarly, h_r is determined as given in (4.62), where ϵ is the hemispherical emissivity of the surface, which is usually assumed to be 0.9 for most construction materials, both on interior and exterior surfaces, σ is the Stefan-Boltzmann constant equivalent to $5.67 \times 10^{-8}\ W/(m^2 \cdot K^4)$, and T_{mn} is the mean thermodynamic temperature of the surface in K, which conventionally is assumed to be equal to the internal or external ambient temperature, depending on the calculation.

$$h_r = \epsilon 4 \sigma T_{mn}^3 \tag{4.62}$$

On the other hand, in the case of windows, the value of U is determined as given in (4.63) [56].

$$U = \frac{1}{R_{se} + R_{cond} + R_g + R_{si}} \tag{4.63}$$

Where R_{cond} corresponds to the conduction thermal resistance in the glass layers and R_g corresponds to the thermal resistance of unventilated air gaps with thicknesses less than $0.3m$, which is determined from the design values presented in Table 4.12, according to the emissivity of the materials and air gap thickness. Also, R_{se} and R_{si} are determined from conventional design values in Table 4.13.

Table 4.12: Thermal resistance in $(m^2K)/W$ of vertical unventilated air gaps with horizontal thermal flow [58] [60].

Air gap thickness *mm* / Emissivity	0.82	0.2
0	0	0
10	0.150	0.280
20	0.175	0.37

Table 4.13: Conventional surface thermal resistances [58].

Surface resistances	Heat flow direction			Units
	Upward	Horizontal	Downward	
R_{si}	0.10	0.13	0.17	$(m^2 \cdot K)/W$
R_{se}	0.04	0.04	0.04	

4.6.7.2 Thermal Mass Index

The Thermal Mass Index (I_{tm}) is obtained from the methodology presented in [57]. It is a function of the heat capacity per unit area (H_s) of the building elements. To calculate it, the sum of all layers of the element must be considered, starting from the surface in contact with the indoor air and ending under any of the following conditions:

- If the total thickness of the layers exceeds 100 mm.
- If the midpoint of the construction is reached.
- If an insulation layer is reached.

Thus, H_s is determined as given in (4.64).

$$H_s = \sum_{i=1}^{n} \rho_i c_i e_i \tag{4.64}$$

Where ρ_i, c_i, and e_i are the density, specific heat, and thickness of the material of layer i of the building element, respectively. Table 4.14 correlates I_{tm} with the value of H_s obtained. It can be observed that the requirement varies according to the thermal zone.

Table 4.14: Description of the minimum recommended thermal mass index according to the thermal zone [59].

Thermal Zone	I_{tm}	Heat Capacity	Units
A,C,E,F,G,I	Light (L)	< 70	$kJ/(m^2 \cdot K)$
B,D	Medium (M)	70 - 200	
H	Heavy (H)	>200	

4.6.8 Q_L calculation

The heat input $\dot{Q}_{\mathrm{L}}$ corresponds to the heat emitted by household appliances, lighting, and occupants. The heat generated by household appliances and lighting is equivalent to the household's electrical consumption

profile (E_c) (defined in section 5.4), assuming that all devices are located inside the home, and that heat does not escape through windows or walls (e.g. light from the lighting does not escape through the windows) [52].

On the other hand, the heat contributed by the occupants (Q_{occ}) depends directly on the occupancy profiles (defined in section 5.4), determined as an approximation based on the metabolic rate and characteristics of the occupants [61], determined as given in (4.65).

$$Q_{occ} = met \cdot B_s \cdot M \tag{4.65}$$

Where *met* is the metabolism unit, B_s is the body surface area, and M is the metabolic rate. Table 4.15 summarizes the assumed parameters.

Table 4.15: Occupancy heat gain parameters [61].

Parameter	Value	Unit
Metabolism unit (*met*)	58.15	W/m^2
Adult body surface area (B_s)	1.8	m^2
Adult metabolic rate in a detached house (M)	1	met
Heat gain per adult occupant (Q_{occ})	125.6	W

Finally, the heat contribution Q_L is defined by eq. 4.66.

$$Q_L = E_c + Q_{occ} \tag{4.66}$$

4.6.9 Q_{inf} calculation

Q_{inf} represents the heat contribution from outdoor air infiltrations into the interior, determined as given in (4.67).

$$Q_{\text{inf}} = \frac{ACH}{3600} c_a \rho_a (T_H - T_a) \tag{4.67}$$

where ACH represents air changes per hour, assumed constant at 0.5 [62], c_a is the specific heat of air, and ρ_a is the air density.

4.6.10 Q_R calculation

To obtain the heat contribution from solar radiation filtered through the windows (Q_R), the methodology presented in [62] was followed. Q_R is determined as given in (4.68).

$$Q_R = \alpha_R G_t A_{ws} \tag{4.68}$$

Where α_R is assumed as 0.2, which corresponds to the fraction of solar radiation that filters through the windows into the interior, considering the effect of the transmittance of windows and the blocking action

of shading devices, G_t corresponds to the incident solar global radiation on the window surfaces (defined in section 5.2), and A_{ws} is the effective area of the windows.

4.6.11 Q_u calculation

Q_u corresponds to the heat input from the AC system, estimated based on parameters from commercially available devices [63]. Table 4.16 summarizes the technical parameters of the AC systems considered, classified according to their size. The values of EER and COP were interpolated from Tables 4.17 and 4.18, respectively, based on the indoor temperature and outdoor temperature.

Q_u^{i+1} is determined based on the smart control strategy of the AC system. The algorithms ALG AC 01, ALG AC 02, ALG AC 03, and ALG AC 04 represent the operation modes for fixed-speed AC system, fixed-speed AC system with self-consumption priority, inverter AC system, and inverter AC system with self-consumption priority, respectively.

Table 4.17: Air conditioning EERs.

IT °C	Size															
	Small				Medium				Large				Extra large			
	OT °C															
	-15	21	35	46	-15	21	35	46	-15	21	35	46	-15	21	35	46
20	4.97	5.67	3.56	1.93	4.22	3.82	3.22	2.04	3.95	4.37	3.01	2.09	4.12	3.82	3.21	1.98
22	4.94	5.69	3.54	1.92	4.22	3.83	3.20	2.05	3.96	4.36	3.01	2.10	4.11	3.81	3.21	1.98
25	4.97	5.63	3.56	1.93	4.23	3.80	3.22	2.03	3.97	4.35	3.01	2.09	4.11	3.82	3.20	1.99
27	4.94	5.65	3.56	1.93	4.23	3.82	3.21	2.03	3.97	4.35	3.01	2.10	4.11	3.82	3.20	1.99
30	4.91	5.68	3.55	1.93	4.24	3.82	3.21	2.05	3.98	4.35	3.01	2.09	4.10	3.83	3.20	1.98
32	4.95	5.62	3.55	1.93	4.25	3.79	3.22	2.03	3.97	4.35	3.01	2.09	4.10	3.82	3.20	1.99

Note: IT and OT correspond to the indoor and outdoor dry bulb temperatures, respectively.

Table 4.18: Air conditioning COPs.

IT °C	Size															
	Small				Medium				Large				Extra large			
	OT °C															
	-15	-10	7	24	-15	-10	7	24	-15	-10	7	24	-15	-10	7	24
16	2.22	2.41	3.66	4.03	2.16	2.41	3.63	3.97	2.05	2.40	3.62	4.07	1.81	2.13	3.22	3.66
18	2.21	2.41	3.66	4.02	2.15	2.42	3.63	3.99	2.05	2.40	3.61	4.04	1.81	2.13	3.22	3.67
20	2.21	2.39	3.67	4.03	2.15	2.41	3.62	3.98	2.05	2.39	3.62	4.05	1.81	2.13	3.22	3.67
21	2.21	2.40	3.68	4.03	2.15	2.41	3.62	3.98	2.05	2.39	3.63	4.07	1.81	2.13	3.21	3.67
22	2.20	2.41	3.67	4.03	2.15	2.41	3.62	3.98	2.05	2.39	3.63	4.07	1.82	2.14	3.21	3.68
24	2.21	2.40	3.68	4.03	2.15	2.42	3.61	3.99	2.05	2.39	3.63	4.07	1.81	2.14	3.20	3.67

Note: IT and OT correspond to the indoor and outdoor dry bulb temperatures, respectively.

Table 4.16: Air conditioning parameters.

Size		Small	Medium	Large	
Model	Name	Slim 1 way cassete			Units
	Indoor Unit	AC035FBNDEH/EU	AC052FBNDEH/EU	AC060FBNDEH/EU	
	Outdoor Unit	AC035FCADEH/EU	AC052FCADEH/EU	AC060FCADEH/EU	
Capacity	Cooling (Min / Std / Max)	0.99/3.50/4.20	1.30/5.00/5.90	1.80/5.80/6.50	kW
	Sensible heat ratio (SHR)	0.75			-
	Heating (Min / Std / Max)	0.98/4.00/5.00	1.30/5.50/7.50	1.60/7.00/9.00	kW
Power Input	Cooling (Min / Std / Max)	0.24/1.09/1.45	0.31/1.66/2.10	0.38/1.81/2.60	kW
	Heating (Min / Std / Max)	0.18/1.11/1.40	0.35/1.61/2.40	0.35/2.18/3.60	
Energy Efficiency	EER (Nominal Cooling)	3.21	3.01	3.20	–
	COP (Nominal Heating)	3.60	3.42	3.21	
Indoor Unit	Air flow rate (High / Mid / Low)	158/133/108	200/175/150	183/167/150	L/s
Outdoor Unit	Air flow rate (High / Mid / Low)	500	550	833	L/s
	Operating temp. range (Cooling)	[-10,46]	[-10,46]	[-15,46]	$°C$
	Operating temp. range (Heating)	[-15,24]	[-15,24]	[-20,24]	

4.6.11.1 ALG AC 01

The algorithm 6 receives as input the heat contributed by the occupants in the next time step Q_{occ}^{i+1}, the interpolated COP^{i+1} and EER^{i+1}, the current operating mode $mode_{AC}^{i}$, and the current temperatures of the nodes. First, it asks if there will be no occupants present in the next time step:

- If so, (C) then it enters shutdown mode.
- Otherwise, it then asks if the indoor temperature T_H is lower than the minimum comfort range temperature T_{min}.
  - If so, it asks if there was cooling in the last hour.
    - If so, it proceeds with C.
    - Otherwise, (A) the system enters heating mode at nominal power.
- Otherwise, it asks if T_H is greater than the maximum comfort range temperature T_{max}.
  - If so, it asks if there was heating in the last hour.
    - If so, it proceeds with C.
    - Otherwise, (B) the system enters cooling mode at nominal power.
- Otherwise, if there are occupants present and T_H remains within the comfort range, then it continues to maintain the operating mode from the previous time step. Finally, it calculates the thermal resistances and updates the temperatures of the nodes.

4.6.11.2 ALG AC 02

The algorithm 7 receives as input the heat contributed by the occupants in the next time step Q_{occ}^{i+1}, the interpolated COP^{i+1} and EER^{i+1}, the current operating mode $mode_{AC}^{i}$, the average outdoor temperature during the last week T_{aR}^{i+1}, the average outdoor temperature during the last year T_{aY}^{i+1}, the current temperatures of the nodes, the available surplus power to be self-consumed P_{d}^{i+1}, the special operating mode S_{mode}^{i}, and the change in comfort range temperature I.

- First, it asks if there will be no occupants present in the next time step. If so, (C) then it enters shutdown mode.
- Otherwise, it asks if S_{mode}^{i} is in self-consumption mode.
  - If so, it asks if T_{aR}^{i+1} exceeds T_{aY}^{i+1}.
    - If so, it seeks to overcool, reducing T_{max} and T_{min} by a margin I.
    - Otherwise, it seeks to overheat, increasing the comfort temperature range.
  - Then, it asks if T_H is lower than the new T_{min}.
    - If so, it asks if there was cooling in the last hour, or if P_{d}^{i+1} is not enough to reach the nominal power required by the system.

Algorithm 6 ALG AC 01

Input: Q_{occ}^{i+1}, COP^{i+1}, EER^{i+1}, $mode_{AC}^{i}$, T_H^i, T_W^i, T_R^i, T_{ws}^i
Output: $mode_{AC}^{i+1}$, T_H^{i+1}, T_W^{i+1}, T_R^{i+1}, T_{ws}^{i+1}

if $Q_{occ}^{i+1} = 0$ **then**
  C: mode$_{AC}^{i+1} = Off$; $Q_u^{i+1} = 0$
else if $T_H^i < T_{min}$ **then**
  if $t_{\text{current}} - t_{\text{last\_cooling}} < 1\text{h}$ **then**
    C
  else
    A: $mode_{AC}^{i+1} = Heating$, $Q_u^{i+1} = P_{hnom} COP^{i+1}$
  end if
else if $T_H^i > T_{max}$ **then**
  if $t_{\text{current}} - t_{\text{last\_heating}} < 1\text{h}$ **then**
    C
  else
    B: $mode_{AC}^{i+1} = Cooling$, $Q_{ureq}^{i+1} = P_{cnom} EER^{i+1} SHR$
  end if
else if $mode_{AC}^{i} = Heating$ **then**
  A
else if $mode_{AC}^{i} = Cooling$ **then**
  B
else
  C
end if
Calculate thermal resistances
Calculate material temperatures

  - If so, the system enters the special Recovering mode and goes back to (C), taking advantage of thermal inertia and waiting for T_H to return to the normal comfort range.
  - Otherwise, it enters heating mode at nominal power.

- Otherwise, it asks if T_H is greater than the new T_{max}.
  - If so, it asks if there was heating in the last hour, or if P_d^{i+1} is not enough to reach the nominal power required by the system.
    - If so, the system enters the special Recovering mode and goes back to (C).
    - Otherwise, it enters cooling mode at nominal power.
- Otherwise, if the previous mode was heating, then it proceeds with (A). Alternatively, if the mode was cooling, then it proceeds with (B). Otherwise, it proceeds with (B).

- Otherwise, it asks if S_{mode}^{i} is in special Recovering mode.
  - If so, if there was a heating period but still T_H is lower than T_{min}, or if there was a cooling period but still T_H is greater than T_{max}, then it continues with ALG AC 01.
  - Otherwise, it maintains the special Recovering mode and goes back to (C).
- Finally, it calculates the thermal resistances and updates the temperatures of the nodes.

Algorithm 7 ALG AC 02

Input: Q_{occ}^{i+1}, COP^{i+1}, EER^{i+1}, $mode_{AC}^{i}$, T_H^i, T_W^i, T_R^i, T_{ws}^i, P_d^{i+1},S_{mode}^{i}, I

Output: $mode_{AC}^{i+1}$, T_H^{i+1}, T_W^{i+1}, T_R^{i+1}, T_{ws}^{i+1}

if $Q_{occ}^{i+1} = 0$ **then**
  C: $Q_u^{i+1} = 0$; mode$_{AC}^{i+1} = Off$
else if S_{mode}^{i+1} = Self-consumption **then**
  if $T_{aR}^{i+1} \geq T_{aY}^{i+1}$ **then**
    $T_{max} = T_{max} - I$; $T_{min} = T_{min} - I$
  else
    $T_{max} = T_{max} + I$; $T_{min} = T_{min} + I$
  end if
  if $T_H^i < T_{min}$ **then**
    if A: $t_{\text{current}} - t_{\text{last\_cooling}} < 1\text{h}$ **or** $P_d^{i+1} < P_{hnom}$ **then**
      S_{mode}^{i+1} = Recovering, C
    else
      $mode_{AC}^{i+1}$ = Heating, $Q_u^{i+1} = P_{hnom} COP^{i+1}$
    end if
  else if $T_H^i > T_{max}$ **then**
    if B: $t_{\text{current}} - t_{\text{last\_heating}} < 1\text{h}$ **or** $P_d^{i+1} < P_{cnom}$ **then**
      S_{mode}^{i+1} = Recovering, C
    else
      $mode_{AC}^{i+1}$ = Cooling, $Q_u^{i+1} = P_{cnom} EER^{i+1} SHR$
    end if
  else if $mode_{AC}^{i} = Heating$ **then**
    A
  else if $mode_{AC}^{i} = Cooling$ **then**
    B
  else
    C
  end if
else if $S_{mode}^{i} = Recovering$ **then**
  if $mode_{AC}^{i} = Heating$ **and** $T_H^i < T_{min}$ **then**
    Continue with ALG AC 01
  else if $mode_{AC}^{i} = Cooling$ **and** $T_H^i > T_{max}$ **then**
    Continue with ALG AC 01
  else
    S_{mode}^{i+1} = Recovering, C
  end if
end if
Calculate thermal resistances
Calculate material temperatures

4.6.11.3 ALG AC 03

The algorithm 8 receives as input the heat contributed by the occupants in the next time step Q_{occ}^{i+1}, the interpolated COP^{i+1} and EER^{i+1}, the current operating mode $mode_{AC}^{i}$, the current temperatures of the nodes, the set-point temperature T_{sp}, and the tolerance margin M with respect to the T_{sp}.

- First, it asks if there will be no occupants present in the next time step. If so, (C) then it enters shutdown mode.
- Otherwise, it then asks if T_{sp} is above T_H by a value greater than M.
  - If so, it asks if there was cooling in the last hour.
    - If so, it proceeds with C.
    - Otherwise, (A) the system enters heating mode and calculates the required heat Q_{ureq}^{i+1} to reach T_{sp}.
      - Then it asks if the required input power exceeds the maximum operating input power P_{hmax}. If so, the input power is limited to P_{hmax}.
      - Otherwise, it asks if the required input power is less than the minimum operating input power P_{hmin}. If so, it proceeds with (C).
      - Otherwise, the system provides a heat gain equivalent to Q_{ureq}^{i+1}.
- Otherwise, it then asks if T_{sp} is below T_H by a value greater than M.
  - If so, it asks if there was heating in the last hour.
    - If so, it proceeds with C.
    - Otherwise, (B) the system enters cooling mode and calculates the required heat Q_{ureq}^{i+1} to reach T_{sp}.
      - Then it asks if the required input power exceeds the maximum operating input power P_{cmax}. If so, the input power is limited to P_{cmax}.
      - Otherwise, it asks if the required input power is less than the minimum operating input power P_{cmin}. If so, it proceeds with (C).
      - Otherwise, the system provides a heat gain equivalent to Q_{ureq}^{i+1}.
- Otherwise, if the previous mode was heating, then it proceeds with (A). Alternatively, if the mode was cooling, then it proceeds with (B). Otherwise, it proceeds with (B). Finally, it calculates the thermal resistances and updates the temperatures of the nodes.

Q_{ureq}^{i+1} is obtained by Newton-Raphson iteration, seeking the required heat to reach the set point temperature in T_H. The iteration equation is determined as given in (4.69), where Q_u^{n+1} is the obtained value , Q_u^n is the value of the previous iteration, T_H^n is the internal temperature evaluated in the previous iteration, T_{sp} is the set point temperature, Δt is the time step, and C_H is the internal air heat capacity of the home.

$$Q_u^{n+1} = Q_u^n - \frac{T_H^n - T_{sp}}{\Delta t C_H} \tag{4.69}$$

Algorithm 9 shows the iteration procedure. First, the tolerance is defined to stop the iteration when the value has converged. In this case, a tolerance of 1W was considered. The initial value of the iteration Q_u^0 is also defined. Then, the temperatures are calculated with this initial value. Subsequently, $T_H(Q_u^0)$ and $T_H^{'}(Q_u^0)$ are calculated to obtain the value of the first iteration Q_u^n. If the difference between the values of iterations n and $n+1$ is less than the tolerance, then the iteration process has converged. Otherwise, the iteration is repeated in a repetitive cycle until convergence is reached.

Algorithm 8 ALG AC 03

Input: Q_{occ}^{i+1}, COP^{i+1}, EER^{i+1}, $mode_{AC}^{i}$, T_H^i, T_W^i, T_R^i, T_{ws}^i, T_{sp}, M

Output: $mode_{AC}^{i+1}$, T_H^{i+1}, T_W^{i+1}, T_R^{i+1}, T_{ws}^{i+1}

if $Q_{occ}^{i+1} = 0$ **then**
  C: $Q_u^{i+1} = 0$; mode$_{AC}^{i+1} = Off$
else if $T_{sp} - T_H^i > M$ **then**
  if $t_{\text{current}} - t_{\text{last\_cooling}} < 1\text{h}$ **then**
    C
  else
    A: $mode_{AC}^{i+1} = Heating$, $Q_{ureq}^{i+1} = f_{NR}(T_{sp}, T_H^i)$
    if $Q_{ureq}^{i+1}/COP^{i+1} > P_{hmax}$ **then**
      $Q_u^{i+1} = P_{hmax}COP^{i+1}$
    else if $Q_{ureq}^{i+1}/COP^{i+1} < P_{hmin}$ **then**
      C
    else
      $Q_u^{i+1} = Q_{ureq}^{i+1}$
    end if
  end if
else if $T_{sp} - T_H^i < -M$ **then**
  if $t_{\text{current}} - t_{\text{last\_heating}} < 1\text{h}$ **then**
    C
  else
    B: $mode_{AC}^{i+1} = Cooling$, $Q_{ureq}^{i+1} = f_{NR}(T_{sp}, T_H^i)$
    if $Q_{ureq}^{i+1}/(EER^{i+1}SHR) > P_{cmax}$ **then**
      $Q_u^{i+1} = -P_{cmax}EER^{i+1}SHR$
    else if $Q_{ureq}^{i+1}/(EER^{i+1}SHR) < P_{cmin}$ **then**
      C
    else
      $Q_u^{i+1} = Q_{ureq}^{i+1}$
    end if
  end if
else if $mode_{AC}^{i} = Heating$ **then**
  A
else if $mode_{AC}^{i} = Cooling$ **then**
  B
else
  C
end if
Calculate thermal resistances
Calculate material temperatures

Algorithm 9 Q_{ureq}^{i+1} calculation

Input: $T_a^i, Q_R^i, Q_L^i, Q_{inf}^i, T_H^i, T_W^i, T_R^i, T_{ws}^i, T_{sp}^i$
Output: Q_{ureq}^{i+1}

Tolerance = 1; $Q_u^0 = 0$
Compute temperatures using Q_u^0
$T_H(Q_u^0) = T_H^0$ - T_{sp} ; $T_H^{'}(Q_u^0) = \Delta t / C_H$
$Q_u^n = Q_u^0$ - $T_H(Q_u^0)/T_H^{'}(Q_u^0)$
if $abs(Q_u^n - Q_u^0) <$ Tolerance **then**
    $Q_{ureq}^{i+1} = Q_u^n$
else
    Condition = FALSE
    repeat
        Compute temperatures using Q_u^n
        $T_H(Q_u^n) = T_H^n$ - T_{sp} ; $T_H^{'}(Q_u^n) = \Delta t / C_H$
        $Q_u^{n+1} = Q_u^n$ - $T_H(Q_u^n)/T_H^{'}(Q_u^n)$
        if $abs(Q_u^{n+1} - Q_u^n) <$ Tolerance **then**
            Condition = TRUE
            $Q_{ureq}^{i+1} = Q_u^{n+1}$
        else
            $Q_u^n = Q_u^{n+1}$
        end if
    until $Condition == TRUE$
end if

4.6.11.4 ALG AC 04

The algorithm 10 receives as input the heat contributed by the occupants in the next time step Q_{occ}^{i+1}, the interpolated COP^{i+1} and EER^{i+1}, the current operating mode $mode_{AC}^i$, the setpoint temperature T_{sp}, the average outdoor temperature during the last week T_{aR}^{i+1}, the average outdoor temperature during the last year T_{aY}^{i+1}, the current temperatures of the nodes, the available surplus power to be self-consumed P_d^{i+1}, the special operating mode S_{mode}^i, the change in comfort range temperature I, and the tolerance margin M with respect to the T_{sp}.

- First, it asks if there will be no occupants present in the next time step. If so, (C) then it enters shutdown mode.
- Otherwise, it asks if S_{mode}^i is in self-consumption mode.
  - If so, it asks if T_{aR}^{i+1} exceeds T_{aY}^{i+1}.
    - If so, it seeks to overcool, reducing T_{sp} by a margin I.
    - Otherwise, it seeks to overheat, increasing the temperature setpoint.
  - Then, it asks if the new setpoint T_{spo} is higher than T_H by a value greater than M.

        * If so, it asks if there was cooling in the last hour, or if P_d^{i+1} is not enough to reach the minimum input power P_{hmin}.

            · If so, the system enters the special Recovering mode and goes back to (C), taking advantage of thermal inertia and waiting for T_H to return to the normal comfort range.

            · Otherwise, it enters heating mode and calculates the required heat to reach the setpoint Q_{ureq}^{i+1}. Then the heat provided Q_u^{i+1} will be the minimum between Q_{ureq}^{i+1}/COP^{i+1}, P_d^{i+1}, and P_{hmax}, multiplied by COP^{i+1}.

    – Otherwise, it asks if the new setpoint T_{spo} is lower than T_H by a value greater than M.

        * If so, it asks if there was heating in the last hour, or if P_d^{i+1} is not enough to reach the minimum input power P_{cmin}.

            · If so, the system enters the special Recovering mode and goes back to (C).

            · Otherwise, it enters cooling mode and calculates the required heat to reach the setpoint Q_{ureq}^{i+1}. Then the heat provided Q_u^{i+1} will be the minimum between $Q_{ureq}^{i+1}/(EER^{i+1}SHR)$, P_d^{i+1}, and P_{cmax}, multiplied by $EER^{i+1}SHR$.

    – Otherwise, if the previous mode was heating, then it proceeds with (A). Alternatively, if the mode was cooling, then it proceeds with (B). Otherwise, it proceeds with (B).

- Otherwise, it asks if S^i_{mode} is in special Recovering mode.

    – If so, if there was a heating period but T_H is still below the setpoint by a value greater than M, or if there was a cooling period but T_H is still above the setpoint by a value greater than M, then it continues with ALG AC 03.

    – Otherwise, it maintains the special Recovering mode and goes back to (C).

- Finally, it calculates the thermal resistances and updates the temperatures of the nodes.

Algorithm 10 ALG AC 04

Input: Q_{occ}^{i+1}, COP^{i+1}, EER^{i+1}, $mode_{AC}^{i}$, T_{sp}, T_{aR}^{i+1}, T_{aY}^{i+1}, T_{H}^{i}, T_{W}^{i}, T_{R}^{i}, T_{ws}^{i}, P_{d}^{i+1}, S^{i}_{mode}, I, M

Output: $mode_{AC}^{i+1}$, T_{H}^{i+1}, T_{W}^{i+1}, T_{R}^{i+1}, T_{ws}^{i+1}

if $Q_{occ}^{i+1} = 0$ **then**
  C: $Q_{u}^{i+1} = 0$; mode$_{AC}^{i+1} = Off$
else if S^{i+1}_{mode} = Self-consumption **then**
  if $T_{aR}^{i+1} \geq T_{aY}^{i+1}$ **then**
    $T_{spo} = T_{sp} - I$
  else
    $T_{spo} = T_{sp} + I$
  end if
  if $T_{spo} - T_{H}^{i} > M$ **then**
    if A: $t_{\text{current}} - t_{\text{last\_cooling}} < 1\text{h}$ **or** $P_{d}^{i+1} < P_{hmin}$ **then**
      S^{i+1}_{mode} = Recovering, C
    else
      $mode_{AC}^{i+1}$ = Heating, $Q_{ureq}^{i+1} = f_{NR}(T_{sp}, T_{H}^{i})$, $Q_{u}^{i+1} = min(\frac{Q_{ureq}^{i+1}}{COP^{i+1}}, P_{d}^{i+1}, P_{hmax})COP^{i+1}$
    end if
  else if $T_{spo} - T_{H}^{i} < -M$ **then**
    if B: $t_{\text{current}} - t_{\text{last\_heating}} < 1\text{h}$ **or** $P_{d}^{i+1} < P_{cmin}$ **then**
      S^{i+1}_{mode} = Recovering, C
    else
      $mode_{AC}^{i+1}$ = Cooling, $Q_{ureq}^{i+1} = f_{NR}(T_{sp}, T_{H}^{i})$, $Q_{u}^{i+1} = -min(\frac{Q_{ureq}^{i+1}}{EER^{i+1}SHR}, P_{d}^{i+1}, P_{cmax})\ EER^{i+1}SHR$
    end if
  else if $mode_{AC}^{i} = Heating$ **then**
    A
  else if $mode_{AC}^{i} = Cooling$ **then**
    B
  else
    C
  end if
else if $S^{i}_{mode} = Recovering$ **then**
  if $mode_{AC}^{i} = Heating$ **and** $T_{sp} - T_{H}^{i} > M$ **then**
    Continue with ALG AC 03
  else if $mode_{AC}^{i} = Cooling$ **and** $T_{sp} - T_{H}^{i} < -M$ **then**
    Continue with ALG AC 03
  else
    S^{i+1}_{mode} = Recovering, C
  end if
end if
Calculate thermal resistances
Calculate material temperatures

4.7 Thermal Comfort Model

The thermal comfort of occupants is based on thermal sensation, which is affected by both internal and external physical factors, as well as psychological factors. In the literature, various methodologies have been formulated for its estimation in a quantitative manner using empirical expressions [64]. In physical terms, thermal comfort is achieved when the body temperature is maintained within certain comfort ranges (primarily temperature and humidity), the skin humidity is low, and the physiological effort to regulate the temperature is low (which is influenced by levels of perspiration, vasodilation, vasoconstriction, among other biological phenomena).

One of the thermal comfort estimators currently used is the Predicted Mean Vote (PMV) index, which provides a hypothetical average response of a large group of people according to the ASHRAE thermal sensation scale (+3 Hot, +2 Warm, +1 Slightly warm, 0 Neutral, -1 Slightly cool, -2 Cool, -3 Cold) [65]. It is obtained through Fanger's comfort equation for human body heat exchange. This model assumes that the body is a single mass and is used in the context of steady-state conditioned environments [64], meaning without significant disturbances in environmental variables, and assuming that the body remains in thermodynamic equilibrium, where there is no net heat gain or loss. Due to the above, we estimate the PMV index in the current work when the temperature does not undergo abrupt changes, and assuming that the human body has reached its thermodynamic equilibrium. The energy balance of the human body can be modeled using Figure 4.23, which is determined as given in (4.70).

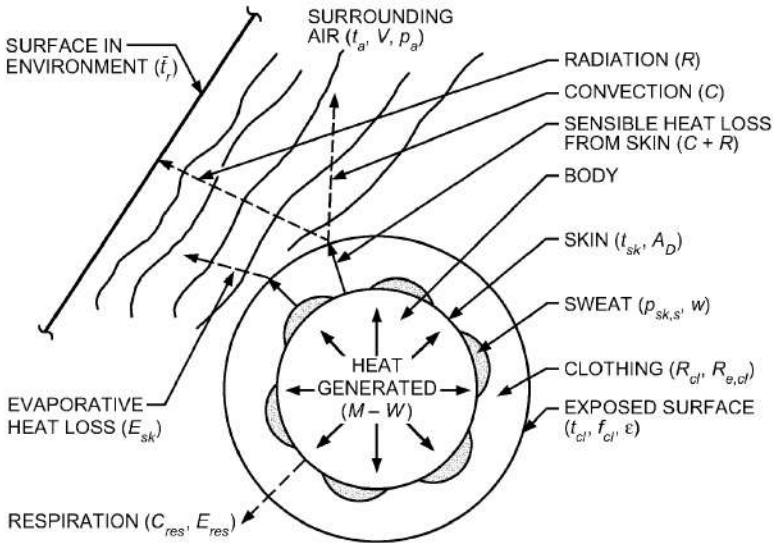

Figure 4.23: Energy thermal balance of human body [65].

$$M - W = q_{sk} + q_{res} + S \tag{4.70}$$

Where M is the metabolic rate of the body, W is the rate of mechanical work done, q_{sk} is the rate of heat loss through the skin, q_{res} is the rate of heat loss through perspiration, and S is the rate of heat accumulation in the body. Now, the approach can be made more specific through (4.71).

$$M - W = (C + R + E_{sk}) + (C_{res} + E_{res}) + (S_{sk} + S_{cr}) \tag{4.71}$$

Where C and R correspond to the rates of sensible heat loss through the skin by convective and radiative effects, respectively, E_{sk} is the rate of latent heat loss through the skin (evaporation of sweat), C_{res} is the rate of sensible heat loss by convection from respiration, E_{res} is the rate of latent heat loss through respiration (exhalation of water vapor), S_{sk} is the rate of heat accumulation in the skin (external surface), and S_{cr} is the rate of heat accumulation in the core (internal volume). However, Fanger in [66] proposed the simplification of equation (4.71) to equation 4.72, in the case of conventional clothing and typical indoor environments with low or moderate activity levels, where it is assumed that the sweat of the occupants evaporates completely. In this way, PVM calculation for conventional cases is determined as given in (4.72) [64].

$$\begin{aligned} PMV = [0.303e^{-0.036M} + 0.028][(M - W) - 3.05 \cdot 10^{-3}(5733 - 6.99(M - W) - p_{ia}) + 0.42[(M - W) \\ - 58.15] + 1.7 \cdot 10^{-5} M(5867 - p_{ia}) - 0.0014M(34 - T_H) - 3.96 \cdot 10^{-8} f_{cl}[(T_{cl} + 273)^4 \\ - (T_{MR} + 273)^4] - f_{cl} h_c (T_{cl} - T_H)] \end{aligned} \tag{4.72}$$

Where p_{ia} is the indoor water vapor pressure, f_{cl} is the ratio of clothed surface, T_{cl} is the clothing surface temperature, T_{MR} is the mean radiant temperature, and h_c is the convective heat transfer coefficient. p_{ia} is first obtained by calculating the external saturated water vapor pressure (P_{ews}) as given in (4.73).

$$\begin{aligned} P_{ews} = 1000 \exp\Big[-5800(T_a + 273)^{-1} - 5.516 - 0.04864(T_a + 273) + 4.176 \cdot 10^{-5}(T_a + 273)^2 \\ - 1.445 \cdot 10^{-8}(T_a + 273)^3 + 6.546 \ln(T_a + 273) \Big] \end{aligned} \tag{4.73}$$

Then, the external specific humidity H_{se} is determined as given in (4.74).

$$H_{se} = \frac{R_{da}}{R_w} \left(\frac{P_T}{P_{ews} RH_a} - 1 \right)^{-1} \tag{4.74}$$

Where R_{da} and R_w are the specific gas constants for dry air and water vapor, respectively, P_T is the atmospheric absolute pressure, and RH_a is the ambient relative humidity. It is assumed that the indoor specific humidity H_{si} is equal to H_{se}, assuming that there are no significant internal sources of water and the contribution of vapor from occupants is negligible. Finally, the indoor water vapor pressure (p_{ia}) is determined as given in (4.75).

$$p_{ia} = P_T \left(\frac{R_{da}}{R_w H_{si}} + 1 \right)^{-1} \tag{4.75}$$

On the other hand, T_{MR} is obtained from the form factors of each interior surface with respect to the

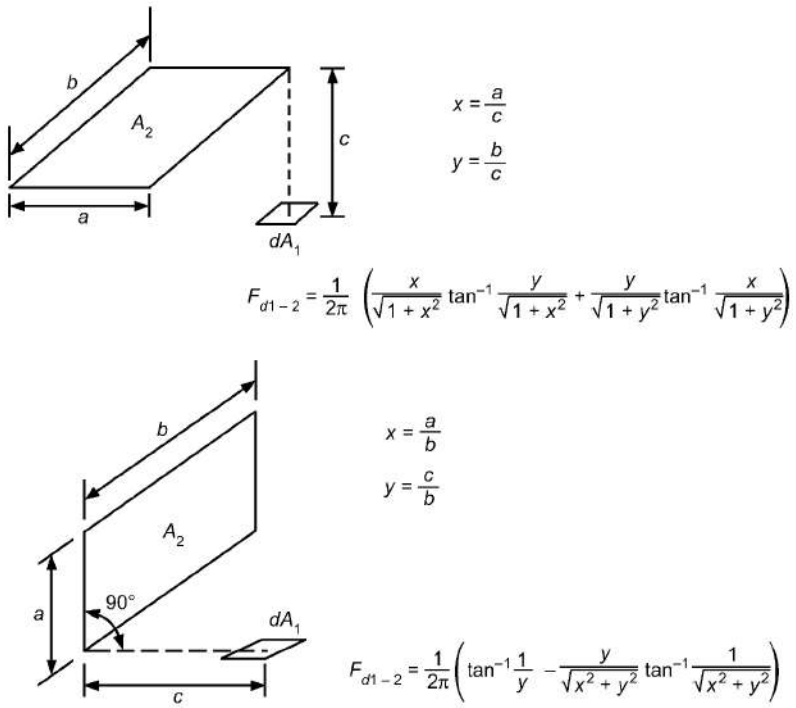

Figure 4.24: Analytical formulas for calculating angle factor for small plane element [65].

person. Figure 4.24 shows the analytical formulas for obtaining the form factors for the upper and lower interior surfaces (upper approach), as well as for the wall surfaces (lower approach). The occupant is modeled as an infinitesimal surface at the center of the home, without the existence of internal walls. Each internal surface is divided into four quadrants with equivalent form factors. The form factors of the ceiling F_{up} and the floor F_{down} are determined as given in (4.76).

$$F_V = \frac{\arctan\left[\frac{b/c}{(1+(a/c)^2)^{0.5}}\right]a}{2\pi c[1+(a/c)^2]^{0.5}} + \frac{\arctan\left[\frac{a/c}{(1+(b/c)^2)^{0.5}}\right]b}{2\pi c[1+(b/c)^2]^{0.5}} \tag{4.76}$$

Where a, b, and c are the width, length, and distance of the quadrant to the person, respectively. The form factors of the lateral walls (F_{HL}) and the frontal walls (F_{HA}) are determined as given in (4.77).

$$F_H = \frac{\arctan[1/(\frac{c}{b})]}{2\pi} - \frac{\frac{c}{b}\cdot\arctan[([\frac{a}{b}]^2+[\frac{c}{b}]^2)^{-0.5}]}{2\pi[(\frac{a}{b})^2+(\frac{c}{b})^2]^{0.5}} \tag{4.77}$$

Where a, b, and c are the height, length, and distance of the quadrant to the person, respectively. Then, T_{MR} is determined as given in (4.78).

$$T_{MR} = \sqrt[4]{4T_R^4 F_{\text{up}} + 4T_F^4 F_{\text{down}} + 8T_W^4(F_{\text{HL}} + F_{\text{HA}})} \tag{4.78}$$

Where T_F is the floor temperature, assumed to be equal to T_W. On the other hand, f_{cl} is determined as given in (4.79).

$$f_{cl} = \begin{cases} 1 + 0.2I_{cl} & \text{if } I_{cl} < 0.5clo \\ 1.05 + 0.1I_{cl} & \text{if } I_{cl} > 0.5clo \end{cases} \tag{4.79}$$

Where I_{cl} is the clothing insulation, assumed as 1.3clo and 0.36clo for winter and summer months, respectively. Finally, T_{cl} and h_c are determined as given in (4.80) and (4.81), where v_{ar} is the relative air velocity, assumed as 0.1m/s. The model was solved using iterative processes, utilizing the Python package *pythermalcomfort* [67].

$$T_{cl} - 35.7 + 0.28(M - W) + I_{cl}[3.96 \cdot 10^8 f_{cl}[(T_{cl} + 273)^4 - (T_{MR} + 273)^4] + f_{cl}h_c(T_{cl} - T_{db})] = 0 \tag{4.80}$$

$$h_c = max(2.38|T_{cl} - T_H|^{0.25}, 12.1\sqrt{v_{ar}}) \tag{4.81}$$

4.8 Key performance indicators calculation

KPIs were obtained for both the RCs and the community. The RCs' bills include the cost of electricity consumption from both the UG and the P2P market, minus injections to the UG and the P2P market. The community cost is the sum of all the RCs' bills. The SCR and SSR are obtained for the microgrid, defined as given in (4.82) and (4.83), respectively. Finally, the energy imported from the UG during critical periods is determined from the periods defined in section 5.5.

$$SCR = \left(1 - \frac{\text{Energy injected into the UG}}{\text{Total local PV generation}}\right) \cdot 100 \tag{4.82}$$

$$SSR = \left(1 - \frac{\text{Energy imported from the UG}}{\text{Total energy consumption}}\right) \cdot 100 \tag{4.83}$$

5 | Study Case

5.1 Location

Figure 5.1 represents the case study under examination, located within a private residential condominium of typical homes in Viña del Mar, Chile, which consists of two prosumers, two consumers, one aggregator responsible for coordinating the P2P market, and the UG.

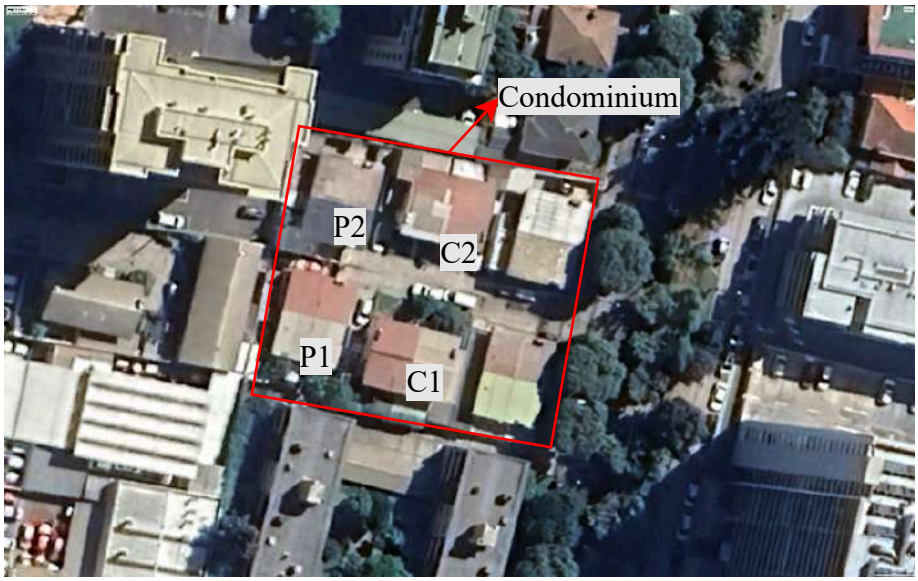

Figure 5.1: Location of the residential condominium.

5.2 Meteorological data

Meteorological data was obtained for the location with coordinates 33.01° latitude and 71.32° longitude. From [42], data on solar irradiation (S_i), dry bulb temperature (T_a), and wind speed (W_v) were obtained for a typical meteorological year (TMY), with hourly resolution (see Figure 5.2). Similarly, data on annual relative humidity (RH_a) were obtained from [68], with hourly resolution (see Figure 5.3). The databases were interpolated for the time step used. Finally, wet bulb temperature (T_{wb}) data was obtained using the methodology presented in section 4.5.4 (see Figure 5.4). Table 5.1 shows the minimum, average, and maximum values of the meteorological variables.

Table 5.1: Summary of meteorological variables.

Variable	Minimum	Average	Maximum	Unit
Dry bulb temperature (T_a)	1.9	14.2	29.5	$°C$
Relative humidity (RH_a)	13	76.9	100	$\%$
Wet bulb temperature (T_{wb})	-1.1	11.6	28.3	$°C$
Solar irradiation (S_i)	0	230	1140	W/m^2
Wind velocity (W_v)	0	1.6	8.1	m/s

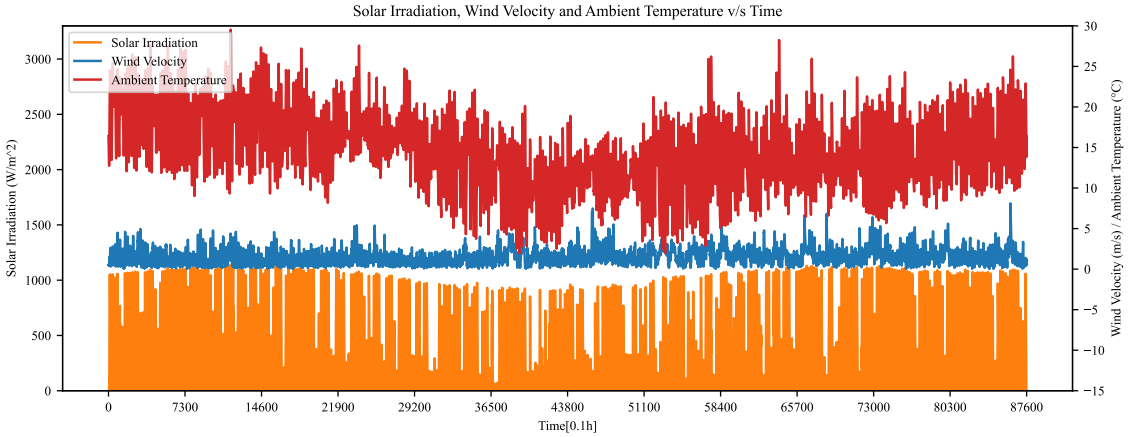

Figure 5.2: Graph of annual data on solar irradiation, dry bulb ambient temperature, and wind speed.

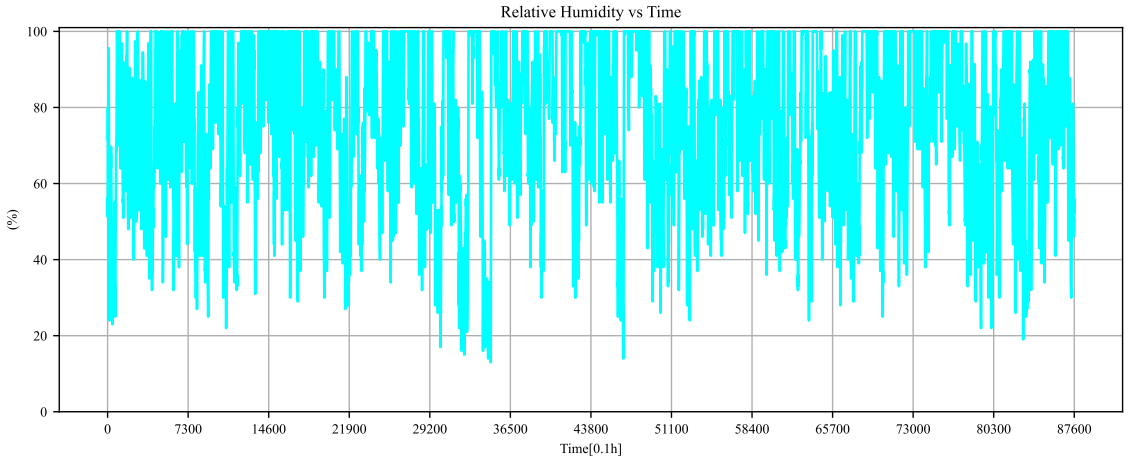

Figure 5.3: Graph of annual data on relative humidity.

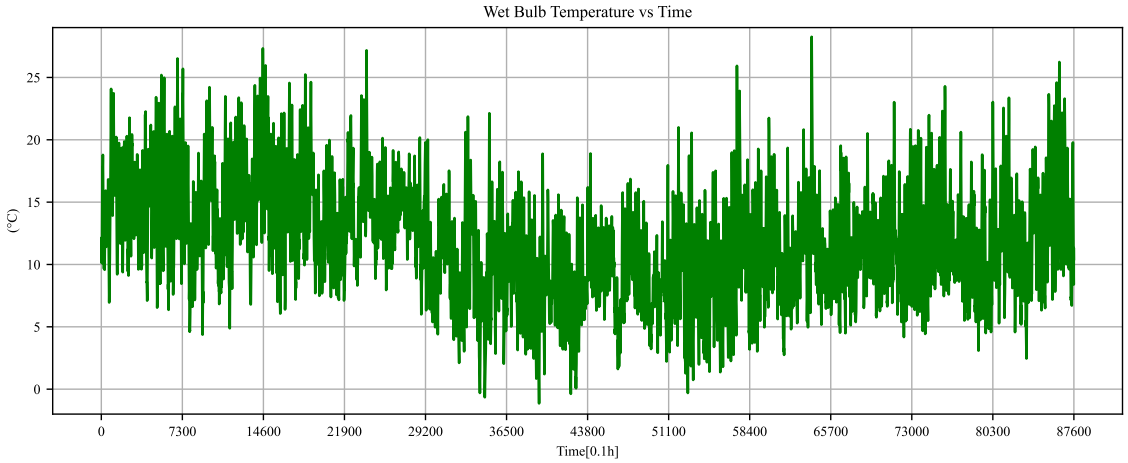

Figure 5.4: Graph of annual data on wet bulb ambient temperature.

5.3 Occupancy profiles

Typical residential occupancy profiles were obtained from [69]. Each home is occupied by an inhabitant with different occupancy profiles. These profiles vary according to the type of inhabitant, type of day, and season of the year. Table 5.2 summarizes the occupancy hourly ranges for each home.

Table 5.2: Occupancy hourly ranges.

Residential customer	Station	Weekday	Weekend
Prosumer 1	Summer	14:00-8:00	All day
	Winter	All day	All day
Prosumer 2	Summer	19:00-11:00	All day
	Winter	18:00-13:00	All day
Consumer 1	Summer	18:00-10:00	20:00-10:00
	Winter	15:00-8:00	18:00-12:00
Consumer 2	Summer	19:00-8:00	10:00-20:00
	Winter	19:00-8:00	18:00-12:00

5.4 Electrical base annual load profiles

Base load profiles were obtained from open-access databases, derived from Energyplus, with hourly resolution based on a TMY [70]. These profiles encompass consumption related to lighting, household appliances, and miscellaneous devices, with no significant seasonal variations. Profiles 1 and 2 present an annual consumption of 3722 and 3022kWh/year, respectively. Figure 5.5 represents a sample for profile 1 during 2nd-3rd January. The databases were interpolated to the time step used in the simulation. Additionally, a smoothing of the curve was applied using Exponential Weighted Moving Average (EWMA) to avoid abrupt changes in the curve after interpolation. EWMA uses decreasing exponential weights for past values, meaning that more recent values have a greater weight in the moving average calculation.

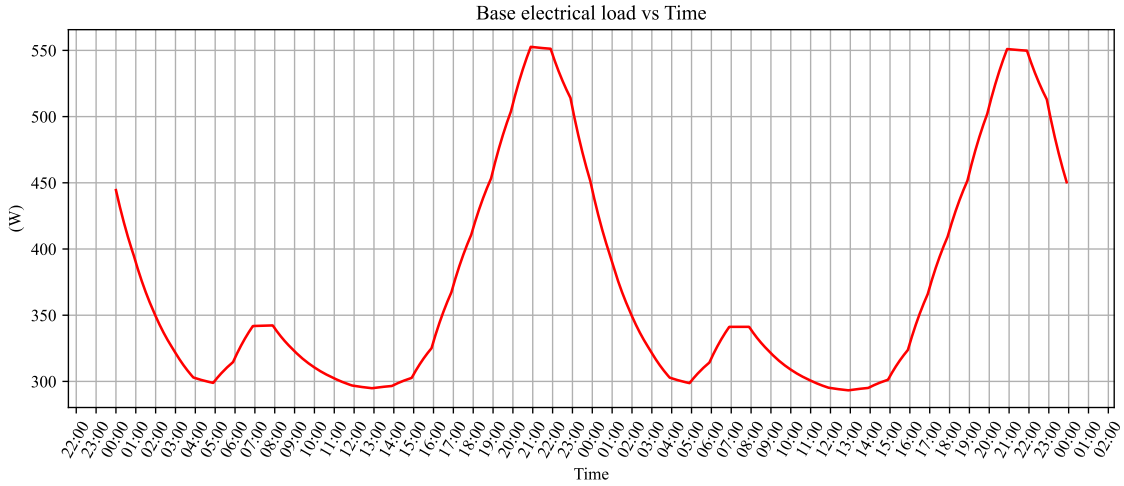

Figure 5.5: Base electrical load profile 1 between 2st-3th January.

5.5 Utility grid critical consumption periods

To determine the critical consumption periods on the utility grid, open-access local consumption data from the National Electric Coordinator for the year 2023 [71] were collected. Figure 5.6 shows the average daily consumption curves for each month of the year. It can be observed that the curves for all months have a similar shape; however, the critical consumption periods vary from one season to another.

It is assumed that critical periods correspond to times of absence or deficit of solar resources. In this way, the critical hour is assumed to begin when there is a sudden increase in total demand, and ends when consumption levels return to pre-increase levels. For example, during the winter months of June and July, the critical period starts from 17:00pm until demand returns to the same level at 23:30pm, reaching its peak hour at 19:00pm, while during the summer months of December and January, the critical period is from 19:00pm to 22:30pm, with its peak hour at 19:00pm. Table 5.3 summarizes the assumed critical hours and peak consumption hours for each month of the year.

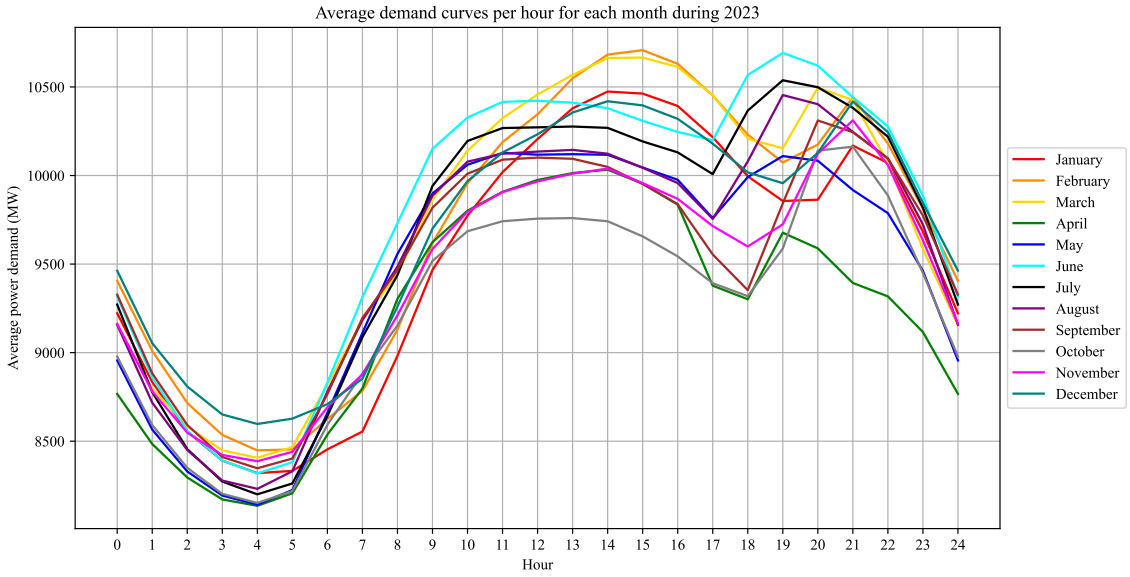

Figure 5.6: Average demand curves per hour for each month during 2023. [71].

Table 5.3: Critical hours and peak hours for each month of the year [71].

Month	Critical consumption period	Peak hour
January	20:00 - 22:30	21:00
February	19:00 - 22:30	21:00
March	19:00 - 22:00	20:00
April	18:00 - 22:00	19:00
May	17:00 - 22:00	19:00
June	17:00 - 22:30	19:00
July	17:00 - 22:30	19:00
August	17:00 - 22:30	19:00
September	18:00 - 00:00	20:00
October	18:00 - 23:00	21:00
November	18:00 - 23:00	21:00
December	19:00 - 22:30	21:00

5.6 DHW consumption profiles

Typical DHW consumption levels for each month in Chile are obtained from [72] (see Figure 5.7). An annual consumption of 25510 L/person, equivalent to 1337 kWh/year, is assumed. The results were interpolated to obtain the consumption in liters for each time step (L_{wsup}) assuming a supply temperature (T_{wsup}) of 45°C, according to the local regulatory framework [73]. DHW consumption profiles were defined based on occupancy status, and it is also assumed that there is no consumption from 0:00 am to 7:00 am (see section 5.4 for occupancy profile descriptions). Table 5.4 summarizes the consumption periods for each household.

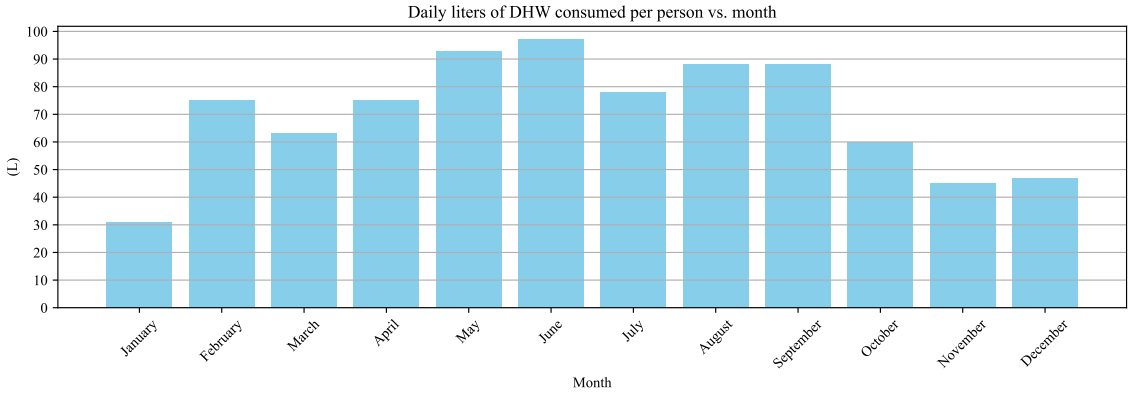

Figure 5.7: DHW average consumption per person in Chile by each month.

Table 5.4: DHW consumption hourly ranges.

Residential Customer	Station	Consumption period	
		Weekday	Weekend
Prosumer 1	Summer	7:00 - 8:00 ; 14:00 - 00:00	7:00 - 00:00
	Winter	7:00 - 00:00	7:00 - 00:00
Prosumer 2	Summer	7:00 - 11:00 ; 19:00 - 00:00	7:00 - 00:00
	Winter	7:00 - 13:00 ; 18:00 - 00:00	7:00 - 00:00
Consumer 1	Summer	7:00 - 10:00 ; 18:00 - 00:00	7:00 - 10:00 ; 20:00 - 00:00
	Winter	7:00 - 8:00 ; 15:00 - 00:00	7:00 - 12:00 ; 18:00 - 00:00
Consumer 2	Summer	7:00 - 8:00 ; 19:00 - 00:00	7:00 - 10:00 ; 20:00 - 00:00
	Winter	7:00 - 8:00 ; 19:00 - 00:00	7:00 - 12:00 ; 18:00 - 00:00

6 | Results from P2P Market Benefit Assessment

A numerical simulation was conducted to analyze the outcomes of the P2P market operation within a residential microgrid, utilizing a 1-hour resolution. The simulations were conducted in Jupyter Notebook with Python 3.10.4, running on macOS Monterey V12.4. The hardware setup includes an Apple M1 chip, 8 GB of RAM, 8-core CPU, 7-core and 8-core GPUs. Figure 6.1 shows schematic diagram of the community microgrid, which consists of two prosumers, two consumers, one aggregator responsible for coordinating the P2P market, and the UG. Thermal loads were not considered in this analysis. The proposed configuration of RCs is presented in Table 7.1.

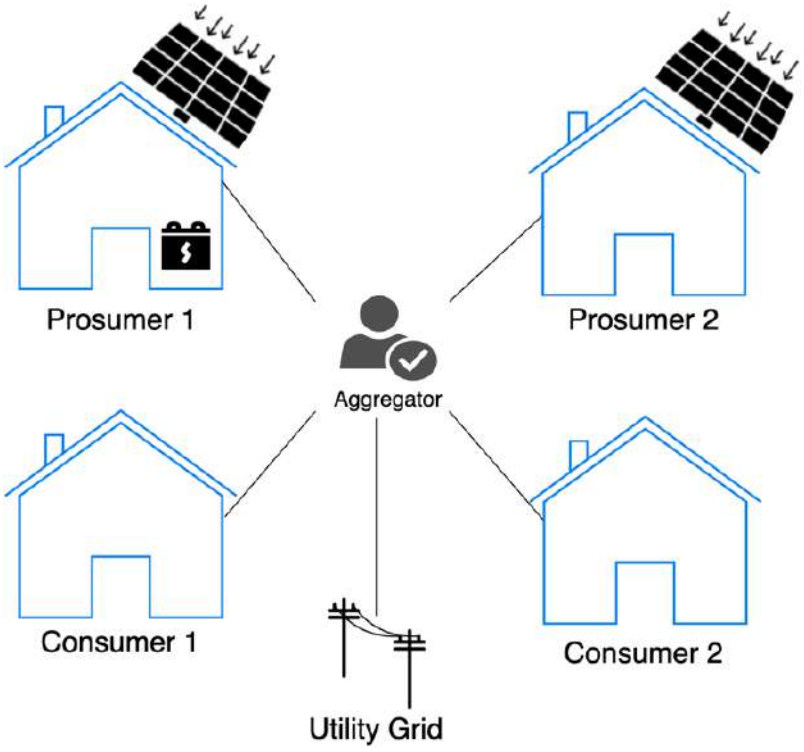

Figure 6.1: Characterization of the participants in the case study.

Table 6.1: Proposed Configuration For RCs.

Parameter	Value				Unit
	P1	P2	C1	C2	
PV installed power	4.92	4.10	0	0	kWp
BESS capacity	10.56	0	0	0	kWh
Annual base demand	3722[a]	3022[b]	3722[a]	3022[b]	kWh/year

[a]Load profile A

[b]Load profile B

6.1 Analysis for P2P market scenario

Sample results are generated for analysis during the period from April 1st to 2nd in the first year of operation. Figure 6.2 displays the results for prosumer 1. Figure 6.2a illustrates the PV generation and electric load profiles. Local generation would experience significant fluctuations, largely influenced by meteorological conditions. Figure 6.2b shows that during high PV generation hours, the BESS consistently would reach its maximum SoC. During nighttime hours, it would be discharged to supply the local load. Figure 6.2c provides insight into the energy transfer dynamics. On April 1st, a portion of PV surpluses would be injected into the AG for trading within the P2P market, while the remainder would be injected into the UG. On April 2nd, PV surpluses would be utilized for recharging the BESS. Power imports from the UG would be null, primarily owing to the self-consumption facilitated by the BESS.

Figure 6.3 shows results for prosumer 2. Figure 6.3a shows the PV generation and electric load profiles. Figure 6.3b reveals a increase in power injections into both the P2P market and the UG compared to prosumer 1, due to the lower load and the absence of a BESS. Self-consumption exclusively would take place during daylight hours, whereas during the nighttime period, there would be power imports from the UG.

Figure 6.4 shows the power imports for consumer 1 from both the P2P market and the UG. Typically, power would be obtained from the P2P market during sunny hours, whereas nighttime would tend to rely on UG power supply. In certain situations, such as at 8:00 am, when there are insufficient offers in the P2P market, a portion of the load would be satisfied by the UG. A similar analysis can be applied to consumer 2.

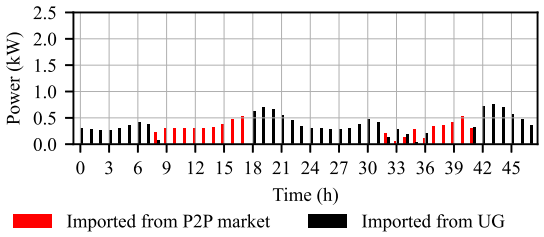

Figure 6.4: Power import profiles from the P2P market and the UG for Consumer 1.

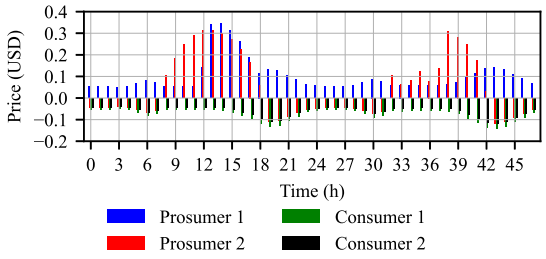

Figure 6.5: Net flows for RCs.

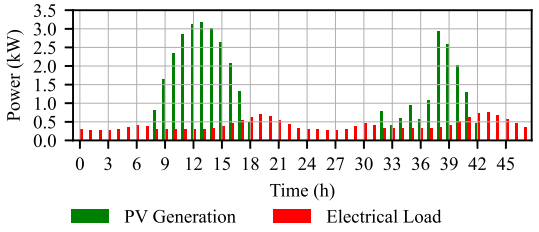

(a)

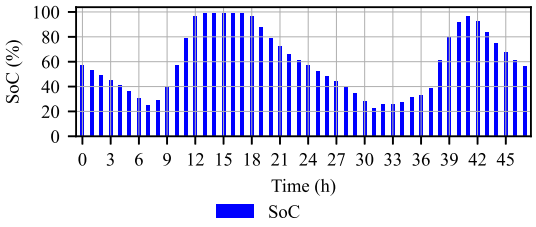

(b)

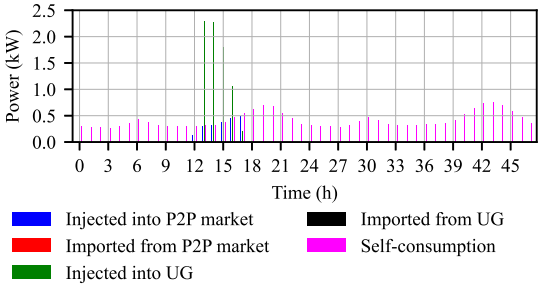

(c)

Figure 6.2: Graphical results for prosumer 1 include (a) PV generation and electrical load profiles, (b) SoC status profile, (c) profiles of self-consumption and power fluxes involving the P2P market and the UG.

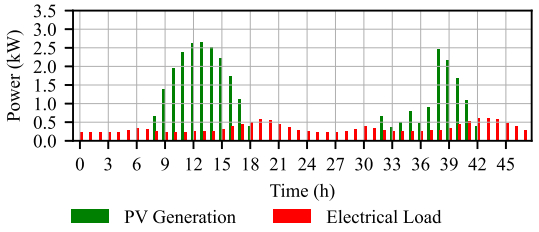

(a)

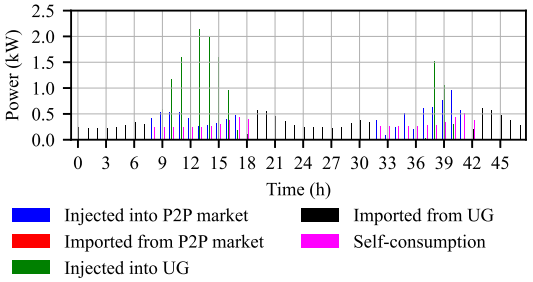

(b)

Figure 6.3: Graphical results for prosumer 2 include (a) PV generation and electrical load profiles, (b) profiles of self-consumption and power fluxes involving the P2P market and the UG.

Figure 6.5 illustrates the net flows for the RCs. Prosumer 1 could generate profits on both days through a combination of self-consumption and power injections into both the P2P market and the UG. Prosumer 2 also could achieve profits by means of self-consumption and by injecting surplus power into the AG during sunny hours. Both consumers would incur expenses for the energy they consume throughout the day.

Figure 6.6 shows results for AG. Figure 6.6a shows the power flows within the P2P market and between the community and the UG. The power flows managed within the P2P market would remain relatively low, peaking at 1 kW, in contrast to the higher power flows managed with the UG, which could reach up to 4.5 kW. However, increased community consumption during periods of surplus injection into the UG would likely boost power transactions in P2P market. Figure 6.6b shows P2P market energy transaction costs and FR incentives. During nighttime periods, FR incentives would be common due to power imports from the UG, contributing to grid frequency stabilization. Payments to AG for energy sales within the P2P market are shown, as well as payments to the community for acquiring PV surpluses, which would be subsequently resold in the P2P market. Transactions between the community and the UG would be excluded as they have no impact on AG's net flow. Figure 6.6c illustrates that AG would earn a modest profit from both P2P transaction coordination and FR incentives. Nevertheless, the potential for greater revenue would exist by incorporating additional RCs and facilitating a higher amount of P2P market transactions.

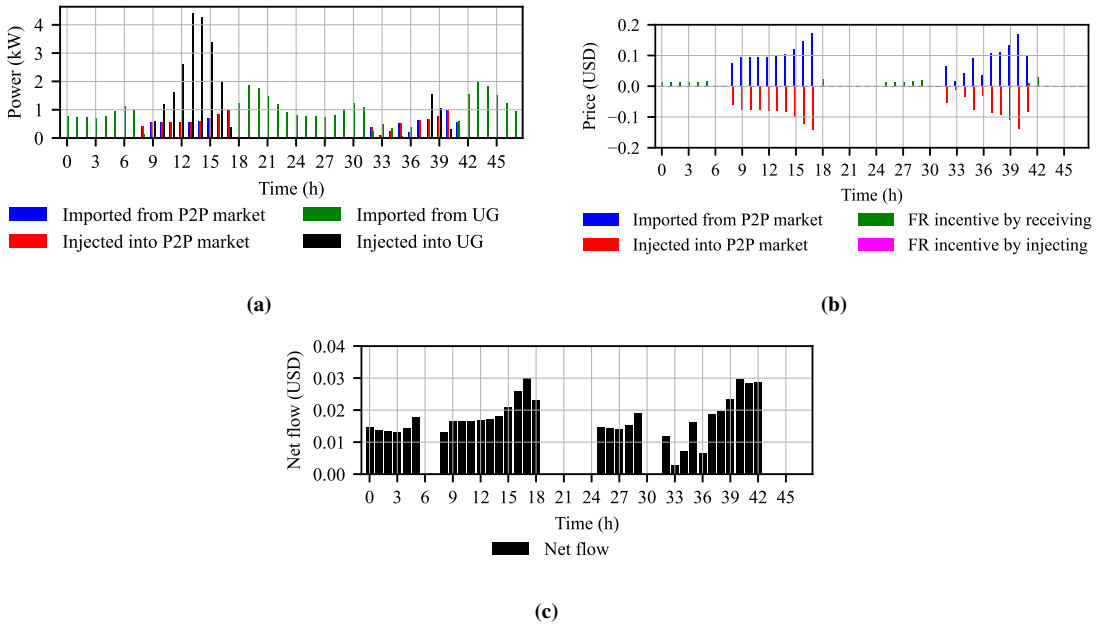

Figure 6.6: Graphical results for AG include (a) power fluxes within the P2P market coordinated by the AG, (b) energy transaction costs and FR incentives for the AG, (c) net flow for the AG.

6.2 Comparison with/without P2P market scenarios

Table 6.2 summarizes the daily electricity bills for RCs, as well as the incomes for the AG and the UG, based on P2P market availability. For Prosumer 1 (P1), the maximum daily electricity bill would remain unaffected, with only a minor impact on the average daily bill. This is primarily due to limited engagement in the P2P market since a significant portion of surplus PV power is stored in the BESS. Benefits would be derived primarily when the BESS reaches full capacity, enabling the injection of surplus PV power into the AG.

However, such occurrences would be infrequent, typically confined to the summer months. Consequently, the minimum billing rate, representing the maximum daily income, would experience a reduction. Prosumer 2 (P2) would obtain more significant benefits from the P2P market, leading to reductions in both the minimum and average daily bills. It actively would participate in the P2P market, taking advantage of the prioritized allocation of PV surplus for trading. The maximum billing rate would remain unaffected as it typically occurs on days with limited solar irradiation, preventing the generation of PV surplus for injection. Consumer 1 (C1) and Consumer 2 (C2) would obtain reductions in their minimum and average daily bills, owing to their opportunity to buy energy at a lower cost within the P2P market. However, the maximum bills would be unaffected, as they would tend to occur when the P2P market is closed, unlike the minimum rates which would be prevalent during the summer months when surplus energy trading is more extensive. In scenarios where neither a P2P market nor participation in FR occurs, the AG would not generate any income. In contrast, in scenarios involving FR and P2P market, the AG red would achieve an average daily income of 0.27 USD. Also, the average daily income for the UG would decrease due to reduced energy sales to the community with the P2P market implementation. However, potential cost savings from avoiding infrastructure damage through FR should be considered, although accurate estimation would require real data from the UG. The financial results for P2P market participants will also depend on the number of RCs to be considered and PV penetration in the microgrid.

Table 6.2: Daily Electricity Bills For RCs And Daily Incomes For The AG And The UG, Under Each Scenario.

Parameter		Value						Unit
Scenario	Net flow	P1	P2	C1	C2	AG	UG	
No P2P	max	1.86	1.51	2.25	1.83	0.00	7.79	USD/day
	min	-3.15	-1.85	1.66	1.35	0.00	0.51	
	avg	-1.67	-0.80	1.92	1.56	0.00	3.14	
With P2P	max	1.86	1.51	2.25	1.83	0.43	7.69	
	min	-3.18	-1.96	1.62	1.31	0.08	-0.05	
	avg	-1.68	-0.90	1.89	1.53	0.27	2.63	

Table 6.3 presents an annual electricity bill estimate for each RC in three distinct scenarios: No PV & No P2P market, PV & No P2P market, and PV & P2P market. In the first scenario, all RCs are categorized as consumers. In the second scenario, prosumers can fully offset their annual electricity bills through PV systems. As per local regulations, they are eligible for reimbursement from the UG at the end of the year for the surplus injections values that exceed their annual bills. In the third scenario, where a P2P market is introduced, P1 and P2 could potentially enhance their profits, resulting in increased reimbursements of 13 USD and 49 USD, respectively. Conversely, C1 and C2 could witness marginal reductions in their annual bills, approximately 1.71% and 1.75%, respectively, by participating in the P2P market. However, increased participation of prosumers within the community would likely lead to a greater supply of power available in the P2P market, thereby enabling more significant reductions in bills for consumers.

Table 6.4: Financial Comparison For Prosumers.

Parameter		Value		Unit
Scenario	Variable	P1	P2	
No P2P market	NPV	-6800	1922	USD
	IRR	2.3	16.6	%
	Payback	18.7	5.8	years
With P2P market	NPV	-6790	2276	USD
	IRR	2.3	17.8	%
	Payback	18.7	5.4	years

Table 6.3: Average Annual Electricity Bills For RCs.

Scenario	Value				Unit
	P1	P2	C1	C2	
No PV & No P2P	701	569	701	569	USD/year
PV & No P2P	-2	-33	701	569	
PV & P2P	-15	-82	689	559	

A profitability analysis of DERs projects for prosumers has been conducted. The initial investment for P1 is 13,333 USD plus the replacement of the BESS after 12 years for $9,178 USD, whereas the initial investment for P2 is $3,663 USD. Table 6.4 provides insights into the Net Present Value (NPV), IRR, and Payback period, all projected over a 25-year horizon with a discount rate of 10%. These calculations assume fixed P2P market and UG electricity prices over the years. P1 would exhibit minimal variations in results when the P2P market implementation is considered, mainly because of their limited involvement. In contrast, P2, with more active participation, would experience a 1.2% increase in IRR and a 0.4-year reduction in payback.

6.3 Sensitivity Analysis

A sensitivity analysis was conducted to assess the annual income variations for RCs, the AG, and the UG, in addition to evaluating the IRRs for DERs projects. It involved varying the installed PV power capacities for P1 (ranging from 1.64 kWp to 8.20 kWp) and P2 (ranging from 0.82 kWp to 7.38 kWp), as well as adjusting the BESS capacity for P1 (ranging from 6.34 kWh to 14.78 kWh).

Figure 6.7 shows that annual income of P1 would rise with an increase in its installed PV power. This occurs because a greater amount of PV surplus would be generated to be sold. Additionally, having a larger BESS capacity would result in a higher self-consumption rate; however, it also would lead to increased standby losses. Consequently, another criterion arises to determine the optimal BESS capacity, where the highest annual income would be achieved with 10.56 kWh. Conversely, P1 could attain a higher annual income if the installed PV power of P2 is reduced. This dynamic arises from competitive interactions within the P2P market. When P2 injects fewer surplus amounts, P1 could sell a larger surplus volume in the P2P market, thus enhancing their profits. With a 3.3 kWp installed, P1's annual electricity bill would be fully covered. Figure 6.8 shows that the annual income of P2 would increase significantly as its installed PV power increases, mirroring the trend observed in the case of P1. Annual income would exhibit insensitivity to the installed PV power and BESS capacity of P1. Similar to P1, an installed capacity of 2.5 kWp would fully

offsets the annual electricity bill. Figure 6.9 shows that as the installed PV capacity of prosumers increases, the reduction in electricity bills for C1 would be higher. This is attributed to a greater availability of PV surpluses to be bought in the P2P market. For the same reason, it is observed that with a lower BESS capacity of P1, a greater benefit would be generated for C1. The same trend applies to C2.

Figure 6.10 shows that as the installed PV capacity of P2 increases and the BESS capacity of P1 decreases, AG's annual income would rise, due to the generation of larger PV surpluses, leading to increased energy transactions within the P2P market. However, an optimal point emerges based on the installed PV power of P1, with 3.3 kWp resulting in the highest annual income. This would occur because, when P1 installs less PV power, it would generate a higher demand within the P2P market, leading to a greater number of transactions that benefit the AG.

Figure 6.11 shows that P1 would achieve a more favorable IRR as its installed PV power increases, due to increased surplus sales within the P2P market. Also, a reduction in P1's BESS capacity would result in a higher IRR, owing to the lower initial investment cost of BESS. The installed PV power of P2 does not significantly impact P1's IRR. Figure 6.12 demonstrates that P2 would enhance its IRR when P1 decreases its installed PV power and augments its BESS capacity. This outcome is influenced by competitive dynamics within the P2P market. Moreover, P2 benefits from increasing its installed PV power up to an optimal point. The highest IRR could be achieved when P2 installs 2.5 kWp, primarily because a higher installed PV power entails a greater investment, and also due to the P2P market becoming saturated with surplus offers, which arises due to low demand.

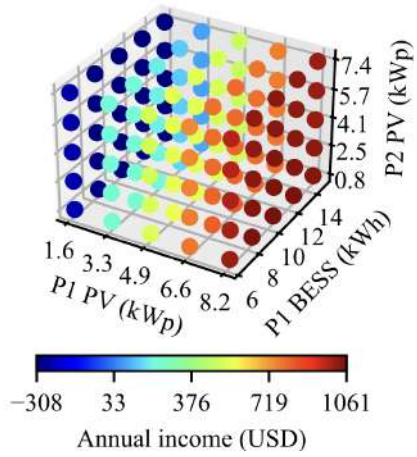

Figure 6.7: Sensitivity analysis of annual income for P1.

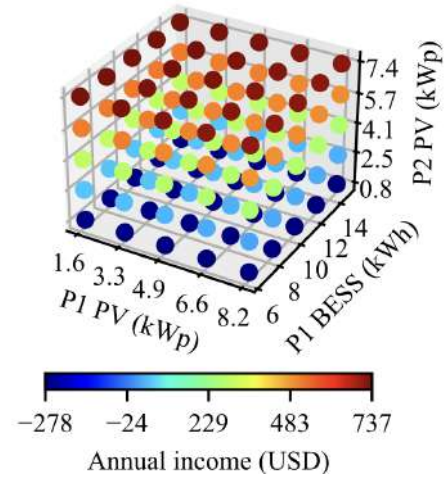

Figure 6.8: Sensitivity analysis of annual income for P2.

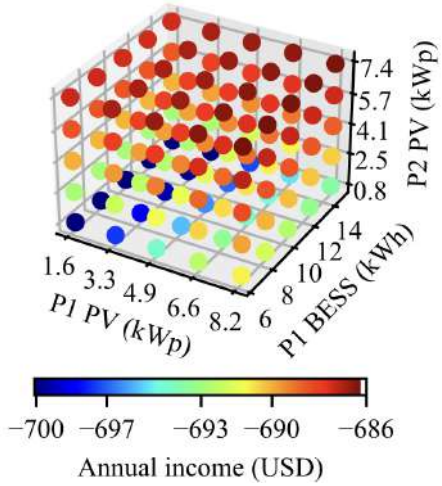

Figure 6.9: Sensitivity analysis of annual income for C1.

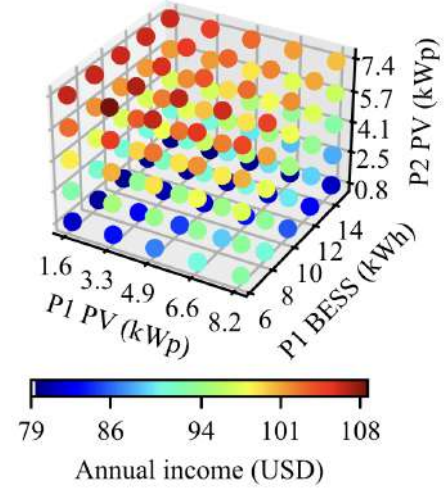

Figure 6.10: Sensitivity analysis of AG annual income.

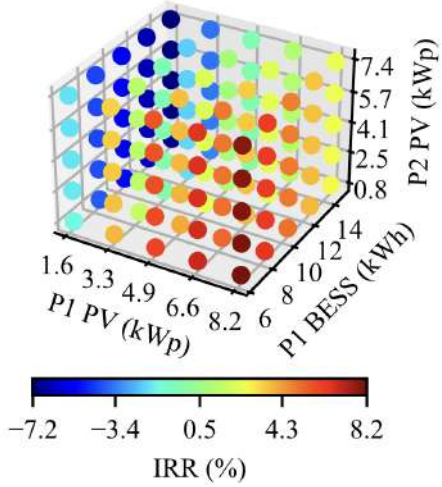

Figure 6.11: Sensitivity analysis of IRR for P1.

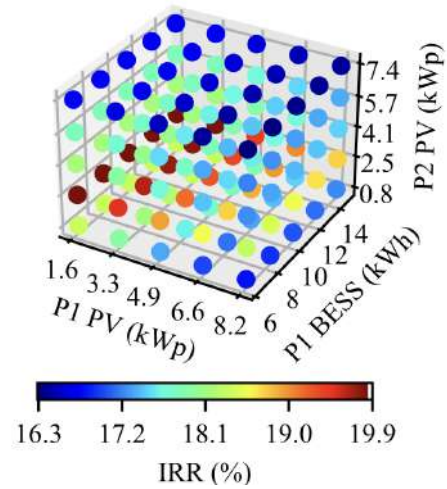

Figure 6.12: Sensitivity analysis of IRR for P2.

6.4 Conclusions

This study presented a sensitivity analysis for a local PV energy trading within a community microgrid to highlight the potential positive impacts and support the development of a new regulations for Chile, which may facilitate the market penetration of distributed generation based on PV systems.

The proposed architecture has been evaluated for a small microgrid consists of two prosumers, two consumers, one aggregator, and the utility grid, but the analysis and results may be extrapolated to a greater microgrid. The prosumers were engaged in DERs projects, including PV systems with or without BESS. A comprehensive daily and annual financial comparisons were conducted, comparing scenarios with and without a P2P market. Prosumers with PV systems, both with and without BESS, could experience an increase in their average daily income, while consumers could observe a reduction in their average daily electricity bills.

The results show that prosumer with PV system and BESS has a reduced benefit because most of its generated surpluses are stored, resulting in minimal participation in the P2P market. Conversely, prosumer with PV system without BESS would prioritize selling surplus PV energy in the P2P market, leading to increased participation, showing a rise in IRR, and a reduction in payback. With local energy trading, the UG would decrease its purchase of surplus energy injected from the community. Thus, DERs projects and P2P markets would offer a cost-effective alternative to address the urgent local need for increased storage capacity and tackle current operational challenges within the UG. Nonetheless, it would experience a decline in its daily income owing to reduced energy sales to the community, which has a systemic benefit by reducing electrical infrastructure damage; however, this economic savings needs to be adequately estimated.

A sensitivity analysis was conducted on the annual income of participants, as well as on the IRRs of DERs projects. Prosumers could achieve higher annual income by installing higher PV capacities and optimizing BESS capacity. Regarding their IRRs, there would seem to be a competitive dynamic in surplus sales within the P2P market among prosumers, where the PV capacity and storage capacity of one would interfere with the IRRs obtained by the other. For consumers, their benefits would increase as the supply of surpluses in the P2P market increases, namely when installed PV capacity increases and prosumers' B SS capacity decreases. The AG would also benefit by increasing the volume of energy transactions within the P2P market, with optimal points identified between surplus supply and energy demand.

Future work aims to investigate individual return/revenue with large number of participants in the local energy market. Furthermore, extend the proposed model to adapt different regions of Chile with different service providers.

7 | Results for Smart Thermal Load Management

A numerical simulation was conducted to analyze the outcomes of the P2P market operation under smart thermal load management within a residential microgrid, utilizing a 6-minutes time step. The simulations were conducted in Jupyter Notebook with Python 3.10.4. Figure 7.1 shows schematic diagram of the community microgrid, which consists of two prosumers, two consumers, one aggregator responsible for coordinating the P2P market, and the UG. The proposed configuration of RCs is presented in Table 7.1, where all RCs maintain AC systems, DHW tanks, and different annual demand profiles.

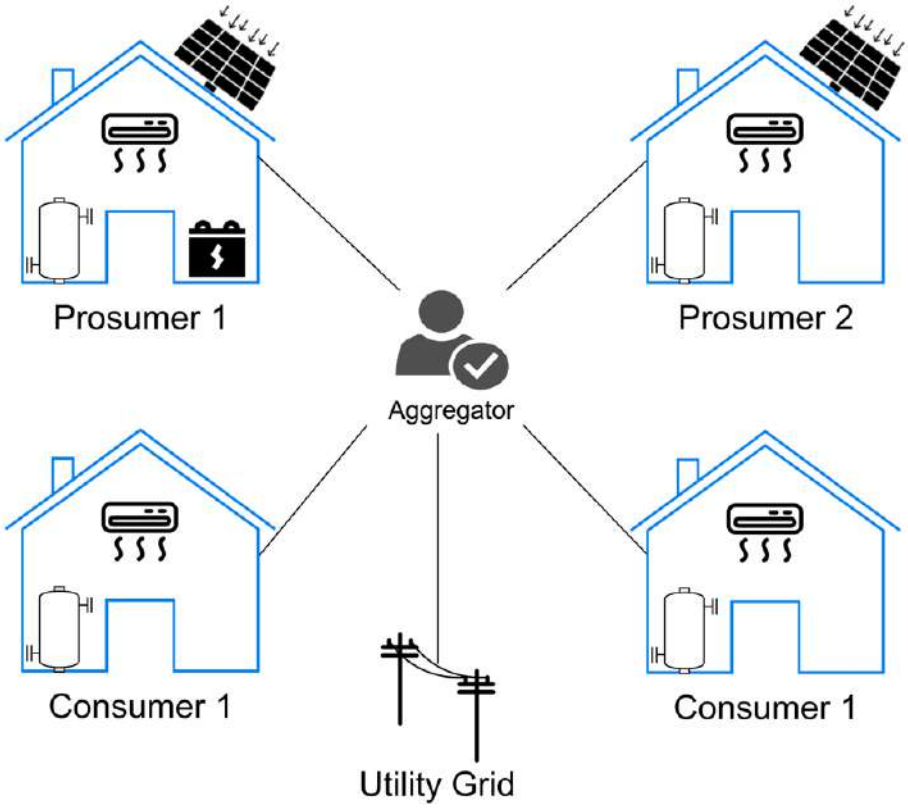

Figure 7.1: Characterization of the participants in the case study.

Table 7.1: Proposed Configuration For RCs.

Parameter	Value				Unit
	P1	P2	C1	C2	
PV installed power	6.56	5.74	0	0	kWp
BESS capacity	12	0	0	0	kWh
DHW tank capacity	200	200	200	200	L
AC system rated power	1.7	1.7	1.7	1.7	kW
Base annual load	3722[a]	3022[b]	3722[a]	3022[b]	kWh/year

[a]Load profile A; [b]Load profile B

7.1 DHW Self Technique Sample

Figure 7.2 shows a sample comparison between a conventional method and the DHW Self method for controlling the DHW tank. The results correspond to P2, during summer days of January 11 and 12, with a rated power of 2kW for the conventional method and a variable power between 0 and 3.5 kW for the DHW Self method. The DHW Self method demands power within the PV generation bell through self-consumption, avoiding consumption from the UG during peak hours, and allowing greater demand flexibility. Conversely, the conventional method opts for a single heating period from the minimum to the maximum operating temperature, leading to nighttime consumption.

Figure 7.3 shows the comparison of the internal temperature behavior for both methods. It is observed that in the conventional method, the tank heats the water when it reaches the minimum operating temperature of 50°C, up to a maximum of 80°C. On the other hand, the DHW Self method heats according to the availability of PV surpluses, so it tends to maintain a high internal temperature during the summer and a low temperature during the winter.

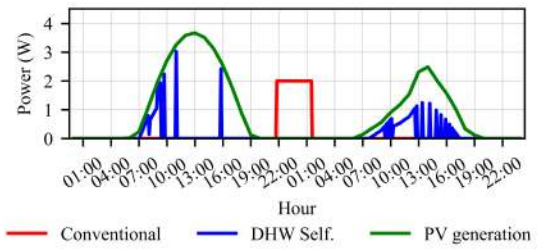

Figure 7.2: Sample comparison between conventional and DHW Self methods.

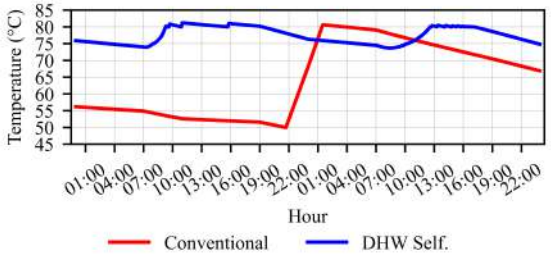

Figure 7.3: Behavior of internal temperature for the Conventional and DHW Self methods.

Figures 7.4 and 7.5 show the power fluxes for the conventional DHW method and DHW Self, respectively. Figure 7.4 shows that between 9:40pm and 1:30am, there is a significant power import from the UG, corresponding to the consumption for water heating. Thus, the conventional method would not optimally utilize local resources, also requiring energy from the UG during critical and nocturnal periods. On the other hand, Figure 7.5 shows that with the DHW Self method, the self-consumption curve and the energy injected into the P2P market increase considerably during high PV generation hours, while injections of surpluses to

the UG and consumption during critical periods are significantly reduced.

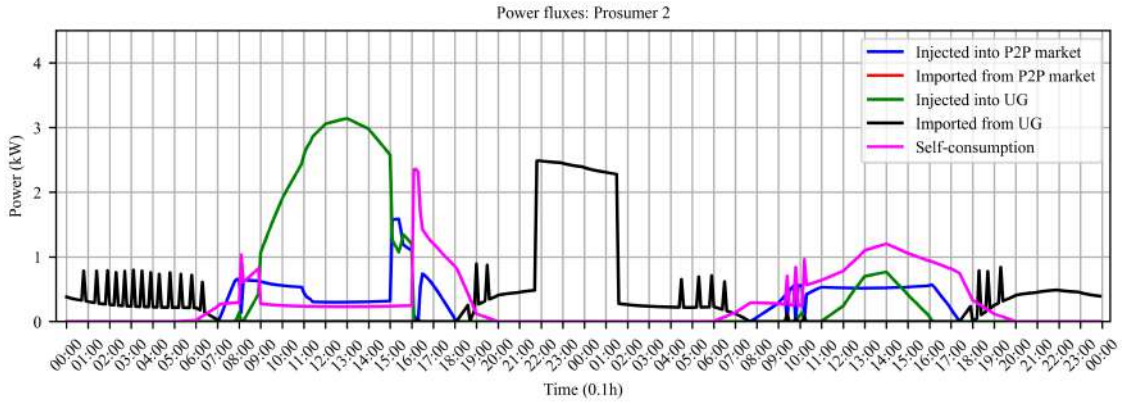

Figure 7.4: Power fluxes for P2 in conventional DHW method.

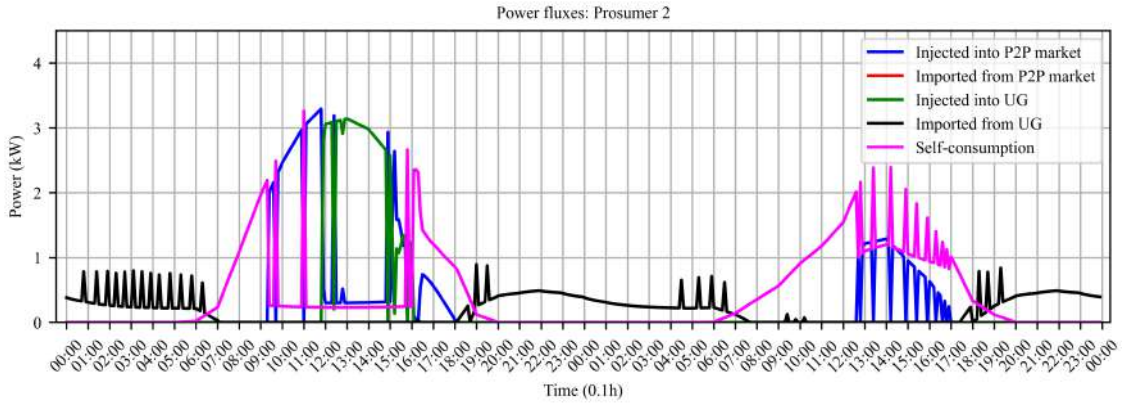

Figure 7.5: Power fluxes for P2 in DHW Self method.

7.2 AC Self Technique Samples

7.2.1 Inverter AC System Assessment

7.2.1.1 Overheating Sample

Figure 7.6 shows a sample of the overheating technique during a winter day on June 17, where the set point temperature was increased by 7°C. It can be observed that the temperature of the thermal mass of the roof and walls is increased by approximately 1°C, which favors savings in heating consumption during the subsequent hours, taking advantage of the building's thermal inertia. Similarly, consumers have the option to apply this technique by purchasing surplus from the P2P market at a special price.

Figure 7.7 shows the thermal loads for the conventional AC method and AC Self. With the conventional method heats during nighttime hours, and a cooling cycle appears during hours of high solar irradiation, in order to mainly counteract heat gains from solar infiltration and maintain the set point temperature at 22°C. On the other hand, the AC Self method maintains a similar behavior during nighttime hours; however, by

increasing the set point temperature during hours of high solar irradiation, the cooling cycle is avoided thanks to solar heat gain, represented as a parabola, thus reducing the energy consumption of the AC system and reducing total consumption during subsequent critical consumption hours. Figures 7.8 and 7.9 summarize the power fluxes for the conventional method and AC Self with overheating, respectively, for the prosumer with BESS. Comparing both figures, it can be observed that overheating allows for a reduction in the energy consumption of the AC system, resulting in an increase in the injections to the UG curve. Also, during critical consumption hours, fluctuations in the power demanded by the AC Self system are observed, because the system requires a minimum operating power, and therefore, when heat input is required that demands an electrical power lower than the minimum operating power to maintain the set point temperature, the inverter AC turns off, generating these power peaks. However, this does not affect the energy imported from the UG, since P1 presents self-consumption during this critical period thanks to its BESS.

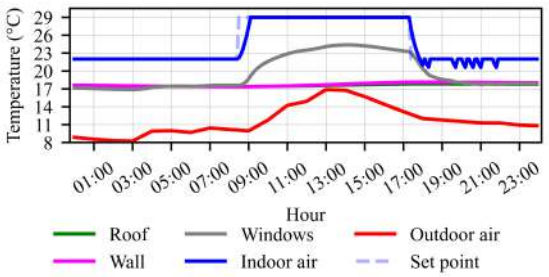

Figure 7.6: Overheating technique sample.

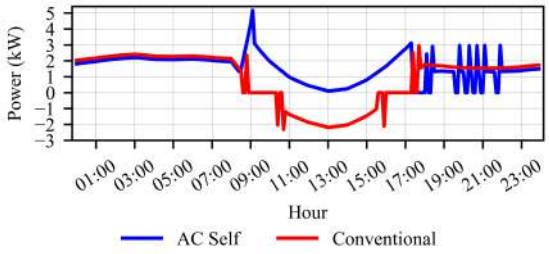

Figure 7.7: Behavior of thermal loads for the Conventional and AC Self with overheating methods.

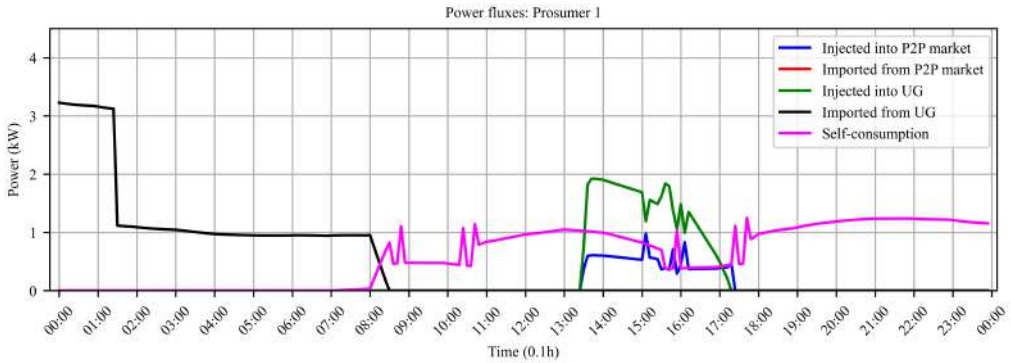

Figure 7.8: Power fluxes for P1 in conventional AC method during June 17.

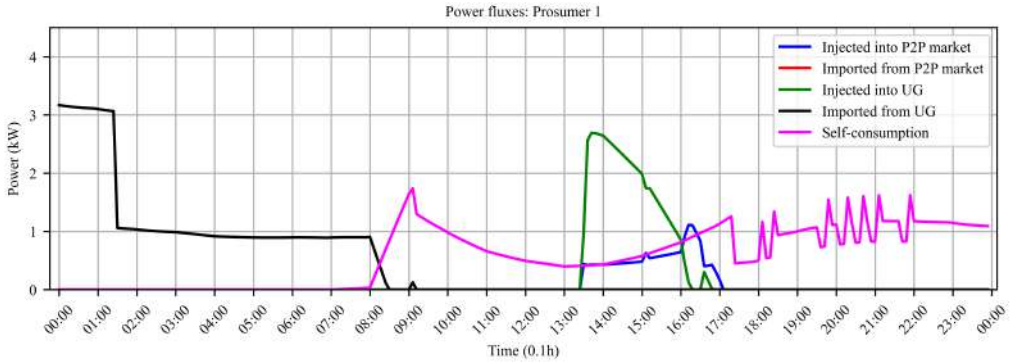

Figure 7.9: Power fluxes for P1 in AC Self method for overheating during June 17.

7.2.1.2 Overcooling Sample

Figure 7.10 shows a sample of the overcooling technique applied during a summer day on January 20, where the set point temperature was decreased by 7°C. It manages to counteract internal heat gains and solar irradiation; however, the temperature of the walls and ceiling remains practically constant.

Figure 7.11 compares the behavior of thermal loads for the conventional and AC Self methods with overcooling. During hours of high solar irradiation, the AC Self method requires higher energy consumption because it has a lower set point temperature, resulting in a greater difference between the external ambient temperature and the internal temperature, leading to increased heat transfer to the interior, which must be countered by the cooling cycle. Additionally, during the subsequent hours, the AC Self method presents higher consumption corresponding to small heating cycles, due to the decrease in the external ambient temperature. In contrast, the conventional method, by maintaining a higher set point temperature during the day, allows the building's thermal mass to store a greater amount of thermal energy, resulting in less AC system consumption during nighttime hours.

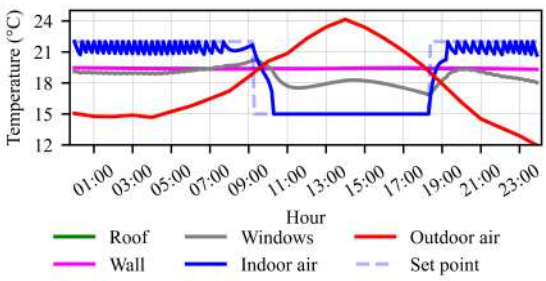

Figure 7.10: Overcooling technique sample.

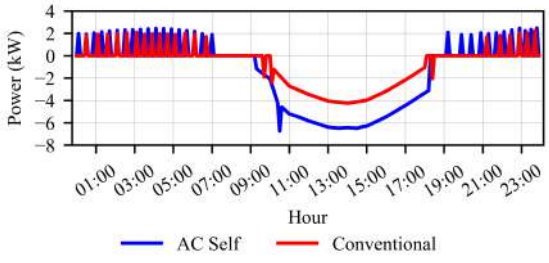

Figure 7.11: Behavior of thermal loads for the Conventional and AC Self with overcooling methods.

Figures 7.12 and 7.13 summarize the power fluxes for the conventional method and AC Self with overcooling, respectively, for the prosumer without BESS. Figure 7.12 shows the self-consumption curve throughout the day, mainly corresponding to the power demand of the AC system. Additionally, periods of high power injected into the P2P market and the UG are observed, respectively. On the other hand, Figure 7.13 shows that implementing overcooling drastically increases the self-consumption curve, while

reducing the power injection curves into the P2P market and the UG, respectively. However, during the critical consumption period, the power from the UG increases both in quantity and in the maximum power demanded from the UG.

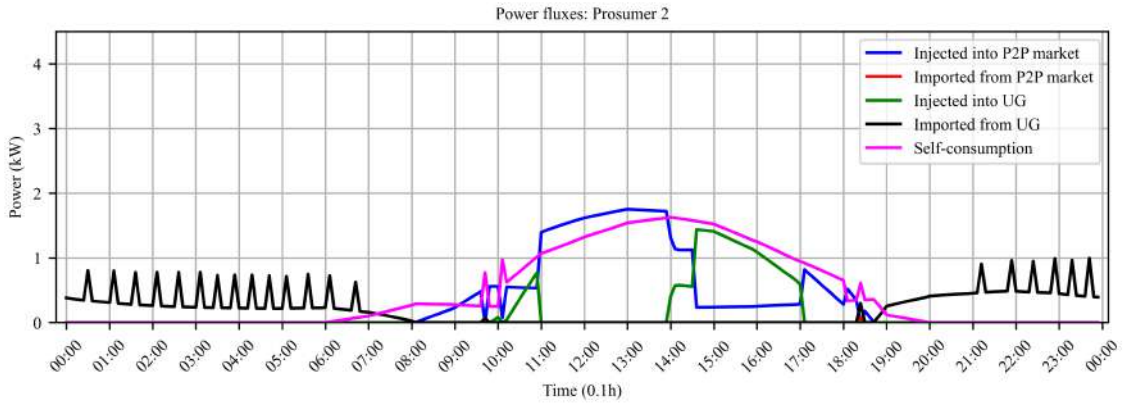

Figure 7.12: Power fluxes for P2 in conventional AC method during January 20.

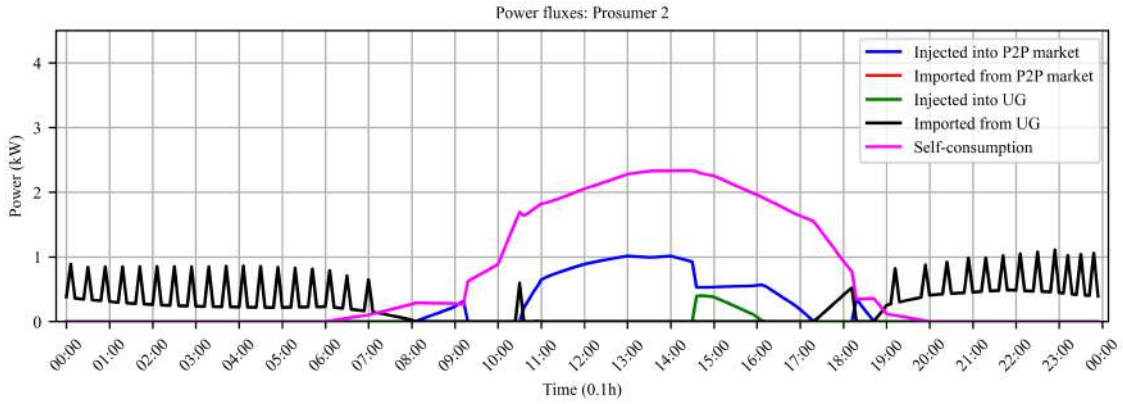

Figure 7.13: Power fluxes for P2 in AC Self method for overcooling during January 20.

Despite this technique benefiting from a higher availability of PV surpluses during the summer, allowing for more frequent overcooling cycles, it results in higher energy consumption and reduces income for prosumers due to a lower amount of injections into both the P2P market and the UG. Additionally, compared to the overheating method, AC systems show lower efficiencies in cooling mode, and the removal of sensible heat from the interior corresponds to only 75% of the total heat extracted, requiring a greater amount of energy to change the internal temperature.

7.2.1.3 Thermal Comfort Assessment Sample

Figure 7.14 depicts the evaluation of PMV for the previously analyzed samples. In both cases, the PMV remains mostly within the optimal comfort range between [-0.5, 0.5], as frequently utilized by standards [64]. The implementation of AC Self. techniques would not significantly impact the thermal comfort of the occupants, and the change of ±7°C would be the maximum recommended value without having to change their thermal preferences.

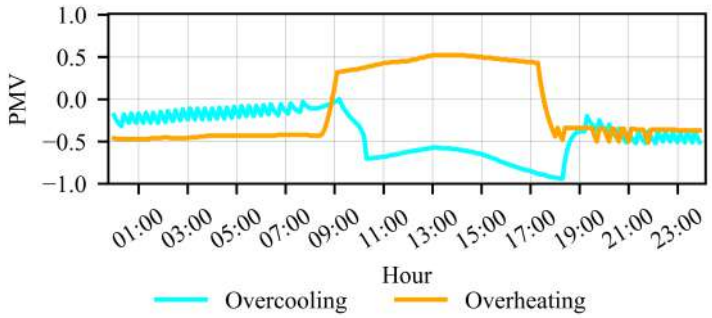

Figure 7.14: PMV results from samples for inverter AC.

7.2.2 Fixed-speed AC System Assessment

Similarly to the analysis conducted for the inverter AC system, an analysis is carried out using a fixed-speed AC system, which has a fixed nominal working power.

7.2.2.1 Overheating Sample

Figure 7.15 shows the behavior of internal temperatures under the overheating technique. During normal mode, the operating range of the internal temperature is between 20 and 24°C, while in overheating mode, the range shifts to between 27 and 31°C. There is a slight increase in the temperatures of the walls and roof, which helps sightly reduce the number of heating cycles in the subsequent hours. This is further evidenced by Figure 7.16, where in conventional mode, there are more heating cycles during the critical consumption period and during nighttime hours. Additionally, the conventional mode has to apply cooling cycles during hours of solar irradiation, because it has a range of operation of lower temperatures.

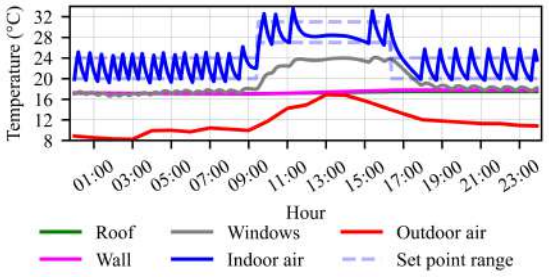

Figure 7.15: Overheating technique sample with fixed speed AC.

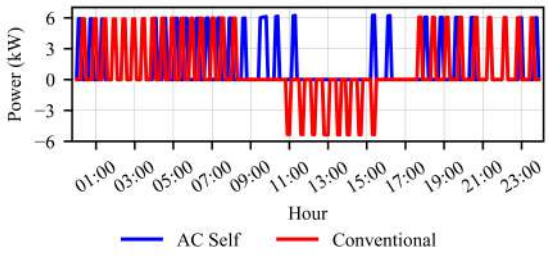

Figure 7.16: Behavior of thermal loads for the Conventional and AC Self with overheating methods, using fixed speed AC.

Figures 7.17 and 7.18 summarize the power fluxes for the conventional method and AC Self with overheating, respectively. Comparing the results, it is observed that the overheating method allows for a reduction in consumption during hours of high solar irradiation, resulting in a higher power injected into the UG. Also, with the AC Self method, there is one less heating cycle during the critical consumption period.

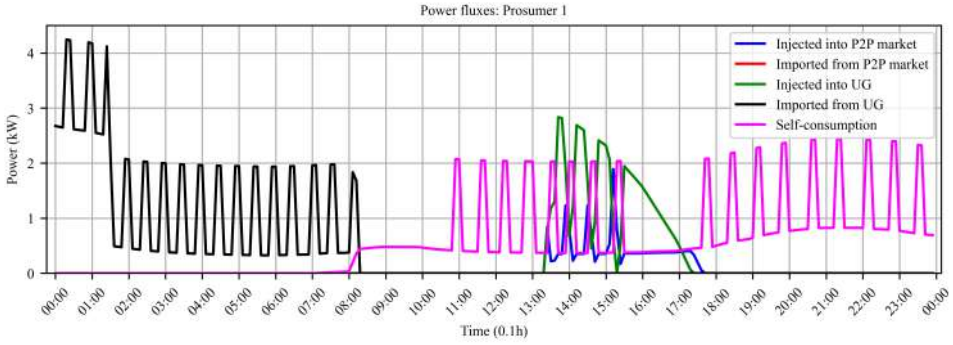

Figure 7.17: Power fluxes for P1 in conventional AC method during January 20, using fixed speed AC.

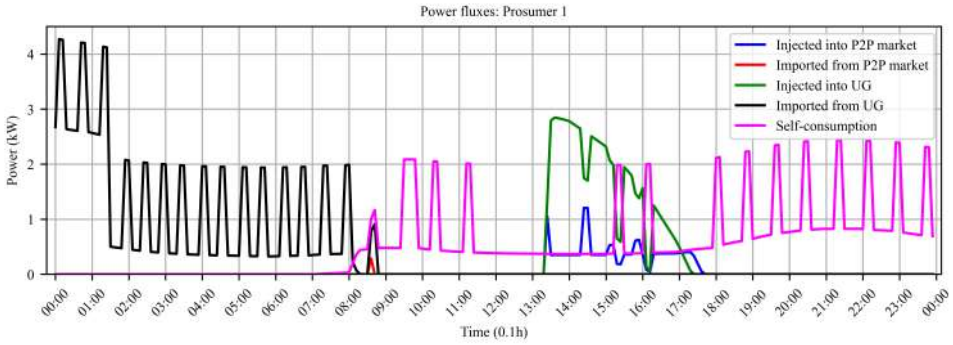

Figure 7.18: Power fluxes for P1 in AC Self method for overheating during January 20, using fixed speed AC.

7.2.2.2 Overcooling Sample

Figure 7.19 shows the behavior of internal temperatures under the overcooling technique. During overcooling mode, the range shifts to between 13 and 17°C. It is observed that unlike an inverter AC, the power of the fixed-speed AC system is not sufficient to cover the overcooling demand, so it would be necessary to install a larger AC system, which would involve higher investment costs and lower energy efficiency. On the other hand, an advantage of conventional AC system control is that the temperature operating range allows for flexibility in operation, allowing for periods of shutdown when the internal temperature fluctuates within the acceptable range. This is observed between approximately 00:00 and 10:00 am, where the AC system did not need to be turned on to control the temperature, leading to significant energy savings compared to an inverter AC, which seeks to maintain a fixed operating temperature. Thus, it is established that the wider the temperature operating range, the greater the potential savings, taking advantage of the flexibility in AC system control.

Figure 7.20 shows the thermal loads associated with the conventional method and the overcooling method. A similar behavior is observed, however AC Self presents a single cooling cycle during the day, avoiding stops and starts of the AC system.

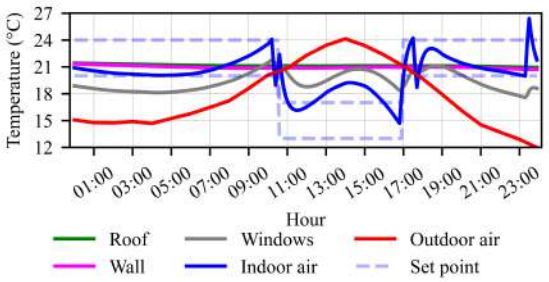

Figure 7.19: Overcooling technique sample with fixed speed AC.

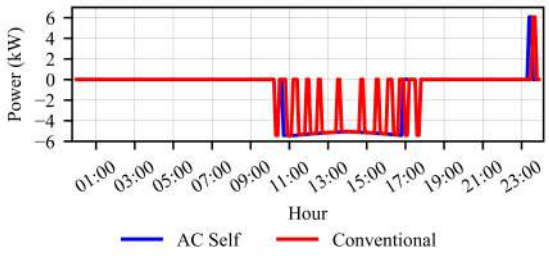

Figure 7.20: Behavior of thermal loads for the Conventional and AC Self with overcooling methods, using fixed speed AC.

Figures 7.21 and 7.22 summarize the power fluxes for the conventional method and AC Self with overcooling, respectively. The AC Self method allows for reducing the peaks of power injected into the grid during hours of high irradiation by increasing self-consumption of surpluses.

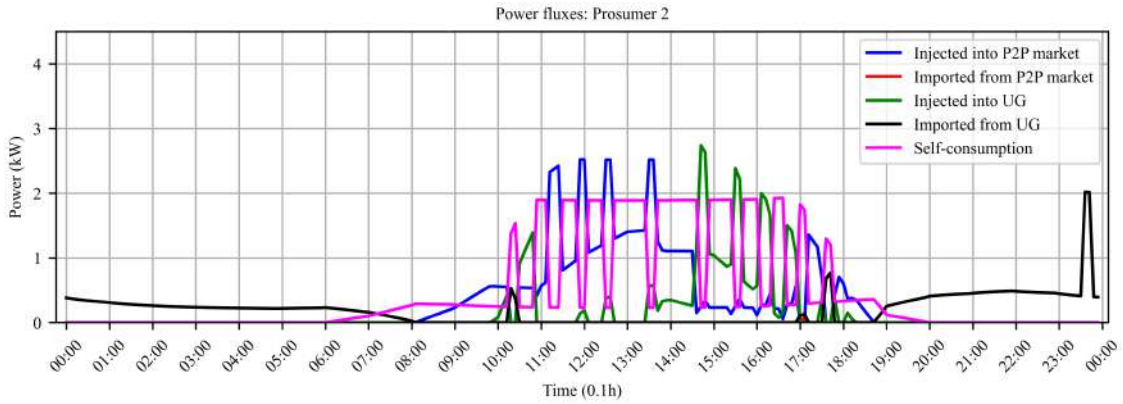

Figure 7.21: Power fluxes for P2 in conventional AC method during June 17, using fixed speed AC.

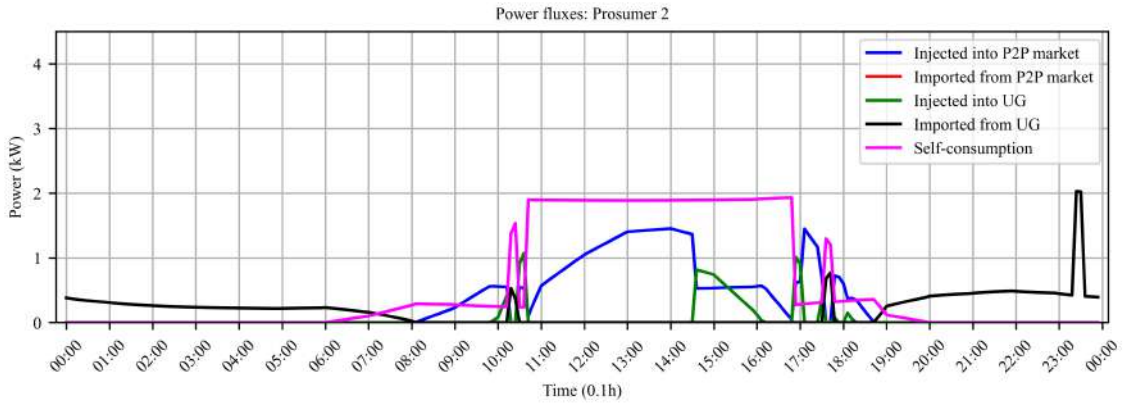

Figure 7.22: Power fluxes for P2 in AC Self method for overcooling during June 17, using fixed speed AC.

7.2.2.3 Thermal Comfort Assessment Sample

Figure 7.23 depicts the evaluation of PMV for the previously analyzed samples. During normal operation and the overcooling period, the PMV tends to fluctuate within the optimal comfort range between [-0.5, 0.5]. However, during overheating, it reaches values close to 1, so occupants could perceive a slight sensation of warmth at times. Nevertheless, the index remains within acceptable neutral levels of thermal comfort.

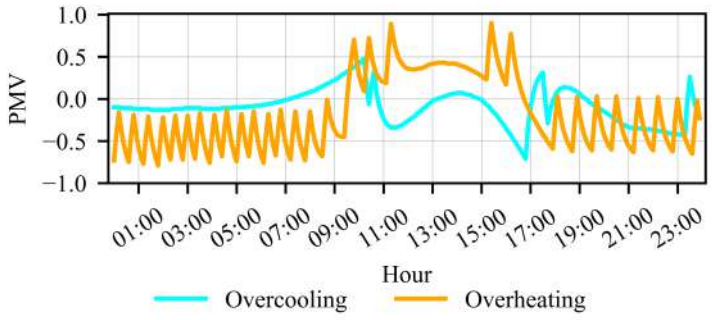

Figure 7.23: PMV results from samples for fixed speed AC.

7.3 Models Comparison with Inverter AC System

To compare the proposed smart thermal load management methods, five scenarios were evaluated: (1) Base Case: No P2P market with AC & DHW, (2) Conventional case: AC & DHW (3) AC Self (overcooling and overheating) & DHW, (4) AC Self (only overheating) & DHW, (5) AC & DHW Self and (6) AC Self (only overheating) & DHW Self. Key indicators such as the annual bills of the RCs, community annual cost, SCR, SSR, and energy imported from the UG during critical periods were analyzed. Table 7.8 summarizes the results obtained.

Table 7.2: Smart thermal load management scenarios comparison for inverter AC system.

Metric	Part.	(1) No P2P	(2) Conv.	(3) AC Self	(4) AC Self (overheating)	(5) DHW Self	(6) DHW Self + AC Self (overheating)	Unit
Annual bills	P1	310	289	376	259	245	209	USD
	P2	326	253	322	250	162	142	
	C1	1275	1256	1232	1231	1230	1242	
	C2	1100	1088	1090	1087	1062	1073	
	CM	3012	2886	3020	2828	2700	2665	
SCR	CM	57.1	74.4	76.9	72.7	91.9	90.6	%
SSR	CM	27.0	35.9	36.1	35.5	44.8	44.8	%
Energy from UG (critical periods)	CM	5354	5313	5358	5284	4431	4438	kWh/ year

CM: Community

When comparing scenarios (1) and (2), it is observed that implementing a P2P market leads to a reduction in electricity bills for the RCs, as was obtained in Section 6. Additionally, the SCR and SSR indicators increase considerably, thanks to the local surpluses being utilized for trading with consumers. However, the implementation of the P2P market does not solve the issue of energy imports from the UG during critical periods, as the reduction is negligible.

Comparing with case (2), the (3) AC Self method leads to an increase in the annual bills of prosumers, whereas employing (4) AC Self with only overheating results in a reduction of these costs. This highlights the inviability of the overcooling technique in this particular case study, as it escalates the energy consumption of AC system in order to counterbalance internal heat gains. Consequently, prosumers forfeit the potential income derived from trading their PV surplus in the P2P market or injecting it into the UG. Conversely, the overheating approach allows for an increase of the setpoint temperature, enabling internal gains to contribute to the internal temperature increase and thus leading to energy savings in AC usage.

The (5) DHW Self method proves to be beneficial both economically for the RCs and from an energy perspective for the microgrid. It increases the SCR and SSR while reducing the critical consumption from the UG. This method increases the self-consumption of local PV surpluses, enhances independence from the UG, and shifts loads from periods where energy is primarily sourced from fossil fuel generation plants, to periods of high solar irradiation.

The (5) DHW Self method outperforms the (4) AC Self with only overheating in both economic and energy terms. This is because the control of a DHW tank is more flexible than that of an AC system, which is limited by thermal comfort requirements and occupancy status. Additionally, DHW tanks must comply with rigorous thermal insulation standards, enabling them to store thermal energy more effectively than residential buildings mass. As a result, they experience lower levels of thermal losses to the exterior.

The (6) DHW Self + AC Self with only overheating method presents better results for prosumers compared to (5) DHW Self, as it combines the benefits of overheating. However, the benefit for consumers decreases because prosumers increase their self-consumption, resulting in fewer surplus injections into the P2P market. Nonetheless, the community cost decreases, the SCR decreases due to the lower energy consumption of the AC systems, the SSR increases slightly, and the critical consumption decreases slightly.

Comparing the (6) DHW Self + AC Self. with only overheating method to the (2) Conventional case, it is possible to reduce P1 and P2 tariffs by 27.7% and 43.9%, respectively, C1 and C2 tariffs by 1.2% and 1.3%, respectively, community energy costs by 7.6%, increase SCR and SSR by 16.2% and 9.0%, respectively, and reduce energy import from the UG during critical periods by 16.5%.

Finally, comparing the (6) DHW Self + AC Self. with only overheating with the current case in Chile, corresponding to (1) the base case without a P2P market, it is possible to reduce P1 and P2 tariffs by 32.6% and 56.4%, respectively, C1 and C2 tariffs by 2.6% and 2.5%, respectively, community energy costs by 11.5%, increase SCR and SSR by 33.5% and 17.8%, respectively, and reduce energy import from the UG during critical periods by 17.1%.

7.4 Models Comparison with Fixed-speed AC System

Table 7.3 summarizes the results of the same previous analysis but using a fixed-speed AC. The results show similar trends to those obtained for an inverter AC. The green and red arrows in the cells indicate an improvement or worsening in the key indicators compared to Table 7.3. For conventional operation without smart management of thermal loads, worse economic and energy indicators are observed. However, when applying smart control of the fixed-speed AC through overheating and overcooling, the economic results for prosumers improve because a fixed-speed AC has a more flexible operating temperature range, allowing for better leveraging of local energy surpluses. However, the results worsen for consumers, with a slight increase in their bills and poorer performance in terms of energy indicators.

Table 7.3: Smart thermal load management scenarios comparison for fixed speed AC system .

Metric	Part.	(1) No P2P	(2) Conv.	(3) AC Self	(4) AC Self (overheating)	(5) DHW Self	(6) DHW Self + AC Self (overheating)	Unit
Annual bills	P1	321↓	301↓	313↑	246↑	256↓	197↑	USD
	P2	338↓	265↓	260↑	237↑	172↓	135↑	
	C1	1279↓	1261↓	1246↓	1241↓	1235↓	1242 =	
	C2	1107↓	1094↓	1093↓	1093↓	1069↓	1079↓	
	CM	3045↓	2920↓	2914↑	2817↑	2732↓	2652↑	
SCR	CM	56.6↓	73.6↓	74.3↓	70.9↓	91.7↓	89.7↓	%
SSR	CM	26.6↓	35.2↓	35.6↓	34.7↓	44.4↓	44.6↓	%
Energy from UG (critical periods)	CM	5400↓	5353↓	5309↑	5287↓	4451↓	4381↑	kWh/ year

CM: Community

Overall, both systems yield fairly similar results; however, it is chosen to further analyze the smart control of an inverter AC, which has gained popularity in the market in recent years.

7.5 Sensitivity Analysis

A sensitivity analysis was conducted, evaluating key indicators in 2187 scenarios by varying the sizing of the BESS, AC systems, and DHW tanks, under the escenario (6) DHW Self + AC Self (overheating). Table 7.4 summarizes the variable parameters. A pairwise correlation matrix was obtained among the variable parameters, showing linear relationships between -1 and 1.

Table 7.4: Variable parameters in sensitivity analysis.

Parameter	Value			Unit
	P1	P2	Consumers	
BESS capacity	[6,12,18]	-	-	kWh
DHW tank capacity	[100,200,300]	[100,200,300]	[100,200,300]	lt
AC system size	[S,M,L]	[S,M,L]	[S,M,L]	-

S: Small, M: Medium, L: Large

Figure 7.24 depicts the results for RCs bills. It is observed that all RCs increase their bills when they install AC systems and DHW tanks with higher capacity in their homes. This is due to AC systems showing lower efficiencies at higher size, while DHW tanks experience higher thermal losses and, at the same time, contain a greater amount of water to be heated, resulting in higher energy consumption. However, for prosumers, it would be advantageous for consumers to install DHW tanks with higher capacity, as this would make consumers more willing to buy from the P2P market. Regarding the BESS of P1, it is beneficial for P2 if P1 has a higher BESS capacity, as this reduces competition among prosumers in the P2P market, allowing P2 to sell a greater amount of surplus. However, it is not beneficial for C1, as P1 will prioritize storing their surplus rather than selling it to consumers.

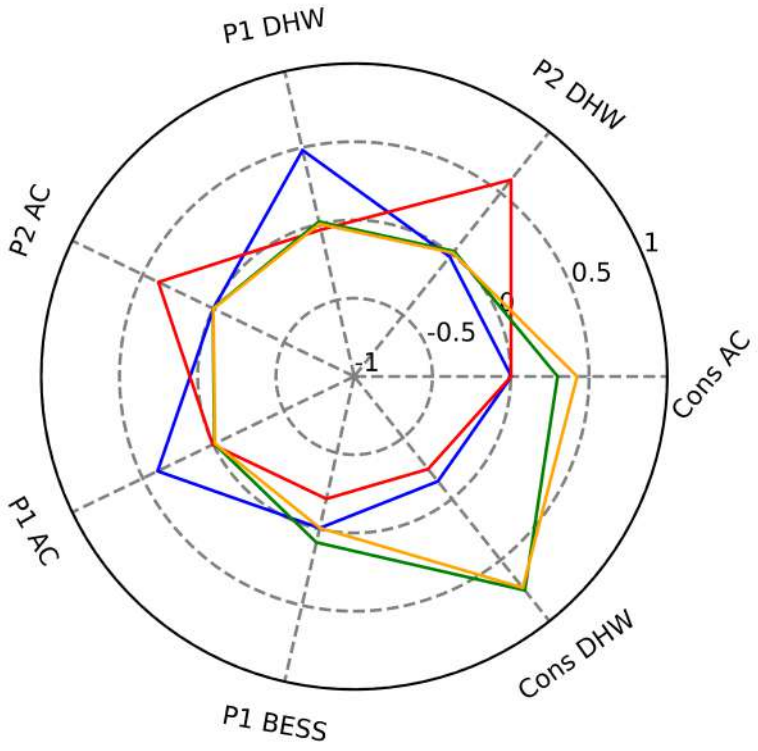

Figure 7.24: Sensitivity analysis on the bills of the RCs. The curves for P1, P2, C1, and C2 are presented in blue, red, green, and orange, respectively.

Figure 7.25 shows the results for key indicators in the microgrid. Community cost increases when RCs install higher capacity AC systems and DHW tanks, due to higher energy consumption. However,

it decreases when the BESS capacity increases, as it enhances local self-consumption. In this way, SCR increases with higher BESS and DHW tank capacities, as both are ways to store energy and avoid surplus injection into the UG. SSR decreases with larger AC systems, as more energy is imported from the UG, but increases with higher BESS and DHW tank capacities, reducing dependence on the UG.

Finally, energy from the UG during critical periods increases with larger AC systems in consumers, due to lower efficiencies. It also increases with higher DHW tank capacity in P2, as this reduces its surplus injection into the P2P market, reducing consumers' chances of buying for DHW Self. during sunny hours. Conversely, if P1 installs a larger DHW tank, critical consumption decreases, as P1 prioritizes storing surplus in the BESS, and a large part of DHW tank consumption comes from the UG, unlike P2, where the DHW tank is the only storage source. Also, if consumers install larger DHW tank capacities, critical consumption decreases, as they can store more energy from surplus in the P2P market. Lastly, increasing P1's BESS increases critical consumption, as a large part of P1's PV surplus will be stored in the BESS, affecting the availability of supply in the P2P market for consumers to buy for DHW Self and increasing the consumption of P1 during the critical period for DHW heating.

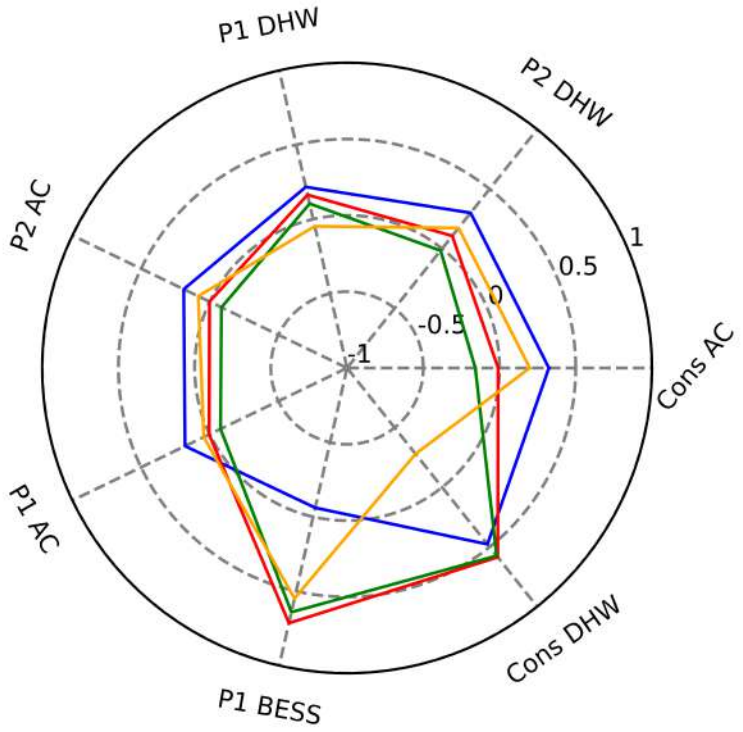

Figure 7.25: Sensitivity analysis on the community costs (blue curve), SCR (red curve), SSR (green curve), and energy from the UG during critical periods (orange curve).

7.6 Geographic Analysis

In Chile, different geographic zones of the country have been classified according to their meteorological conditions and thermal requirements through a thermal zoning, applying different building regulations,

thermal insulation requirements, and energy efficiency, according to the Chilean Official Standard NCh 853:2021. The territory is divided into 9 thermal zones, from A (less stringent) to I (most stringent) [57]. Figure 7.26 shows the distribution of the thermal zones throughout the territory. It can be observed that the less stringent zones are located in the north of the country, generally near the coasts, while the most stringent correspond to the southernmost region or in high mountain areas.

The same analysis as before is carried out, applied to characteristic cities of each thermal zone; Zone A: Arica, Zone B: Vicuña, Zone C: Viña del Mar, Zone D: Santiago, Zone E: Concepción, Zone F: Temuco, Zone G: Puerto Montt, Zone H: Calama, and Zone I: Punta Arenas. Table 7.5 summarizes the collected meteorological data, corresponding to dry bulb temperature, relative humidity, solar irradiation, and wind speed. It can be observed that northern zones present a higher average irradiation, benefiting the amount of PV generation by prosumers. On the other hand, Table 7.6 summarizes the thicknesses of the materials in the construction solution, along with their corresponding U-values obtained and the maximum values allowed by the NCh 853:2021 [57]. These were calculated for a TMY, based on local meteorological conditions. Additionally, Table 7.7 summarizes the electricity prices from different regional distribution companies, along with the estimated prices for the P2P market. For the cities of Arica, Vicuña, Viña del Mar, Concepción, Temuco, and Calama, the prices were obtained from the Compañía General de Electricidad (CGE) [45], for Santiago from Enel [74], for Puerto Montt from Grupo Saesa [75], and for Punta Arenas from the Empresa de Electricidad de Magallanes (Edelmag) [76].

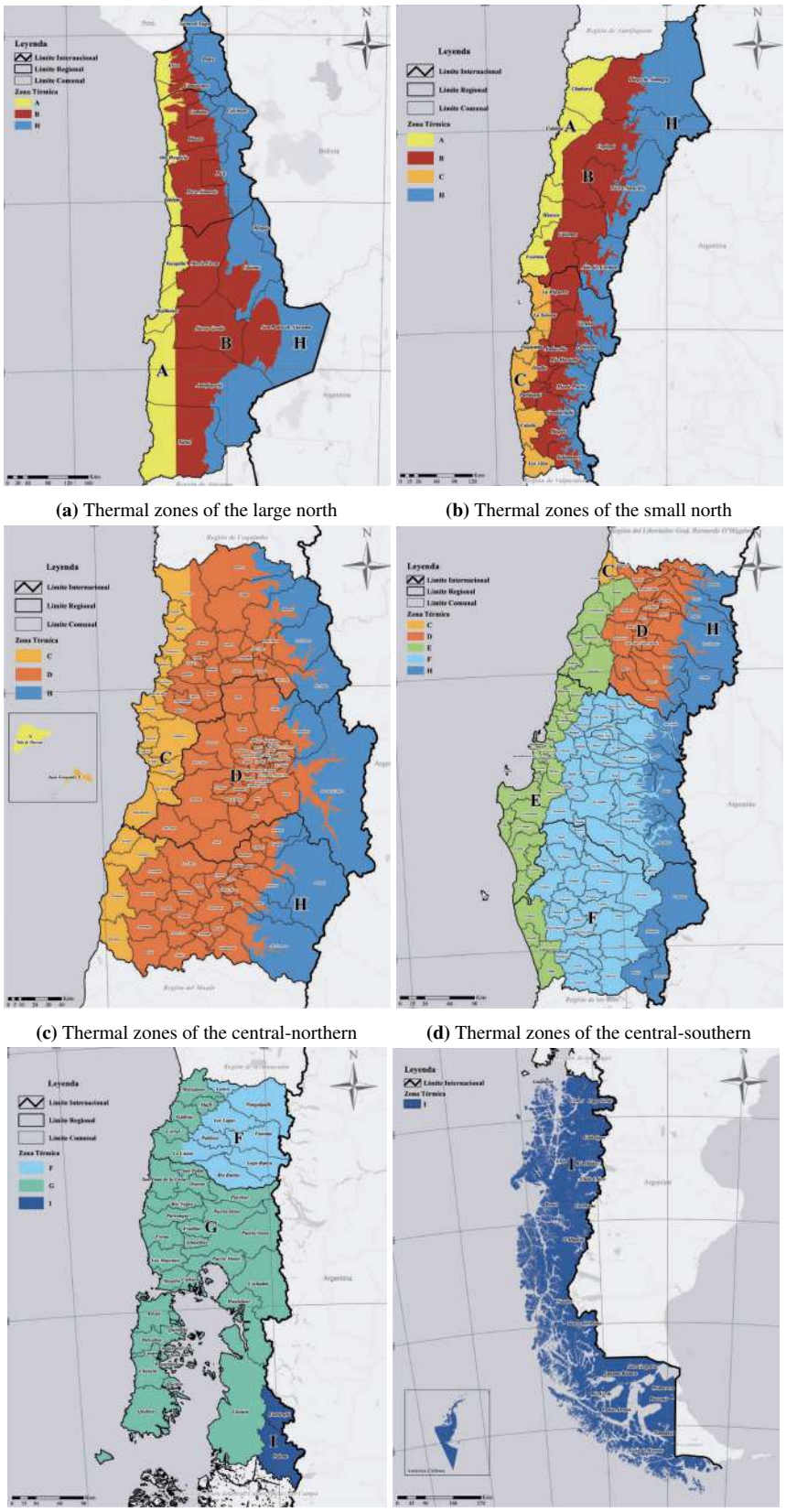

(a) Thermal zones of the large north

(b) Thermal zones of the small north

(c) Thermal zones of the central-northern

(d) Thermal zones of the central-southern

(e) Thermal zones of the south

(f) Thermal zones of the extreme south

Figure 7.26: Residential thermal zones in the territory of Chile [57].

Table 7.5: Summary of meteorological variables.

Parameter/ Thermal Zone	A	B	C	D	E	F	G	H	I
Dry bulb temperature (min/avg/max) [°C]	10.9/ 18.9/ 29.3	4.0/ 16.6/ 32.7	1.9/ 14.2/ 29.5	0.3/ 15.9/ 34.5	-3.0/ 12.6/ 29.4	-2.4/ 12.0/ 36.4	-5.1/ 10.7/ 26	-0.6/ 14.7/ 29.6	-5.2/ 6.7/ 22.0
Relative humidity (min/avg/-max) [%]	13.8/ 69.7/ 90	7.4/ 81.4/ 100	13/ 76.9/ 100	12/ 64.7/ 100	12/ 79.4/ 100	6/ 84.4/ 100	22/ 87.5/ 100	0.3/ 25.1/ 97	17/ 71.1/ 99
Solar radiation (avg/max) $[W/m^2]$	271/ 1103	274/ 1144	230/ 1140	238/ 1106	222/ 1152	191/ 1133	159/ 1123	330/ 1208	171/ 1123
Wind velocity (min/avg/max) $[m/s]$	0/ 1.6/ 5.3	0/ 2.3/ 7.8	0/ 1.6/ 8.1	0/ 1/ 3.6	0/ 1.8/ 8.2	0/ 2.4/ 11.6	0/ 2.8/ 11.9	0/ 4.9/ 11.8	0/ 3.8/ 13.3

Table 7.6: Characteristics of the construction solution and U-values considered for each thermal zone.

Parameter/ Thermal Zone	A	B	C	D	E	F	G	H	I
Wall material thickness [mm]: Reinforced concrete/Expanded polystyrene/Cement mortar	200/ 10/ 10	200/ 50/ 10	200/ 50/ 10	200/ 50/ 10	200/ 60/ 10	200/ 100/ 10	200/ 110/ 10	200/ 130/ 10	200/ 110/ 10
U-value Wall / (Max. allowed) $[W/(m^2K)]$	[1.55-1.91] / (2.10)	[0.62-0.68] / (0.80)	[0.62-0.67] / (0.80)	[0.62-0.67] / (0.80)	[0.54-0.58] / (0.60)	[0.35-0.37] / (0.45)	[0.33-0.34] / (0.40)	[0.28-0.29] / (0.30)	[0.33-0.34] / (0.35)
Roof material thickness [mm]: Reinforced concrete/Expanded polystyrene/Zinc roof tile	200/ 40/ 30	200/ 80/ 30	200/ 80/ 30	200/ 100/ 30	200/ 120/ 30	200/ 160/ 30	200/ 160/ 30	200/ 160/ 30	200/ 160/ 30
U-value Roof / (Max. allowed) $[W/(m^2K)]$	[0.73-0.82] / (0.84)	[0.43-0.46] / (0.47)	[0.43-0.46] / (0.47)	[0.35-0.37] / (0.38)	[0.30-0.32] / (0.33)	[0.23-0.24] / (0.28)	[0.23-0.24] / (0.28)	[0.23-0.24] / (0.25)	[0.23-0.24] / (0.25)
Windows material thickness [mm]: Monolithic glass/Air chamber (emissivity)	6/ 0 /6	6/ 20 (0.82) /6	6/ 20 (0.82) /6	6/ 20 (0.82) /6	6/ 20 (0.82) /6	6/ 20 (0.82) /6	6/ 10 (0.2) /6	6/ 10 (0.2) /6	6/ 10 (0.2) /6
U-value Windows / (Max. allowed) $[W/(m^2K)]$	5.56 / (5.80)	2.82 / (3.60)	2.82 / (3.60)	2.82 / (3.60)	2.82 / (3.00)	2.82 / (3.00)	2.17 / (2.40)	2.17 / (2.40)	2.17 / (2.40)

Table 7.7: Electricity prices from the utility grid and P2P market for the different thermal zones.

Parameter/ Thermal Zone	A	B	C	D	E	F	G	H	I
Utility prices									
Fixed monthly charge (USD/month)	1.18	1.36	1.36	0.70	1.07	1.07	1.14	1.07	1.36
Import price (USD/kWh)	0.18	0.18	0.17	0.16	0.17	0.18	0.16	0.17	0.16
Injection price (USD/kWh)	0.10	0.10	0.10	0.09	0.10	0.10	0.08	0.11	0.08
P2P market prices									
Buying price (USD/kWh)	0.16	0.17	0.16	0.14	0.16	0.17	0.15	0.16	0.15
Selling price (USD/kWh)	0.13	0.14	0.14	0.12	0.14	0.14	0.11	0.14	0.11
Special price (USD/kWh)	0.15	0.15	0.15	0.13	0.15	0.15	0.13	0.15	0.13

Table 7.8 summarizes the results obtained for each thermal zone from the previously analyzed models. For the thermal zones in the north and center of the country, such as A, B, C, D, E, F, and H, a similar trend is followed, where scenario (6) shows the greatest decrease in prosumers' annual bills and the total cost of the community. However, scenarios (4) and (5) present better results for C1 and C2, respectively, because in (6), the increase in self-consumption by prosumers generates a lower amount of surplus to inject into the P2P market, so consumers have fewer opportunities to purchase energy. Regarding the energy KPIs of the microgrid, scenarios (5) and (6) present similar results, significantly increasing SCR and SSR, and reducing energy from the UG during critical periods compared to the base case, respectively. Thus, in these zones, scenario (6) is decided to be the most optimal, considering that it corresponds to a more feasible case than (5), where prosumers have decision-making power over smart management of local thermal loads based on the most convenient scenario for them, while consumers are dependent on the supply in the P2P market. On the other hand, in thermal zones G and I, the lowest average levels of solar irradiation are presented, allowing low availability to smart manage thermal loads through local surpluses as well as a low availability of supply in the P2P market. In this way, scenario (6) presents a practically negligible benefit for prosumers compared to scenario (5), so it would not be worth incorporating the overheating technique. In this way, scenario (5) offers better results in the KPIs for the microgrid in this thermal zones.

Table 7.8: Results of the KPIs obtained according to thermal zone and smart thermal load management model.

Thermal zone	Metric	Part.	(1) No P2P	(2) Conv.	(3) AC Self	(4) AC Self (overheating)	(5) DHW Self	(6) DHW Self + AC Self (overheating)	Unit
A	Annual bills	P1	275	259	223	196	199	134	USD
		P2	327	251	246	236	152	117	
		C1	1442	1420	1368	1366	1376	1400	
		C2	1185	1173	1173	1171	1135	1157	
		CM	3229	3104	3010	2969	2862	2808	
	SCR	CM	63.6	79.1	77.2	76.2	94.6	92.9	%
	SSR	CM	32.6	41.1	40.9	40.7	49.6	49.9	%
	Energy from UG (critical periods)	CM	5293	5226	5247	5242	4229	4263	kWh/ year

Continued on next page

Table 7.8 – Continued from previous page

B	Annual bills	P1	159	133	161	61	81	-8	USD
		P2	164	83	98	51	-18	-76	
		C1	1322	1298	1243	1235	1262	1287	
		C2	1083	1069	1067	1064	1037	1058	
		CM	2728	2583	2568	2412	2362	2261	
	SCR	CM	59.8	76.5	75.1	71.2	92.6	90.7	%
	SSR	CM	34.2	44.4	43.7	43.0	54.1	54.9	%
	Energy from UG (critical periods)	CM	4523	4465	4441	4426	3604	3516	kWh/ year
C	Annual bills	P1	310	289	376	259	245	209	USD
		P2	326	253	322	250	162	142	
		C1	1275	1256	1232	1231	1230	1242	
		C2	1100	1088	1090	1087	1062	1073	
		CM	3012	2886	3020	2828	2700	2665	
	SCR	CM	57.1	74.4	76.9	72.7	91.9	90.6	%
	SSR	CM	27.0	35.9	36.1	35.5	44.8	44.8	%
	Energy from UG (critical periods)	CM	5354	5313	5358	5284	4431	4438	kWh/ year
D	Annual bills	P1	368	354	382	325	310	275	USD
		P2	362	300	318	290	214	185	
		C1	1245	1229	1204	1199	1202	1217	
		C2	1060	1050	1050	1049	1024	1037	
		CM	3035	2934	2955	2864	2751	2714	
	SCR	CM	64.0	79.1	79.3	76.7	95.5	94.6	%
	SSR	CM	29.1	36.5	36.4	36.0	44.6	44.9	%
	Energy from UG (critical periods)	CM	5589	5555	5661	5551	4836	4818	kWh/ year
E	Annual bills	P1	395	374	442	358	327	306	USD
		P2	408	344	394	346	254	243	
		C1	1319	1302	1279	1279	1275	1284	
		C2	1152	1141	1142	1140	1114	1125	
		CM	3274	3160	3257	3123	2970	2959	
	SCR	CM	56.4	72.6	75.9	71.4	90.6	89.3	%
	SSR	CM	24.9	32.6	33.4	32.4	41.3	41.1	%
	Energy from UG (critical periods)	CM	5730	5688	5663	5673	4943	4977	kWh/ year
F	Annual bills	P1	556	540	594	527	487	470	USD
		P2	584	525	553	523	427	412	
		C1	1407	1391	1372	1371	1358	1374	
		C2	1229	1219	1219	1218	1185	1200	
		CM	3775	3675	3738	3640	3457	3457	

Continued on next page

Table 7.8 – Continued from previous page

	SCR	CM	60.6	76.9	78.7	75.3	95.0	93.9	%
	SSR	CM	23.2	29.9	30.3	29.6	37.6	37.5	%
	Energy from UG (critical periods)	CM	5726	5690	5686	5684	5084	5093	kWh/ year
G	Annual bills	P1	593	585	625	584	533	532	USD
		P2	642	601	612	603	509	504	
		C1	1245	1234	1226	1226	1196	1215	
		C2	1100	1092	1093	1092	1056	1073	
		CM	3580	3512	3556	3504	3293	3224	
	SCR	CM	61.9	78.0	81.6	77.8	95.6	95.0	%
	SSR	CM	20.4	26.2	27.1	26.2	32.7	32.7	%
	Energy from UG (critical periods)	CM	6063	6031	5986	6036	5453	5480	kWh/ year
H	Annual bills	P1	-22	-56	-19	-117	-103	-185	USD
		P2	-14	-111	-87	-146	-218	-282	
		C1	1309	1286	1226	1223	1259	1272	
		C2	1056	1044	1038	1037	1020	1032	
		CM	2330	2164	2159	1997	1958	1837	
	SCR	CM	58.0	75.2	75.0	70.9	91.3	90.9	%
	SSR	CM	37.5	49.4	49.3	48.5	60.3	62.0	%
	Energy from UG (critical periods)	CM	4155	4081	4032	4029	2938	2786	kWh/ year
I	Annual bills	P1	738	729	N/A	730	666	670	USD
		P2	824	779	N/A	788	669	665	
		C1	1475	1462	N/A	1457	1423	1444	
		C2	1330	1321	N/A	1322	1283	1304	
		CM	4366	4292	N/A	4297	4040	4082	
	SCR	CM	59.4	75.1	N/A	76.0	95.9	94.2	%
	SSR	CM	18.2	23.4	N/A	23.7	30.5	30.2	%
	Energy from UG (critical periods)	CM	7827	7824	N/A	7841	6783	6903	kWh/ year

CM: Community

Table 7.9 summarizes the benefits obtained for the most optimal method in each thermal zone compared to the (2) Conventional case. Figures 7.27 and 7.28 show the annual electricity bill savings and the changes in the microgrid KPIs according to the thermal zone, respectively.

Table 7.9: Smart thermal load management scenarios comparison .

Metric	Part.	A	B	C	D	E	F	G	H	I	Unit
Annual bills reduction	P1	125	142	80	79	68	70	52	129	64	USD
	P2	135	159	111	115	101	113	93	171	110	
	C1	20	11	15	12	17	17	38	15	39	
	C2	16	11	15	14	15	19	36	12	38	
	CM	9.5	12.5	7.6	7.5	6.4	5.9	6.2	15.1	5.9	
SCR increase	CM	13.8	14.3	16.2	15.5	16.8	17.0	17.6	15.7	20.7	%
SSR increase	CM	8.7	10.5	9.0	8.4	8.5	7.5	6.6	12.6	7.1	
Energy from UG reduction (critical periods)	CM	18.4	21.3	16.5	13.3	12.5	10.5	9.6	31.7	13.3	

CM: Community

Figure 7.27 shows that the highest economic savings for prosumers occur in zones A, B and H, corresponding to northern regions with high solar radiation indices, allowing for a greater amount of PV surpluses. In this way, prosumers benefit more from smart management of thermal loads, allowing for more frequent overheating and DHW Self cycles. Calama in zone H presents the best results for prosumers, since it meets optimal characteristics, such as a high solar radiation index and the most stringent thermal regulation of all thermal zones. On the other hand, zones G and I show the greatest benefits for consumers, since the best method corresponds to DHW Self, without the consideration of overheating technique, so consumers experience a greater availability of supply in the P2P market. Additionally, although zone I has lower solar radiation than zone G, zone I has more stringent thermal insulation standards, allowing for greater savings in AC consumption, and therefore, a greater availability of surpluses to be allocated to DHW Self.

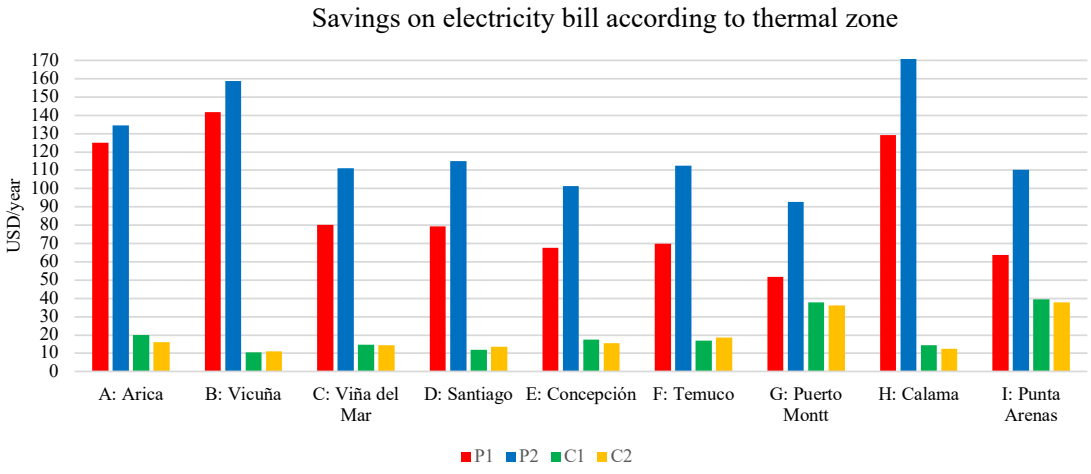

Figure 7.27: Annual electricity bill savings for RCs according to thermal zone.

Figure 7.28 shows the changes in the community's energy KPIs according to the thermal zone. Regarding the community's energy costs and energy from the UG during critical periods, it is observed once again that zones A, B, and H show the greatest reductions, and the greatest increases in SSR, thanks

to the availability of energy surpluses. Regarding the SCR, it tends to increase in thermal zones with more demanding thermal regulations, allowing for greater use of local generation.

In this way, the importance of investing in thermal insulation projects at the residential level is emphasized, which not only allows for improved energy efficiency and cost reduction, but also enhances the benefits of implementing smart management methods of thermal loads.

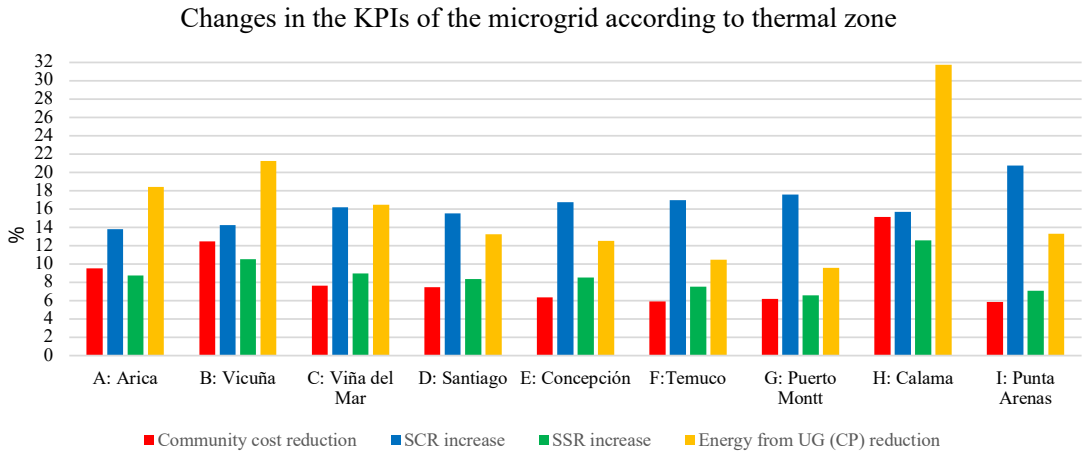

Figure 7.28: Changes in the microgrid KPIs according to thermal zone.

8 | Conclusions

This study proposes a digital twin (DT) for smart management of thermal loads in residential microgrids with peer-to-peer (P2P) transactions to evaluate key indicators such as annual bills, community costs, self-consumption ratio (SCR), self-sufficiency ratio (SSR), and the amount of energy imported from the utility grid (UG) during critical consumption periods. The evaluation results aim to incentivize local energy policies and support the resolution of current issues in the generation and transmission system.

The model considers local historical data, such as base load profiles, domestic hot water consumption profiles (DHW), typical meteorological year profiles, occupancy profiles, and building thermal insulation requirements for specific thermal zones. Physics-based and data-driven models are formulated to simulate digital twin subsystems, including the P2P market, photovoltaic (PV) systems, battery energy storage systems (BESS), and smart management of thermal loads through the control of DHW tanks and air conditioning (AC) systems, ensuring thermal comfort for occupants. The model has been evaluated for a residential microgrid consisting of two prosumers, two consumers, one aggregator, and the UG. The prosumers were involved in distributed energy resources (DERs) projects, including PV systems with or without BESS, and all the residential customers (RCs) maintain DHW tanks and AC systems. Five scenarios were compared: (1) Base case: No P2P market; AC and DHW systems operate conventionally. (2) Conventional case: P2P market with AC and DHW systems operating conventionally. (3) AC Self: P2P market with DHW operating conventionally and the AC system applying overheating and overcooling techniques. (4) Same as (2) but without considering overcooling. (5) DHW Self: P2P market with AC system operating conventionally and the DHW system flexibilizing its heating periods to prioritize self-consumption and incentivize P2P transactions. (6) Combination of scenarios (4) and (5).

The results show that flexibilizing the control of the DHW tank to prioritize the self-consumption of local PV surplus by prosumers and the purchase of surplus from the P2P market by consumers, helps reduce energy costs for the RCs, increase grid independence, boost local self-consumption, and reduce energy imported from the UG during critical consumption periods. Applying the overheating reduces AC consumption during winter by leveraging internal heat gains to achieve a higher setpoint temperature. However, the overcooling during summer increases AC consumption, as it counteracts internal heat gains.

Compared with the (2) Conventional case, case (6) was considered the most attractive for the community. It manages to reduce prosumers' annual bills by up to 43.9%. This reduction would attract investment in new distributed generation (DG) projects, resulting in a slight indirect benefit to consumers by reducing their annual bills by up to 1.3%. Additionally, at the community microgrid level, community costs would be reduced by 7.6%. SCR and SSR would increase by 16.2% and 9%, respectively. Furthermore, the

UG would benefit by reducing energy consumption during critical periods by 16.5%, achieved by shifting loads to periods of high solar irradiation. The latter directly addresses supply-demand mismatch issues in the electrical system by reducing dependence on fossil fuel-based generation plants, which increases during critical periods. Furthermore, this suggests that hypothetically including large-scale PV plants in P2P markets could directly reduce their power curtailment, addressing a long-standing issue in the local transmission system. Smart control of DHW tanks and AC systems can work synergistically to maximize benefits. However, the control of DHW tanks yields better results than the control of AC systems, mainly because DHW tanks must comply with rigorous thermal insulation standards, allowing for more efficient storage of thermal energy. Additionally, the optimal control of AC systems is limited by the thermal comfort of occupants and occupancy status. Finally, comparing case (6) with a current case in Chile, corresponding to case (1), savings in prosumers' tariffs of up to 56.4% and in consumers' tariffs of up to 2.6% would be achieved. At the microgrid level, community energy costs would be reduced by 11.5%, SCR and SSR would increase by 33.5% and 17.8%, respectively, and energy consumption from the UG during critical periods would be reduced by 17.1%.

A sensitivity analysis was conducted, varying the capacities of AC systems, DHW tanks, and BESS. Results indicate that RCs reduce their bills when they install smaller AC systems and DHW tanks, thereby reducing their energy consumption. A higher BESS capacity would negatively affect consumers due to lower availability of supply in the P2P market, while benefiting BESS-less prosumers due to reduced market competition. Also, higher BESS and DHW tank capacities for consumers would significantly improve the SCR and SSR of the microgrid, increasing independence from the UG. However, a larger BESS would drastically increase grid consumption during critical periods for consumers, as they would have fewer options for applying DHW Self, while a larger DHW tank would decrease it significantly; however, the latter is not economically viable. Therefore, it would be essential to propose a pricing scheme based on high and low consumption periods to incentivize thermal storage technologies.

A geographical analysis was conducted to extend the evaluation to different geographical zones with varying meteorological conditions, thermal insulation regulations according to the Chilean Standard NCh 853:2021, and electricity prices. For the northern, central, and central-southern regions of the country, the same trend observed in the case study in Viña del Mar is repeated, where case (6) offers the greatest benefits. However, for southern and far southern regions, the optimal case is (5), making smart thermal load management of the DHW tank only viable in these areas due to the low availability of PV surpluses. The general trend indicates that the most influential variable in the benefits is the level of solar radiation, as seen in the cities of Arica, Calama, and Vicuña, followed by the stringency of thermal insulation regulations, allowing for better performance in terms of energy efficiency of the AC system. Thus, Calama stands out as the most suitable city to establish a microgrid of this kind, as it combines the most influential variables.

9 | Appendix

9.1 DHW Tank Manufacturer Parameters

Model

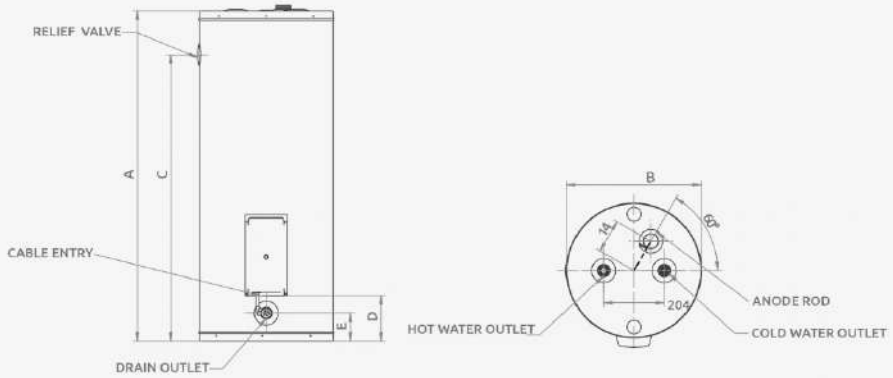

Technical Parameter

Model		100L	150L	200L	300L	400L	500L
Element sizes	standard	1.5kW	1.5kW	2kW	3kW	4kW	5kW
	optional	2/3kW	2/3kW	1.5/3/4/5kW	1.5/2/4/5/6kW	1.5/2/3/5/6kW	1.5/2/3/4/6kW
Element No.		1					
Electrical supply (Voltage /Frequency)		220V/50Hz 240V/50Hz					
Element Metrial		INCOLOY 840					
Relief Valve Pressure		1.0MPa					
Max Inlet Pressure		0.8MPa					
T&PR Valve Connection		NPT3/4					
Water Connection		NPT3/4					
Temperature Range		49-82 C					
insulation material/thickness		40mm	40mm	40mm	40mm	50mm	50mm
Tank Dimensions							
A (mm)		1114	1483	1516	1520	1576	1926
B (mm)		450	450	520	620	710	710
C (mm)		965	1340	1350	1320	1373	1722
D (mm)		154	154	163	178	210	210
E (mm)		95	95	100	100	100	100
Weight (net/gross)		38/40kg	57/60kg	69/70kg	85/88kg	113/116kg	128/132kg
		480×480×1190	480×480×1560	550×550×1595	655×655×1595	745×745×1650	745×745×2000
Outer Body Colour		white					

Figure 9.1: DHW tank datasheet.

9.2 Related Work Summary

Table 9.1: Summary of main contributions and results of related work on P2P energy trading.

Ref.	Main contributions and Results
[26]	• The proposed flexibility model aggregates demands from residential and non-residential buildings, with a local retailer controlling HVAC systems and smart appliances. Load scheduling optimization is based on day-ahead market price predictions and occupants' comfort. • Adequate demand aggregation increases local retailer profits in the day-ahead market and achieves a demand flexibility ratio between 10% and 40%. Optimal scheduling shifts part of the demand from peak to off-peak periods while maintaining indoor temperatures within the comfort range.
[37]	• A digital twin is used in the design phase to replicate a city block, showing the results of a study on city renewal using renewable resources for CO2 neutrality. Different scenarios were studied, combining subsystems like the power grid, PV systems, heat pumps, and electric heaters. The digital twin integrates real local data for diagnostics and simulations of energy demand and renewable supply, reducing risks and total investment. Economic benefits and greenhouse gas emissions are optimized based on heat pump sizing and operation for space heating and DHW, alongside PV systems. • Results show that using locally generated PV energy for both electrical consumption and thermal loads maximizes economic benefits, although the self-sufficiency ratio decreases due to increased demand from heat pumps and electric heaters.
[38]	• A model-based digital twin integrating cyber-physical systems for community energy trading is proposed, considering distributed resources such as PV systems, BESS and two P2P market paradigms, such as bill sharing and mid-market rate. Transaction simulations in a replica minigrid of a community microgrid case study quantifies the impact on grid voltage, and optimizes BESS operation and individual bills, along with allowing device testing in real-time by interfacing simulation with the real system hardware. • Results shown that energy from grid can be reduced by 15.4%, and individual bills by at least 11.3%.
[27]	• Development of a P2P energy trading model incorporating aggregated controls of residential EWH with TES, along with the implementation of a novel revenue stream for export response, which relies on real-time pricing conditions. • The proposed method can increase aggregated PV self-consumption by 42% and contribute to 17% of the total energy savings for consumers.
[28]	• Analysis of building thermal energy storage capability in P2P energy trading, and derivation of a time-varying virtual energy storage system model to quantify its demand flexibility. • The proposed method can reduce the operational costs of prosumers by 3.7% and increase self-consumption ratio by 3.1%.
[29]	• Examination of economic benefits of leveraging HPs flexibility through LEMs, including the identification of factors contributing to relatively small economic benefits and regulatory framework changes required to address them, such as high balancing costs, excessive taxes, uneven distribution of benefits and seasonal fluctuations. • The penetration of 40% of HPs in residential communities can reduce their annual energy costs by 5.1% through a LEM, leveraging demand-side flexibility to capitalize on price advantages.

Continued on next page

Table 9.1 – Continued from previous page

[33]	• A P2P model incorporating negotiation-based auction and pricing mechanisms in LEMs is considered. The model takes into account a HP responding to retail electricity prices to supply heating loads and DHW demand, flexible indoor temperature control within comfort ranges, and a TES. • The proposed model reduces average daily electricity costs for RCs by 41.24%. HP enhances flexibility in energy scheduling, and TES complements the heat supplied by the HP, allowing for responsive adjustments to variations in retail electricity prices.
[30]	• A hierarchical energy management system for a commercial neighbourhood is proposed, considering P2P energy trading, BESS sharing and demand-side control of AC loads, thermal loads and thermal storages. • The proposed model increases SSR and SCR by up to 22.8% and 11.3%, respectively. It also reduces annual operational costs by 24.6%, net equivalent CO2 emissions by 7.1%, and shifts peak demand from high-demand to high-production periods, mitigating demand-supply mismatches.
[31]	• A P2P model is proposed for an integrated electric-thermal system, accommodating both supply and demand uncertainties. An aggregator equipped with a PV system, BESS, and electric/thermal DR is included. Additionally, a solar HP for DHW demand with TES is incorporated. • The proposed model decreases total energy costs by 26.7%, increases self-consumption by 61.8%, and reduces power fluctuations and peak loads.
[32]	• A P2P market with tariffs based on participant reservation prices under the German levy regime is proposed. Representative RCs were modeled, considering HEMS, HPs, PV systems, BESS, and TES. Modifications to FiT and transaction levies for the current regime are suggested. • P2P markets are not feasible under the current regime. Under the proposed new regime, all participants benefit, with consumers being the primary beneficiaries. Additionally, storage systems are utilized more efficiently in DR.
[34]	• A P2P model considering flexibility constraint optimization, community BESS, shiftable appliances, HVAC systems and prosumer's thermal comfort through the PMV index is proposed. • Community energy costs can decrease by up to 34.6% with a 15 kWh community BESS installation, along with a 603 kW reduction in PV curtailment power for prosumers in the self-sufficiency program.
[35]	• A P2P model for RCs with HVAC systems to address power shortages is proposed. The model integrates online appliance scheduling and a pay-as-market clearing price to reduce power consumption, considering thermal preferences and adjusting set point temperatures based on electricity prices. • Depending on the flexibility of each RC, HVAC energy costs can be decreased by 10-26%, while total energy costs can be reduced by 28-36%.
[32]	• A P2P market with tariffs based on participant reservation prices under the German levy regime is proposed. Representative RCs were modeled, considering HEMS, HPs, PV systems, BESS, and TES. Modifications to FiT and transaction levies for the current regime are suggested. • P2P markets are not feasible under the current regime. Under the proposed new regime, all participants benefit, with consumers being the primary beneficiaries. Additionally, storage systems are utilized more efficiently in DR.

Continued on next page

Table 9.1 – Continued from previous page

[25]	• A review of 34 large-scale P2H DR projects is presented, considering different locations, sizes, objectives and technical implementations such as TES, EWH, AC, HVAC, TCL and HP. • P2H DR addresses infrastructure capacity limits, real-time balancing, frequency response, and load curtailment. It also facilitates load shifting, ancillary services, peak load reduction (1.5% to 48%), increased self-consumption, and complements price-based programs and TOU tariffs.

Table 9.2: Summary of technical parameters of related work on P2P energy trading.

Ref.	A)Participants, B)Building parameters, C)PV systems, D)BESS, E)Weather data, F)Electrical load data G)Thermal load data, H)Electricity prices, I)HVAC systems, J)DHW systems, K)KPIs, L) Simulation setup
[38]	• A) 6 residential prosumers and one school • C) Generation profiles: from local datasets. Daily generation: 12.1kWh • D) Capacity: 25kWh; Discharging power: 4kW • F) Load profiles: from local datasets obtained from smart meters. Daily demand: 8.9kWh • H) Retail price scheme: TOU tariffs; Buying price: 0.18 USD/kWh • K) Energy from grid, Electricity bills • L) Software: MATLAB Simulink; Horizon: 1 day
[37]	• A) 1694 residential apartments, one school and 4 kindergartens. • B) Heating floor area m^2: Apartments: 718-2880; School: 4051; Kindergarten: 777-1015 • C) Generation profiles: From Prosumer Simulation Tool. Generation: 1036 kWh/kWp per year. PV panels: Nominal power: 250W; Efficiency: 15%, Annual degradation rate: 0.5%, Installation costs: 1090 USD/kW • D) Virtual storage service provided by Lithuanian electricity distributor. Cost for stored and recovered electricity: 0.059 USD/kWh • E) Solar radiation kWh/m^2 per year: Global horizontal: 1031; Direct normal: 960; Diffuse horizontal: 536 • F) Load profiles: from local historical datasets from 2011 to 2021 • G) from AB Kauno energija company historical datasets from 2011 to 2021. Average annual space heating demand MWh: Apartment: 54-187; School: 485; Kindergarten: 82-97. Average annual DHW demand MWh: Apartment: 22-281; School: 8; Kindergarten: 4-20 • I) Rated power: 25-240kW, COP: 3.7-4.8 • K) Investment, operation and maintenance costs, Payback periods, Net present values, SSR, IRR and mitigation of CO2 emissions. • L) Software: Python, BARON solver

Continued on next page

Table 9.2 – Continued from previous page

[27]	• A) 12 residential prosumers • B) Occupancy rates: 24-50% • C) Capacity: 1.8-6.3kWp; Wiring losses: 9%; Inverter efficiency: 96%; Inverter capacity: 2-7kW • E) Origin: Australian Bureau of Meteorology; Resolution: 1min • G) Daily load data from 81 households; Avg. EWH consumption: 2078$kWh/year$; Avg. DHW load: 1543$kWh/year$; Standing losses: 535$kWh/year$ • H) Retail prices USD/kWh: Solar FiT 0.08; Peak period (6:00-10:00 and 15:00-1:00) 0.26; Off-peak period (1:00-6:00) 0.17; High-generation period (10:00-15:00) 0.14; Controlled consumption (0:00-6:00): 0.11 • J) Simulation: 20-nodes model; Volume: 210-315L; Temperature range: 60-85°C; U-value: 0.68-0.72$W/(m^2K)$; Max. heating power: 3.6kW; Load controls: DR, ER, PV consumption • K) PV self-consumption, annual savings, P2P energy traded, SCR in DHW demand • L) Software: TRNSYS, Python, PVWatts
[28]	• A) 90 residential prosumers, 4 enterprises prosumers • B) Surfaces m^2: Windows: 53-1500; Walls: 180-5300; Roofs: 50-1400. Set-point temperatures: 18-20°C • C) Peak power kWp: RCs: 3; Enterprise: 8-50 • D) Capacity kWh: RCs: 13.5; Enterprise: 60-450. Max. charging/discharging power kW: RCs: 3.5; Enterprise: 15-50 • E) Solar irradiation and ambient temperature from a TMY data • F) Power kW: RCs: 3; Enterprise: 30-128. Operation periods: 8:00-17:00 or 17:00-24:00 • H) Import price: Dynamic price model. FiT: Dependent on import price. • I) Combined HP (enterprise): Peak power: 80kW, COP: 3.4 • J) DHW storage tank: Thermal storage capacity: 800-1300kWh, Heat loss rate: 1%. • K) Prosumers/community costs, P2P energy traded, Injections to grid, SCR, Peak demand power • L) Time step: 15min
[29]	• A) 50 RCs • C) Peak power: 3-4kWp. PV penetration: 50% • D) Capacity: 3.5kWh • E) Temperature and Humidity: from OpenWeather. Solar irradiance: from Solcast • F) Annual pure demand: 3000-4000$kWh/year$ (from database) • G) Space heating demand: from SimulationX. DHW demand: 200L/day (From DHWcalc) • H) P2P market prices: from MPC algorithm, considering levies, balancing prices and retail prices • I) **HP**: Thermal power: 12kW; Room temperature range: 18-22°C. **TES tank**: Thermal model: Fully mixed; Temperature range: 30-45°C; Volume: 200L, Sizing: Should cover space heating demand for 2 hours alone. • J) TES tank: Model: Fully mixed; Temperature range: 40-65°C; Volume: 200L; Sizing: Should meet highest DHW demand for 30min. • K) Daily average costs, Peak demand power, Individual/aggregated self-consumption • L) Time step: 15min

Continued on next page

Table 9.2 – Continued from previous page

[33]	• A) 4 residential prosumers, 3 residential consumers • B) Thermal model: 1R1C. U-value: 409.09W/K. Thermal capacitance: 1.75e6 $J/(kg \cdot K)$ • C) Installed power: 6kWp. PV generation profiles: from Renewables.ninja • H) Maximum/Average/Minimum retail prices: 0.38/0.071/0 USD/kWh • I) Air-source HP: Maximum heating power: 12kW; COP: 4. Temperature range/set-point: [18.15-21.15]/21.15°C • J) TES: Capacity: 7kWh; Maximum charging/discharging power: 6kW • K) Daily average costs, Energy imported/injected to grid • L) Time step: 30min. Software: MATLAB
[35]	• A) 150 residential prosumers • B) Equivalent building thermal resistance: 5°C/kW • H) Dynamic pricing model • I) Maximum/Minimum HP power: 6/1.5kW; Air flow rate: 3.4kg/s; SHR*COP: 2; Room temperature range: 19.5-28.5°C. Temperature set-point: Increases when electricity prices are higher than its average to avoid the operation of HVAC, and decreases when are lower applying over-cooling. • K) Total energy costs, Energy imported/injected to grid • L) Software: MATLAB. Time step: 15min
[34]	• A) 50 residential prosumers • B) Thermal resistance: 2°C/kW. Thermal capacitance: 2.5kWh/C • C) Installed power: 2-8kWp. Injection maximum power capacity: 5kW • D) Capacity: 10kWh. Charging/discharging efficiency: 94% • E) Ambient temperature: from database • H) Retail prices: Buying prices: from database; Selling prices: 50% of buying prices; Thermal discomfort penalty: 50% higher than buying prices • I) **HVAC**: Maximum cooling power capacity: 3.5kW, Set-point temperature range: 18-21°C. **Thermal comfort**: Index: PMV; PMV acceptable range: ±0.5; Human metabolism rate: 80W/m^2; Clothing thermal resistance: 0.16m^2C/W; Average temperature of human skin in a comfortable state: 33.5°C • K) Energy costs, SSR • L) Software: MATLAB; Time step: 1min

Continued on next page

Table 9.2 – Continued from previous page

[30]	• A) 20 office buildings, 20 hotels, 5 malls (prosumers) • B) Typical consumption, occupancy profiles and building standards: From Hong-Kong Building Energy Code. ACH: 0.29 • C) PV and Wind generation profiles: from TRNSYS. PV: Installed power: 246-534kWp; Annual generation: 1.8e5-1.5e6kWh; Panel efficiency: 0.15; Absorptance coefficient: 0.9; Refractive index: 1.53; Cover emissivity: 0.9. Wind: Installed rated power: 0.3MW; Cut-in/Rated/Cut-off wind velocity: 3.5/10/25m/s; Hub height: 50m; Rotor diameter: 54m; Site shear exponent: 0.22 • D) Charging/discharging efficiency: 0.9; Max./Min. SoC: 0.9/0.3; Battery capacity: 500kWh • E) Recolected data: from Meteonorm. Max. solar irradiation: 1017W/m^2. Temperature range: 19-35°C; Annual average: 22.9°C. Wind velocity: Max./Avg. annual velocity: 15/5.1m/s; • F) Annual consumption $kWh/(m^2 \cdot year)$: Office: 159; Hotel: 183; Retail: 169 • H) Retail import price USD/kWh: On-peak(9:00-21:00): 0.141; Off-peak(1:00-9:00 and 21:00-24:00): 0.115. Retail export price USD/kWh: 0.026. P2P pricing mechanism: Dynamic SDR based. • I) **Constant-air-volume ventilation system with Fresh air handling unit**: Rated capacity kW: Office and Hotel: 193, Retail: 101; COP: 3; Set-point temperature: 5°C; Chiller pump rated power kW: Office and Hotel: 4.7, Retail: 2.1; TES volume m^3: Office: 15, Hotel and Retail: 10; TES thermal loss coefficient: 0.3 $W/(m^2 \cdot K)$. **Suplementary space cooling system**: Rated capacity kW: Office: 391, Hotel and Retail: 193; COP: Office: 2.85, Hotel and Retail: 3; Set-point temperature: 13°C; Chiller pump rated power kW: Office: 8.4, Hotel and Retail: 4.7; TES volume m^3: Office: 20, Hotel and Retail: 15; TES thermal loss coefficient: 0.3 $W/(m^2 \cdot K)$. **Heat recovery wheel**: Efficiency: 75% . **Deshumidification system: Central ventilation system** • J) **EWH**: Office and Hotel buildings. **Solar thermal system**: Retail buildings; Orientation: South-oriented with 20° tilted angle; Area: 60m^2; Supply temperature: 55°C. **TES**: Hotel buildings; Capacity: 5m^3; Thermal loss coefficient: 0.3$W/(m^2 \cdot K)$ • K) ECE, SSR, SCR, Energy imported/injected into grid, total community cost • L) Software: TRNSYS. Time step: 30min
[31]	• A) 2 RCs, 2 malls, 1 office building (prosumers) • C) Generation profile: From previous work Project of China Southern Grid • D) Maximum capacity: 55kWh; Charging/discharging efficiency: 0.9; Maximum charging/discharging power: 12kW • F) Demand profile: From previous work Project of China Southern Grid • H) Dynamic pricing mechanism for electric/thermal energy, based on SDR, DR benefits and supply availability. Buying price range: 0.062-0.15USD/kWh; Selling price: 0.051USD/kWh; Thermal energy buying price: 0.068USD/kWh • J) Hybrid EWH system: Considers sun-tracked solar collectors, electrical heating and TES • K) Total community cost, Electric/thermal energy balance index, Electric/thermal flatness index • L) Software: MATLAB

Continued on next page

Table 9.2 – Continued from previous page

[32]	• A) 1 prosumager, 1 prosumer, 1 consumer • C) PV generation: from database; Installed power: $10kWp$ • D) Capacity: 10 kWh; Inverter/battery efficiency: 95/98%; Inverter nominal power: $4.6kW$; Maximum charging/discharging power: $4.6kW$; Battery losses per period: 0.003% • E) Ambient temperature: from database • F) Load profiles: from database • G) Floor heating demand: from database. DHW demand: from database • H) Proposed regime: Levies modification in order to make P2P markets more feasible. Area regime: Energy transactions in a local area network, before grid connection point, avoiding grid-use levies. Current retail regime prices levies / Proposed regime /Area regime USD cents/kWh: FiT: 10.7/10.7/10.7; Levies (purchase): 20.8/12/0; VAT: 7.9/5.7/ 6.5; Operator's margin: 2.1/1.5/1.7; Potential P2P price: 41.5/29.9/18.9; Grid fees: 8.4/6.2/0; Electricity tax: 2.2/0/0; EEG surcharge (To promote expansion of renewables tax): 7.3/2.9/0; Concesion fee (use of municipal grid): 1.8/1.8/0; CHP surcharge (levy applied to power plants operators, in order to promote CHP use): 0.3/0.3/0; Offshore surcharge (to compensate off-shore wind farm operators for transmission challenges): 0.5/0.5/0; AbLaV surcharge (to compensate providers which offer flexible services to maintain grid stability): 0.01/0.01/0; §19 StromNEV surcharge (to compensate local network operators from lost revenue due to lower tariffs of certain end consumers): 0.4/0.4/0 • I) **Floor heating system**: Capacity: $10m^3$; Material: Concrete; Supply temperature: 30°C; Comfort range: 20-22°C; Temperature loss per time period (equivalent power): $\pm 0.045kW$; COP: from manufacturer data. **HP**: Maximum power: $3kW$ • J) Supply temperature: 45°C; Volume operating range: 20–180L; Volume loss per time period (equivalent power): $0.035kW$; COP: from manufacturer data • K) Overall costs, Market splits (origin of each energy consumption), Energy consumption, SSR, SCR • L) Software: Julia JuMP, Python. Time step: 1h. Horizon: 1 year

Continued on next page

Table 9.2 – Continued from previous page

[26]	• A) 4000 RCs, 12 hotels, 8 office buildings, 2 malls • B) **Hotels**: Storey buildings: 5, 15x35x20m^3; Thermal insulation: Modest; Indoor temperature range (Opening/Closing(winter)/Closing(summer)): 20-24/18-22/22-26°C. **Office**: Storey buildings: 7, 21x43x15m^3; Thermal insulation: Medium; Indoor temperature range (Opening): 20-24°C. **Malls**: Thermal insulation: High; Indoor temperature range (Opening/Closing(winter)/Closing(summer)): 18-22/15-19/21-25°C. • F) Residential profiles: from statistical data. Non-residential profiles: from physical model to estimate building's temperature dynamics and thermal capacity, considering a behavioral patterns model which considers architectural characteristics, building usage, location, on-site facilities, occupancy and economic data • H) Real-time market prices: from Iberian day-ahead market data, controlled by electricity market operator (OMI-Polo Español S.A); Average winter/summer price: 0.06/0.05 USD/kWh • I) Non-residential buildings: HPs, additional electrical space heating systems, chillers. Thermal comfort control: Based on indoor temperature • J) Non-residential buildings: HPs, Solar-collector water heating systems • K) Demand flexibility ratio, Local retailer average daily profit • L) Software: MATLAB. Time step: 15min. Horizon: 16 days during summer and winter periods, respectively.

9.3 GitHub Repository

The code created for the simulations can be accessed through https://github.com/javiersalles/P2P-markets-simulation. If access is required, please contact javier.salles@sansano.usm.cl.

Bibliography

[1] Gobierno de Chile Ministerio de Energía. Agenda de energía 2022-2026.

[2] D. Olivares M. Negrete R. Moreno N. Lobos, C. Villalobos and A. Navarro. Evaluación de la industria de generación distribuida como motor de empleo y desarrollo económico eficiente y sustentable en chile post covid-19. *Instituto de Sistemas Complejos de Ingeniería*, 1:5–102, 2021.

[3] Coordinador Eléctrico Nacional. Coordinador eléctrico nacional publica propuesta de expansión del sistema de transmisión del año 2023 por usd 279 millones.

[4] Asociación Chilena de Energía Solar AG. (ACESOL). Reporte capacidad instalada y generación 2023.

[5] Electromineria. Vertimientos de energías renovables variables pasan de 1.471 a 2.615 gwh entre 2022 y 2023.

[6] Climate Tracker. Vertimiento de energía: el nudo que chile necesita desatar.

[7] Fraunhofer Chile. Vertimiento de energía de centrales eólicas y solares fotovoltaicas del sistema eléctrico nacional (sen) en chile durante 2022.

[8] Generadoras de Chile. El desafiante nuevo contexto para una transición energética justa, sostenible y segura.

[9] D. Olivares. Análisis del potencial de los recursos energéticos distribuidos en chile. *Proceedings of Conversatorio Generadoras de Chile AG*, pages 23–26, 2022.

[10] G. Campusano. Impacto de la generación distribuida en la operación de la distribución. *Degree thesis, Dept. Electric. Eng., Chile Univ*, 2013.

[11] C. Zhang L. Thomas M. Cheng C. Long, J. Wu and N. Jenkins. Peer-to-peer energy trading in a community microgrid. *2017 IEEE Power & Energy Society General Meeting*, pages 1–5, 2017.

[12] S. Kim G. Yoon M.-I. Choi S. Park S. Park, K. Cho and S. Park. Distributed energy iot-based real-time virtual energy prosumer business model for distributed power resource. *Sensors*, 21:4533, 2021.

[13] M. Jamil M.J.A. Baig, M.T. Iqbal and J. Khan. A low-cost, open-source peer-to-peer energy trading system for a remote community using the internet-of-things, blockchain, and hypertext transfer protocol. *Energies*, 15:4862, 2022.

[14] T. Senoo Y. Takeda, Y. Nakai and K. Tanaka. Designing a user-centric p2p energy trading platform: A case study—higashi-fuji demonstration. *Energies*, 14:7289, 2021.

[15] X. Chen E.G. Lim L. Jiang B. Zhang, Y. Du and K. Yan. Potential benefits for residential building with photovoltaic battery system participation in peer-to-peer energy trading. *Energies*, 15:3913, 2022.

[16] H. Oki Y. Takeda D. Sagawa Y. Matsuda, Y. Yamazaki and K. Tanaka. Demonstration of blockchain based peer to peer energy trading system with real-life used phev and hems charge control. *Energies*, 14:7484, 2021.

[17] M.H. Chung. Comparison of economic feasibility for efficient peer-to-peer electricity trading of pv-equipped residential house in korea. *Energies*, 13:3568, 2020.

[18] J. Lin Y. Wang H. Huang, S. Nie and J. Dong. Optimization of peer-to-peer power trading in a microgrid with distributed pv and battery energy storage systems. *Sustainability*, 12:923, 2020.

[19] J. Weibezahn A. Lüth and J.M. Zepter. On distributional effects in local electricity market designs—evidence from a german case study. *Energies*, 13:1993, 2020.

[20] Y. Sidqi B. Bowler F. Zimmermann G. Deconinck A. Papaemmanouil R. Trivedi, S. Patra and S. Khadem. Community-based microgrids: Literature review and pathways to decarbonise the local electricity network. *Energies*, 15:918, 2022.

[21] W. Hou Q. Luo, Y. Zhou and L.Peng. A hierarchical blockchain architecture based v2g market trading system. *Applied Energy*, 307:118167, 2022.

[22] M. Gomes F. Bandeiras, Á. Gomes and P. Coelho. Exploring energy trading markets in smart grid and microgrid systems and their implications for sustainability in smart cities. *Energies*, 16-2:801, 2023.

[23] J. Soares T. Pinto R. Faia, F. Lezama and Z. Vale. Local electricity markets: A review on benefits, barriers, current trends and future perspectives. *Renew. Sustain. Energy Rev.*, 190:114006, 2024.

[24] H. K. Lopez and A. Zilouchian. Peer-to-peer energy trading for photo-voltaic prosumers. *Energy*, 263:125563, 2023.

[25] A. Abazi V.Z. Gjorgievski, N. Markovska and N. Duić. The potential of power-to-heat demand response to improve the flexibility of the energy system: An empirical review. *Renewable and Sustainable Energy Reviews*, 138:110489, 2021.

[26] B.P. Hayes J. Usaola X. Ayón, J.K. Gruber and M. Prodanović. An optimal day-ahead load scheduling approach based on the flexibility of aggregate demands. *Applied Energy*, 198:1–11, 2017.

[27] K.N. Hasan D.H. Clift and G. Rosengarten. Peer-to-peer energy trading for demand response of residential smart electric storage water heaters. *Applied Energy*, 353 B:122182, 2024.

[28] Z. Wang X. Jin Y. Deng Y. Mu X. Wang, H. Jia and X. Yu. A real time peer-to-peer energy trading for prosumers utilizing time-varying building virtual energy storage. *International Journal of Electrical Power and Energy Systems*, 155 B:109547, 2024.

[29] M. Doepfert P. Tzscheutschler Z. You, S.D. Lumpp and C. Goebel. Leveraging flexibility of residential heat pumps through local energy markets. *Applied Energy*, 355:122269, 2024.

[30] G. Huang S. Zheng, X. Jin and A.CK. Lai. Coordination of commercial prosumers with distributed demand-side flexibility in energy sharing and management system. *Energy*, 248:123634, 2022.

[31] J. Hao C. Sun T. Huang, Y. Sun and C. Liu. A distributed peer-to-peer energy trading model in integrated electric–thermal system. *IET Renewable Power Generation*, pages 1–16, 2023.

[32] L. Langer. An optimal peer-to-peer market considering modulating heat pumps and photovoltaic systems under the german levy regime. *Energies*, 13:5348, 2020.

[33] M. Qadrdan J. Wu W. Hua, Y. Zhou and N. Jenkins. Blockchain enabled decentralized local electricity markets with flexibility from heating sources. *IEEE Transactions on Smart Grid*, 14-2:1607–1620, 2023.

[34] A. Abdollahi H. Ghasemnejad, M. Rashidinejad and S. Dorahaki. Energy management in citizen energy communities: A flexibility-constrained robust optimization approach considering prosumers comfort. *Applied Energy*, 356:122456, 2024.

[35] F. Aminifar F. Nematkhah, S. Bahrami and J. P. S. Catalão. Exploiting the potentials of hvac systems in transactive energy markets. *IEEE Transactions on Smart Grid*, 14-5:4039–4048, 2021.

[36] D. Gusain P. Palensky, M. Cvetkovic and A. Joseph. Digital twins and their use in future power systems. *Digital Twin*, 1:4, 2022.

[37] R. Gatautis O. Vonžudaitė R. Bakas D. Milčius R. Venčaitis V. Bocullo, L. Martišauskas and D. Pupeikis. A digital twin approach to city block renovation using res technologies. *Sustainability*, 15:12:9307, 2023.

[38] F. Olatunji Y. Tsado, O. Jogunola and B. Adebisi. A digital twin integrated cyber-physical systems for community energy trading. *2022 IEEE International Conference on Communications, Control, and Computing Technologies for Smart Grids*, pages 134–140, 2022.

[39] H. Sun I. Castro M. You, Q. Wang and J. Jiang. Digital twins based day-ahead integrated energy system scheduling under load and renewable energy uncertainties. *Applied Energy*, 305:117899, 2022.

[40] P. Georgali E. Klumbyte A. Jurelionis P. Spudys, N. Afxentiou and P. Fokaides. Classifying the operational energy performance of buildings with the use of digital twins. *Energy and Buildings*, 290:113106, 2023.

[41] A. Flores-Maradiaga J. Salles-Mardones and M. Abdelhamid. Feasibility assessment of photovoltaic systems to save energy consumption in residential houses with electric vehicles in chile. *Sustainability*, 14(9):5377, 2022.

[42] Gobierno de Chile Ministerio de Energía. Explorador solar.

[43] M. Bagheri-Sanjareh M. Hassan and S. Hossien. A new method for energy management of residential microgrid for sizing electrical and thermal storage systems. *Sustainable Cities and Society*, 76:103482, 2022.

[44] V. Dorer A. Prasanna and N. Vetterli. Optimisation of a district energy system with a low temperature network. *Energy*, 137:632–648, 2017.

[45] Compañía General de Electricidad (CGE). Tarifas de suministro cge – febrero 2024.

[46] John A. Duffie and William A. Beckman. *Solar Engineering of Thermal Processes*, volume Fourt Edition. 2013.

[47] Rakesh Sinha, Birgitte Bak Jensen, Jayakrishnan Radhakrishna Pillai, Carsten Bojesen, and Bertil Moller-Jensen. Modelling of hot water storage tank for electric grid integration and demand response control. In *2017 52nd International Universities Power Engineering Conference (UPEC)*, pages 1–6, 2017.

[48] Yunus A. Cengel. *Transferencia de Calor y Masa: Un Enfoque practico*, page 311–316. McGraw-Hill, 2007.

[49] GMO. Full line electric water heater.

[50] Si Paing, Timothy Anderson, and Roy Nates. Natural convection heat transfer inside vertical cylindrical solar storage tanks. pages 1–8, 01 2021.

[51] Theodore L. Bergman, Adrienne S. Lavine, Frank P. Incopera, and David P. Dewitt. *Fundamentals of heat and mass transfer*, page 537–539. John Wiley and Sons, seventh edition, 2011.

[52] Boles M. A. Cengel, Y. A. *Thermodynamics*, page 743–745. McGraw-Hill, 2011.

[53] R Stull. Wet-bulb temperature from relative humidity and air temperature. *Journal of Applied Meteorology and Climatology*, 50(11):2267–2269, 2011.

[54] Inc The MathWorks. House heating system.

[55] Hector Bastida, Carlos E. Ugalde-Loo, Muditha Abeysekera, Meysam Qadrdan, and Jianzhong Wu. Thermal dynamic modelling and temperature controller design for a house. *Energy Procedia*, 158:2800–2805, 2019. Innovative Solutions for Energy Transitions.

[56] Gobierno de Chile Servicio de Vivienda y Urbanización SERVIU. Cálculo de transmitancia.

[57] Gobierno de Chile Ministerio de Vivienda y Urbanismo MINVU. *Estándares de Construcción Sustentable para Viviendas, Tomo II: Energía*. Gobierno de Chile, segunda edición edition, 2018.

[58] INN. *Norma Chilena NCh853: 2021 -Building components and building elements - Thermal resistance and thermal transmittance - Calculation methods*. Instituto Nacional de Normalización, quinta edición edition, 2021.

[59] Waldo Bustamante. *Propuesta de actualización de la reglamentación térmica, Art. 4.1.10 de la Ordenanza General De Urbanismo y Construcciones (OGUC)*. Ministerio de Vivienda y Urbanismo, 2016.

[60] INN. *Norma Chilena NCh853: 2007 -Building components and building elements - Thermal resistance and thermal transmittance - Calculation methods*. Instituto Nacional de Normalización, primera edición edition, 2007.

[61] Kaiser Ahmed, Jarek Kurnitski, and Bjarne Olesen. Data for occupancy internal heat gain calculation in main building categories. *Data in Brief*, 15:1030–1034, 2017.

[62] M. Gálvez, J. García, R. Barraza, and J. Contreras. Parametric analysis of an air-based radiative cooling system coupled to a thermal storage wall for a low-income household. *Energy and Buildings*, 252:111364, 2021.

[63] Samsung. *Single Technical Data Book*. Number p. 19-26. Samsung, 2015.

[64] Diana Enescu. A review of thermal comfort models and indicators for indoor environments. *Renewable and Sustainable Energy Reviews*, 79:1353–1379, 2017.

[65] M. S. Owen. *2021 ASHRAE Handbook*. Number p. 17.1-17.16. ASHRAE, 2021.

[66] P.O. Fanger. *Thermal Comfort: Analysis and Applications in Environmental Engineering*. R.E. Krieger Publishing Company, 1982.

[67] F. Tartarini and S. Schiavon. pythermalcomfort: A python package for thermal comfort research. *SoftwareX*, 12:100578, 2020.

[68] Dirección General de Aeronáutica Civil Dirección Meteorológica de Chile. Servicios climáticos.

[69] Gaetani I. Hoes PJ. et al. Muroni, A. Occupant behavior in identical residential buildings: A case study for occupancy profiles extraction and application to building performance simulation. *Building Simulation*, 12:1047–1061, 2019.

[70] National Renewable Energy Laboratory. Commercial and residential hourly load profiles for all tmy3 locations in the united states.

[71] Coordinador Eléctrico Nacional. Demanda sistemática real.

[72] Luis M. López-Ochoa, Konstantin Verichev, Jesús Las-Heras-Casas, and Manuel Carpio. Solar domestic hot water regulation in the latin american residential sector with the implementation of the energy performance of buildings directive: The case of chile. *Energy*, 188:115985, 2019.

[73] A. Pérez-Fargallo, D. Bienvenido-Huertas, S. Contreras-Espinoza, and L. Marín-Restrepo. Domestic hot water consumption prediction models suited for dwellings in central-southern parts of chile. *Journal of Building Engineering*, 49:104024, 2022.

[74] Enel. Tarifas suministros 16t clientes regulados - marzo 24 t1.

[75] Grupo Saesa. Tarifas de suministro eléctrico - abril de 2024.

[76] Edelmag. Publicación de tarifas de suministro empresa eléctrica de magallanes s.a.